Master's Thesis

Measurement of the London penetration depth of superconductors using a spiral coil for next-generation accelerator development
(次世代加速器開発のための螺旋コイルを用いた超伝導体のロンドン侵入長の測定)

Li He

Department of Physics

Graduate School of Science

Tohoku University

2025

Abstract

The International Linear Collider (ILC) is a proposed high-precision electron-positron collider designed to explore fundamental questions in particle physics, particularly through detailed studies of the Higgs boson and top quark. A central component of the ILC is the use of Superconducting Radio Frequency (SRF) cavities, which offer high accelerating gradients and reduced power loss at cryogenic temperatures. Understanding the electromagnetic properties of superconducting materials used in SRF cavities, such as niobium (Nb) and niobium-tin (Nb_3Sn), is essential for optimizing cavity performance. Among these properties, the London penetration depth, which characterizes the exponential decay of magnetic fields within a superconductor, is of great importance.

This thesis presents a practical method to measure the London penetration depth based on an inductive technique using a planar spiral coil. In this approach, a spiral coil is integrated into a resonant circuit and positioned near the surface of a superconducting sample. As the temperature of the sample changes, so does its penetration depth, leading to a measurable shift in the resonant frequency of the circuit. By tracking this frequency shift with a network analyzer and applying a parametrized inversion formula based on the analytical solutions of Maxwell's equations, the temperature dependence of the London penetration depth can be extracted.

A two-dimensional Green's function is derived for calculating the magnetic vector potential of an axis-symmetric coil placed below a conventional bulk superconductor of finite thickness. The equivalence between the solutions of the magnetic vector potential obtained via the Green's function and the Hankel transform was verified. For axis-asymmetric coils, such as spiral coils, a parameterized inductance model effective within a certain range of penetration depths in the low-temperature region has been proposed. All theoretical models derived in this thesis have been compared with the simulation results.

Experimental measurements of the London penetration depth were carried out at cryogenic temperatures using two fabricated planar spiral coils and two different niobium(Nb) superconducting samples. The temperature dependence of the London penetration depth for each sample was extracted from the measured resonant frequency shift. The result of critical temperature and the London penetration depth of two Nb samples at 0 K were presented in this thesis.

Contents

List of Figures

List of Tables

Chapter 1

Introduction

1.1 Superconducting Cavities

The phenomenon of superconductivity was first observed in 1911 by Heike Kamerlingh Onnes in Leiden, shortly after his successful liquefaction of helium which enabled access to temperature near absolute zero. In his experiment, he discovered that the electrical resistance of solid mercury dropped abruptly to zero at at 4 K, which marked the beginning of superconductivity research.

Despite the phenomena of perfect electrical conductivity, Superconductivity is distinguished by another remarkable phenomena: *perfect diamagnetism*. Perfect diamagnetism of conventional superconducting material was discovered in 1933 by Meissner and Ochsenfeld known as the *Meissner effect*, it refers to the complete expulsion of magnetic flux from the interior of a superconductor (see Figure 1.1) when it transforms into superconducting state. The magnetic field is excluded from the interior of the material and decays rapidly within a shallow surface layer, and the thickness of this layer is characterized by the *London Penetration Depth*. The London penetration depth $\lambda(T)$ characterizes the exponential decay of the magnetic field within a superconductor and reflects the electromagnetic response of the superconducting material.

The underlying mechanism of superconducting material remained a mystery for several decades. It was not until the mid-20th century that significant theoretical progress was made. During the 1950s and 1960s, a non-relativistic quantum field theory called Bardeen-Cooper-Schrieffer (BCS) theory was established, which offers a microscopic explanation for superconducting phenomenology. Specifically, BCS theory provides a microscopic explanation for Messier Effect by describing the formation of bound electron pairs, known as Cooper pairs. From BCS theory, one can derive the temperature dependence of the superfluid density, which gives the temperature dependence prediction of London penetration depth.

The development of next-generation accelerators, such as the International Linear Collider (ILC), requires advanced acceleration technologies. As part of the ILC's development, beam acceleration tests have been successfully conducted at around 2 K under pulsed high-gradient electric fields, which achieves the ILC's target average accelerating gradient of 32 MV/m, with beam energies reaching up to 280 MeV.

A critical component of ILC in achieving higher accelerating gradients and reduced energy losses is the implementation of Superconducting Radio-Frequency (SRF) cavities

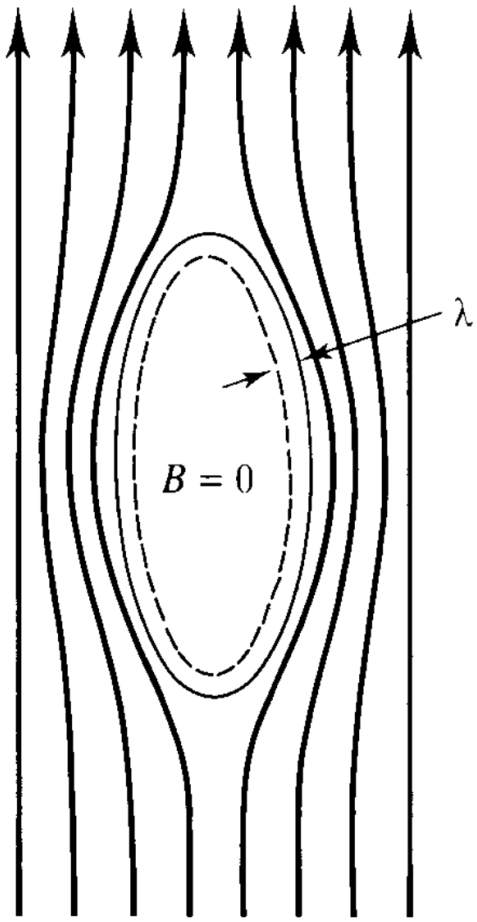

Figure 1.1: Schematic illustration of the Meissner effect [1]. The magnetic field is expelled from the interior of the superconductor, resulting in $B = 0$ inside. The penetration depth λ characterizes the exponential decay of the magnetic field near the surface.

(Figure 1.2). Among the various materials used for SRF technology, niobium (Nb) has long been the standard material due to its high critical temperature and favorable mechanical properties. Bulk Nb cavities can operate efficiently at low temperatures and have demonstrated reliable performance in many operational accelerators. For bulk Nb superconductor, the quality factor Q value or surface resistance depends on the mean free path (mfp). Moreover, there exists an optimal value of the mfp. The mfp reaches its optimum when it has a moderate length (approximately equal to the coherence length) [6] [7]. Since the London penetration depth is a function of mfp, by measuring the London penetration depth, we can determine the mfp. This is one of the motivations for measuring the London penetration depth of bulk Nb.

Figure 1.2: Photograph of a 1.3 GHz superconducting niobium nine-cell cavity used in particle accelerators [3].

In the recent development of advanced SRF accelerators, the bulk Nb cavity has reached its performance limit. Therefore, experts in SRF technology have proposed applying inner-surface coatings to surpass the capabilities of pure bulk Nb cavities [4]. With such coatings, the critical field of the sample can be significantly increased. Figure 1.3 shows a comparison of the effective critical field H_{c1} between a pure bulk Nb sample and multilayer $NbN/SiO_2/Nb$ samples with different NbN layer thicknesses.

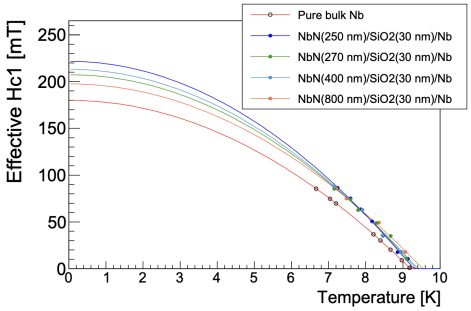

Figure 1.3: Comparison of effective critical field H_{c1} between pure bulk Nb sample and $NbN/SiO_2(30nm)/Nb$ multilayer samples [13].

The accelerating gradient of SRF cavities refers to the rate of the energy of the electron and positron beams increased per unit length. It is typically measured in megavolts per meter (MV/m). For the ILC design, the SRF niobium cavities are targeted to achieve an accelerating gradient of around 31.5 MV/m [13]. The accelerating gradient is one of the

most important parameters to evaluate the performance of accelerator, as a higher accelerating gradient allows achieving the desired collision energy with a shorter accelerator length. Theoretically, the relation between the accelerating gradient and the critical field is given by the following equation [9]:

$$\mu_0 H_0 = g E_{\text{acc}} \tag{1.1}$$

where g is a constants depends on the shape of cavities, and critical field H_{c1} serves as the upper limit of H_0. From the above relation, we can determine the maximum achievable accelerating gradient once we knew the value of the critical field H_{c1}.

In recent years, attention has also shifted toward niobium-tin (Nb_3Sn) coating [2]. Nb_3Sn is a conventional superconducting material that offers a higher critical temperature and critical magnetic field compared to pure niobium. For Nb_3Sn/Nb bilayer samples(figure 1.4), the expected critical field H_c is around 60 MV/m. The theoretical expression of critical field of such bilayer structure is given by the following equations [9]:

$$H_{sh}(d) = \min\left[c_1(d)H_{sh}^{(S)},\ c_2(d)H_{sh}^{(\Sigma)}\right], \tag{1.2}$$

$$c_1(d) = \frac{\cosh\left[d/\lambda_0^{(S)}\right] + \left[\lambda_0^{(\Sigma)}/\lambda_0^{(S)}\right]\sinh\left[d/\lambda_0^{(S)}\right]}{\sinh\left[d/\lambda_0^{(S)}\right] + \left[\lambda_0^{(\Sigma)}/\lambda_0^{(S)}\right]\cosh\left[d/\lambda_0^{(S)}\right]}, \tag{1.3}$$

$$c_2(d) = \cosh\left[d/\lambda_0^{(S)}\right] + \left[\lambda_0^{(\Sigma)}/\lambda_0^{(S)}\right]\sinh\left[d/\lambda_0^{(S)}\right]. \tag{1.4}$$

where the H_{sh} is the superheating field($H_{sh} \approx H_c$), $\lambda_0^{(S)}$ and $\lambda_0^{(\Sigma)}$ are the London penetration depths of the superconductor and superconductor substrate in Figure 1.4, respectively. From this equation, we can plot the maximum value of the magnetic field H_{0max} (H_{sh}) as the function of the coating thickness d (as shown in Figure 1.5).

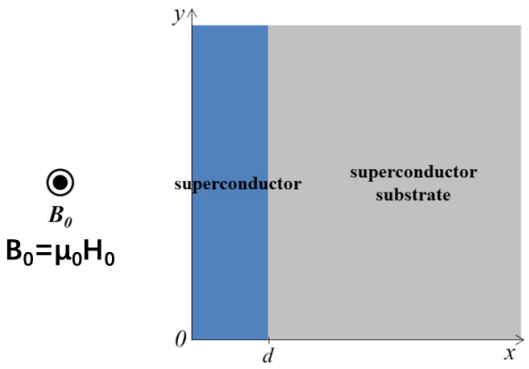

Figure 1.4: A bilayer superconductor without an insulator layer [8]. We denote the London penetration depths of the superconductor and superconductor substrate as $\lambda_0^{(S)} = \lambda_1$ and $\lambda_0^{(\Sigma)} = \lambda_2$.

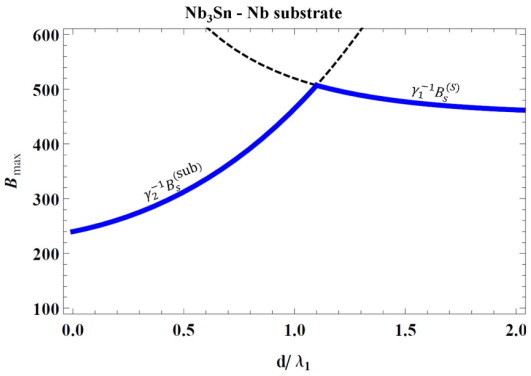

Figure 1.5: Theoretical value of the magnetic field limit of an Nb_3Sn/Nb bilayer structure as a function of coating thickness d, where it assumed $\lambda 1 = 120nm(Nb_3Sn)$ and $\lambda 2 = 40nm$(Nb) [8].

From Figure 1.5 we found that in a multilayer cavity, there exists an optimal coating thickness d for the superconducting thin film at the surface [10] [11] [12]. In recent years, experiments have been conducted to investigate the existence of an optimal coating

thickness of such multilayer superconductors [13] [14]. This optimal thickness d depends on the London penetration depth of the superconducting thin film used in the multilayer structure. Once we knew the London penetration depth of these materials, we can plot the maximum value of H_0 as a function of coating thickness d as shown in figure 1.5. Therefore, to fabricate a multilayer cavity with the optimal coating thickness, it is necessary to know the London penetration depth.

1.2 Inductance Technique

The inductance technique provides a method for measuring the London penetration depth of superconductors with high resolution. In this study, we use a planar spiral coil proposed by Dr. Iwashita and currently being tested in collaboration with Dr. Fuwa (see Figure 1.7) since 2021. This type of coil is made of copper foil on a conventional PCB substrate and is easier to manufacture than coils used in previous studies.

The coil is part of a resonant circuit, which is connected to a single port of Network Analyzer (Figure.1.6). As the temperature of the superconducting sample changes, the London penetration depth also varies, leading to a variation in the inductance of the spiral coil. This change is observed as a shift in the resonant frequency of the circuit, which can be detected by a network analyzer. By precisely monitoring these frequency shifts and applying an inversion formula based on the solution of Maxwell's equations, the value of the London penetration depth at different temperatures can be extracted. The basic derivation steps of the inversion formula can be understood in the following way:

1. Assuming that the current flows at the surface of the superconductor obeys London equations. Solving Maxwell's equations together with London equations to obtain the value of magnetic vector potential $A(\lambda)$ as a function of penetration depth λ along the coil.

2. Calculate the line integral of magnetic vector potential along the coil to obtain the inductance of the coil $L(\lambda)$ as a function of penetration depth λ.

3. Using the formula of resonant frequency $f(L)$ to obtain the relation between resonant frequency and coil inductance at resonance. Since $L(\lambda)$ is a function of London penetration depth, $f(\lambda)$ will be a function of London penetration depth as well. Therefore we can know the value of London penetration depth by reading resonant frequency from Network Analyzer.

The inductance technique is highly sensitive to small variations of London penetration depth and is suitable for both bulk and thin-film superconducting samples. The simple fabrication process of the spiral coil, combined with its appreciable sensitivity, makes it a practical approach for measuring the London penetration depth of superconductors.

1.3 The content of this Thesis

The objective of this thesis is to measure the London penetration depth of the superconducting sample. The method used in this thesis can be applied to measure any

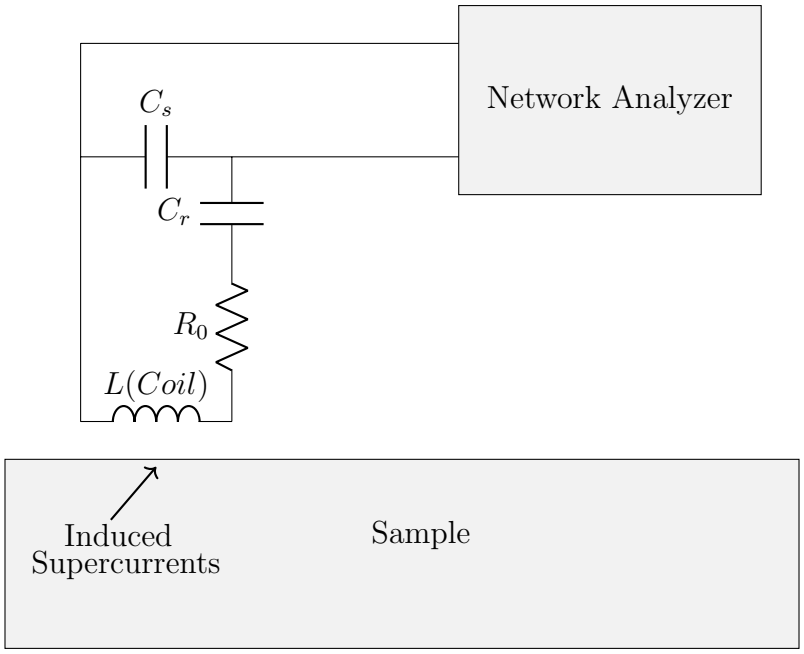

Figure 1.6: Schematic illustration of the measurement setup. A more detailed explanation is described in the experimental section.

superconducting sample of finite thickness. Its application is not only limited to SRF cavities, but also suitable for any research requiring knowledge of the London penetration depth of superconducting materials.

One of the innovative points introduced in this paper is that the pancake coils with a diameter of approximately 0.75 mm used in previous studies were too small to be fabricated, so they were replaced with flat spiral coils with a diameter of approximately 2 mm (Figure. 1.7).

The objective of this research is to obtain the London penetration depth at 0 K of the superconducting materials used in SRF cavities. This will provide reference values of the London penetration depths for optimizing the performance of the multilayer SRF cavities.

The content of this research is summarized in three main parts:

1. Theoretical Derivation
2. Numerical Calculation and Simulation
3. Experimental Measurement

For Part 1, an inversion formula for the spiral coil used in this experiment has been proposed, which enables the transformation of raw frequency data into the temperature dependence of London penetration depth.

For Part 2, an axis-symmetric approximation model of the spiral coil was simulated using Finite Element Method Magnetics (FEMM), while the full axis-asymmetric geometry was modeled in COMSOL. To enhance the reliability of the theoretical formula derived in this thesis, several comparisons were conducted between the simulation results and the theoretical results.

Figure 1.7: The picture of spiral coil used in this thesis. The design of the spiral coil is by Yoshihisa Iwashita(Osaka University).

In Part 3, we simultaneously measured the London penetration depths of two different Nb samples at extremely low temperatures. The network analyzer successfully detected frequency shifts near the critical temperature. We analyzed these shifts using a reverse method and estimated the London penetration depths at different temperatures.

Chapter 2

International Linear Collider

2.1 Overall Design of ILC

The International Linear Collider is a proposed high-precision linear accelerator designed to collide electrons and positrons at an initial energy of 250 GeV, with future energy scale up to 1 TeV. Utilizing 1.3 GHz SRF cavities, the ILC aims to achieve both high luminosity and energy efficiency. With polarized beams and an anticipated integrated luminosity of 400 fb^{-1} within its first four years, it is optimized for detailed studies of the Higgs boson and physics beyond the Standard Model.

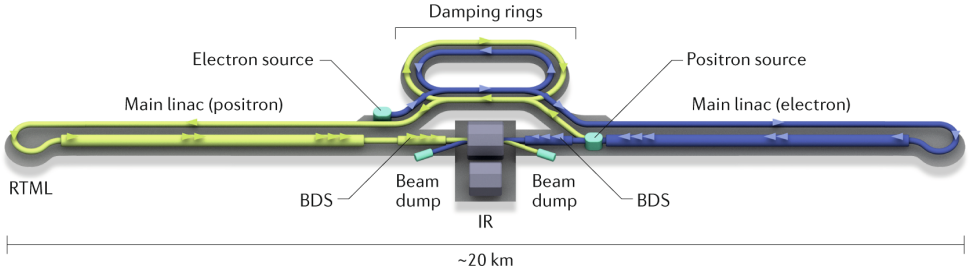

Figure 2.1: Design schematic of the International Linear Collider [20].

As shown in Figure 2.1, the ILC machine begins with prepared sources for both particle types: the electron source generates polarized electrons directly, while the positron source was generated by using a high-energy electron beam passing through a helical undulator to produce photons, which then generate positrons upon striking a target. Both particle species are first accelerated and injected into *damping rings*. After damping, the beams are extracted and sent into two symmetric superconducting linear accelerators that stretch over several kilometers (*main linacs*). Within these linacs, particles are accelerated using 1.3 GHz SRF cavities to their final collision energies. Finally, the electron and positron beams are precisely focused and brought into head-on collision at the central *interaction point*, which creates high-luminosity events. These events will be captured by the ILC detector and analyzed carefully to extract physical results such as Higgs boson couplings, mass, and decay modes, as well as electroweak parameters like the weak mixing angle and gauge boson self-interactions.

While the initial 250 GeV stage of the ILC serves as a Higgs factory with exceptional precision, increasing the collision energy opens access to a broader range of physics search

opportunities. At $\sqrt{s} = 350\,\text{GeV}$, the ILC can precisely measure the top quark mass and its electroweak couplings. Further extending the energy to 500 GeV enables ILC to direct detect the top Yukawa coupling and the Higgs boson self-coupling, both of which are inaccessible for current particle physics experiments. In addition to precision measurements, higher energies enhance the discovery potential for new particles predicted by theories beyond the Standard Model, such as supersymmetry or composite Higgs scenarios [18]. The clean background and high energy of the ILC make it uniquely suited for systematically exploring particle interactions that may remain inaccessible to hadron colliders [16].

2.2 Physics of ILC

2.2.1 Electroweak Symmetry Breaking

In the Standard Model, masses for both gauge bosons and fermions arise through spontaneous symmetry breaking (SSB), which is achieved by introducing a complex scalar doublet known as the Higgs doublet into the Lagrangian. When the Higgs doublet acquires a nonzero vacuum expectation value (VEV), the electroweak symmetry $SU(2)_L \times U(1)_Y$ is spontaneously broken down to the electromagnetic symmetry $U(1)_{\text{EM}}$. As a result, the $W^{\pm}$ and Z bosons acquire masses proportional to the VEV, while the photon remains massless. This phenomena is well described by a theory called Glashow-Weinberg-Salam (GWS) Theory. The Lagrangian of a complex scalar field coupled both to itself and to a non-abelian gauge field is written as:

$$\mathcal{L} = (D_\mu \phi)^\dagger (D^\mu \phi) - V(\phi) - \frac{1}{4} F^a_{\mu\nu} F^{a\,\mu\nu} \tag{2.1}$$

where D_μ is the covariant derivative in non-abelian gauge theory, $F^a_{\mu\nu}$ is the field strength tensor, and $V(\phi)$ is the scalar potential. $V(\phi)$ describes the self-interaction of the scalar field, and more importantly, it determines whether spontaneous symmetry breaking (SSB) occurs. If $V(\phi)$ has the minimal energy at nonzero $|\phi|$ point, the corresponding gauge symmetry will be spontaneously broken. Particularly, we can remove one physical degree by making the scalar potential a Mexican hat shape, where the removal of this degree of freedom is often described as the Goldstone boson being eaten by gauge field.

The mass of gauge bosons is generated from the covariant derivative term of equation (2.1). To demonstrate this, we first write down the covariant derivative when the scalar field is coupled with a SU(2) gauge boson A_μ and an U(1) gauge boson:

$$D_\mu = \partial_\mu - ig\tau^a A^a_\mu - i\frac{g'}{2} B_\mu \tag{2.2}$$

where τ^a is the generator of SU(2) group, and the index a runs from 1 to 3. Since the generators of SU(2) and U(1) act on different internal spaces, they commute with each other. Therefore, their coupling constants g and g' can be defined independently here. By using the above covariant derivative, we can derive the mass terms for gauge bosons by calculating the first term in equation (2.1):

$$(D_\mu \phi)^\dagger (D^\mu \phi) \ni \frac{1}{2} \begin{pmatrix} 0 & v \end{pmatrix} \left(g\tau^a A^a_\mu + \frac{g'}{2} B_\mu \right) \left(g\tau^b A^{b\mu} + \frac{g'}{2} B^\mu \right) \begin{pmatrix} 0 \\ v \end{pmatrix} \tag{2.3}$$

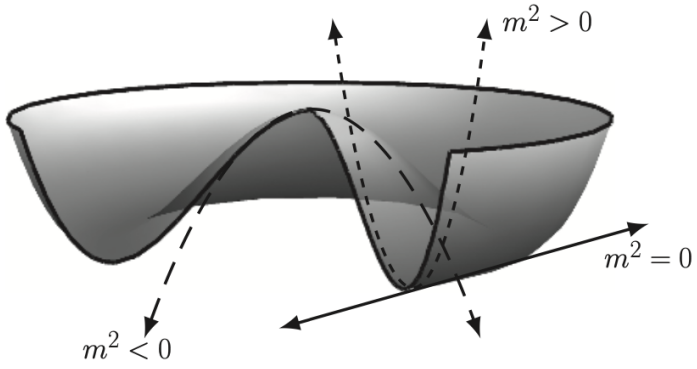

Figure 2.2: Mexican hat potential [21]. The mass squared of the particle is determined by the second derivative of the potential. At the origin, both the real and imaginary components of the scalar field correspond to tachyonic modes, as the second derivative is negative. At the minimum of the potential, the radial component corresponds to a massive scalar particle (dashed line), while the angular (or polar) component represents a massless scalar particle (solid line).

The complex scalar field in equation (2.3) has a nonzero vacuum expectation value $\frac{v}{\sqrt{2}}$, which will cause the square terms of gauge field to appear in the Lagrangian. We can calculate equation (2.3) explicitly by replacing the SU(2) generators by Pauli matrix($\tau^a = \frac{\sigma^a}{2}$):

$$(D_\mu\phi)^\dagger(D^\mu\phi) \ni \frac{1}{2}\frac{v^2}{4}\left[g^2(A^1_\mu)^2 + g^2(A^2_\mu)^2 + (-gA^3_\mu + g'B_\mu)^2\right] \tag{2.4}$$

Therefore, we observed three massive gauge bosons, and their mass squared values can be identified by the coefficients in front each terms. However, before the symmetry breaking, we have four degrees of freedom, where three comes from SU(2) group and one comes from U(1) group. The degree of freedom must not change before and after symmetry breaking, which means there must be a massless gauge boson exist. The expression of the massless gauge boson must be orthogonal to all the gauge boson fields in equation (2.4). This is because all three gauge boson fields in equation (2.4) are mass eigenstates, and therefore the fourth one must be orthogonal to all of them.

Gauge Boson	**Field Combination**	**Mass**
W^+_μ, W^-_μ	$\frac{1}{\sqrt{2}}(A^1_\mu \mp iA^2_\mu)$	$m_W = \frac{1}{2}gv$
Z^0_μ	$\frac{gA^3_\mu - g'B_\mu}{\sqrt{g^2+g'^2}}$	$m_Z = \frac{1}{2}v\sqrt{g^2+g'^2}$
Photon γ	$\frac{g'A^3_\mu + gB_\mu}{\sqrt{g^2+g'^2}}$	0

Table 2.1: Gauge bosons after electroweak symmetry breaking and their masses

The covariant derivative acts on fermion fields can be defined by using the mass eigenstates of gauge boson fields [22]. With the definition of *weak mixing angle* θ_w, the covariant derivative is simplified as:

$$D_\mu = \partial_\mu - i\frac{g}{\sqrt{2}}\left(W_\mu^+ T^+ + W_\mu^- T^-\right) - i\frac{g}{\cos\theta_w} Z_\mu \left(T^3 - \sin^2\theta_w Q\right) - ieA_\mu Q \tag{2.5}$$

$$\cos\theta_w = \frac{g}{\sqrt{g^2+g'^2}}, \qquad \sin\theta_w = \frac{g'}{\sqrt{g^2+g'^2}}. \tag{2.6}$$

where $T^\pm = \frac{1}{2}(\sigma^1 \pm i\sigma^2) = \sigma^\pm$ in the spinor representation of SU(2), and $T^3 = \sigma^3$ accordingly. $Q = T^3 + Y$ is recognized as the electric charge, where Y is the U(1) charge. With a specific chosen representation, we can calculate the U(1) charged coupled with different fermion fields by using the condition that Q must equal to -1 to produce the correct charge for electrons. Another very important observation in Standard Model Lagrangian is that the kinetic energy part of fermion fields can be decoupled as left-hand and right-hand part. This means we can write down the kinetic part of left-hand and right-hand fermions separately, and assign different gauge representation for them. Due to the experimental fact that only left-hand fermions couple to the W bosons, we assign the doublets of SU(2) to left-hand fermions while we assign the singlet of SU(2) to right-hand fermions. The results of all the U(1) charges coupled with different fermion fields are given in table 2.2.

Table 2.2: U(1) charge (Y) assignments for Standard Model fermions.

Fermion Type	**Field**	Q	Y
Lepton doublet	$\begin{pmatrix}\nu_L\\ e_L\end{pmatrix}$	$\begin{pmatrix}0\\ -1\end{pmatrix}$	$-\frac{1}{2}$
Quark doublet	$\begin{pmatrix}u_L\\ d_L\end{pmatrix}$	$\begin{pmatrix}\frac{2}{3}\\ -\frac{1}{3}\end{pmatrix}$	$\frac{1}{6}$
Right-handed electron	e_R	-1	-1
Right-handed up quark	u_R	$\frac{2}{3}$	$\frac{2}{3}$
Right-handed down quark	d_R	$-\frac{1}{3}$	$-\frac{1}{3}$

While the interaction between fermions and weak bosons arise from kinetic term of fermion fields, the mass of fermions arise from Yukawa Coupling terms. Yukawa coupling can be constructed from a gauge invariant coupling between fermions and scalar fields:

$$\mathcal{L} \ni -\lambda_e \overline{E}_L \cdot \phi\, e_R - \lambda_d \overline{Q}_L \cdot \phi\, d_R - \lambda_u \epsilon^{ab} \overline{Q}_{La} \cdot \phi_b^+ u_R + \text{h.c.} \tag{2.7}$$

where $\overline{E}_L$ and ϕ are SU(2) doublets, and they are contracted to form a gauge-invariant term. The introduction of the Higgs doublet is essential, because in the GWS theory, left-handed fermions transform as SU(2) doublets while right-handed fermions are SU(2) singlets. Without the introduction of this Higgs doublet, the Dirac mass terms are not Lorentz invariant. Furthermore, if the scalar field acquires a non-zero vacuum expectation value, we can replace the scalar field by its vacuum expectation value in equation (2.7):

$$\mathcal{L} \ni -\frac{1}{\sqrt{2}}\lambda_e v\, \bar{e}_L e_R - \frac{1}{\sqrt{2}}\lambda_d v\, \bar{d}_L d_R - \frac{1}{\sqrt{2}}\lambda_u v\, \bar{u}_L u_R + \text{h.c.} + \cdots \tag{2.8}$$

From the above Yukawa coupling terms, the masses of the fermions are identified as: $m_e = \frac{\lambda_e v}{\sqrt{2}}, \quad m_d = \frac{\lambda_d v}{\sqrt{2}}, \quad m_u = \frac{\lambda_u v}{\sqrt{2}}$. Where λ_i is called *Yukawa Coupling constants*. Then, the implementation of the other generations of quarks and leptons is straightforward.

2.2.2 Higgs Boson and Top Quark

The GWS theory shows the importance of the implementation of Higgs doublet into the theory of elementary particles, where we assumed that this complex scalar field has a non-zero vacuum expectation value. We can future explore this theory by assuming the vacuum fluctuation scenario. We can chose a specific gauge to the complex scalar field has the form:

$$\phi(x) = \frac{1}{\sqrt{2}} \begin{pmatrix} 0 \\ v + h(x) \end{pmatrix} \tag{2.9}$$

This gauge is called the *unitarity gauge*, in which $h(x)$ represents the Higgs field that characterizes vacuum fluctuations around the minimal points of scalar potential. Specifically, the Lagrangian and scalar potential take the following form:

$$\mathcal{L} = (D_\mu \phi)^\dagger (D^\mu \phi) + \mu^2 \phi^\dagger \phi - \lambda^2 (\phi^\dagger \phi)^2 \tag{2.10}$$

The scalar potential appears in the above Lagrangian has the Mexican hat distribution shows in Figure 2.2, where the minimal value appears at $v = (\frac{\mu^2}{\lambda})^{\frac{1}{2}}$. At the unitary gauge, the potential takes the form as equation (2.9) shows. Plug this expression of the scalar field into the Lagrangian we have:

$$\mathcal{L} = (D_\mu \phi)^\dagger (D^\mu \phi) - \mu^2 h^2 - \lambda v h^3 - \frac{1}{4}\lambda h^4 \tag{2.11}$$

where the mass of the Higgs boson can be identified as $m_h = \sqrt{2}\mu$. The Higgs field interactions in the above Lagrangian consist of a two-point interaction, a three-point interaction, and a four-point interaction. The mass of the Higgs boson is determined by μ. The gauge boson will obtain mass from the kinetic term as demonstrated in the previous section. Put them together, we obtained all the interactions in unitarity gauge:

$$\begin{aligned} \mathcal{L} = \frac{1}{2}(\partial_\mu h)^2 + \left[m_W^2 W^{\mu +} W_\mu^- + \frac{1}{2} m_Z^2 Z^\mu Z_\mu \right] \left(1 + \frac{h}{v}\right)^2 \\ - \frac{1}{2} m_h^2 h^2 - \sqrt{\frac{\lambda}{2}}\, m_h h^3 - \frac{1}{4}\lambda h^4 - m_f f \bar{f} (1 + \frac{h}{v}) \end{aligned} \tag{2.12}$$

where we have used mass eigenstates of gauge bosons to rewrite the kinetic terms. The final term denotes the Yukawa interaction responsible for generating fermion masses. The interaction terms in the above Lagrangian give rise to several fundamental Feynman vertices involving the Higgs boson. These include its couplings to the massive gauge bosons $W^\pm$ and Z, to fermion and anti-fermion pairs via Yukawa interactions, and to

itself through cubic and quartic self-interactions. The corresponding Feynman diagrams up to three-point interactions are illustrated below.

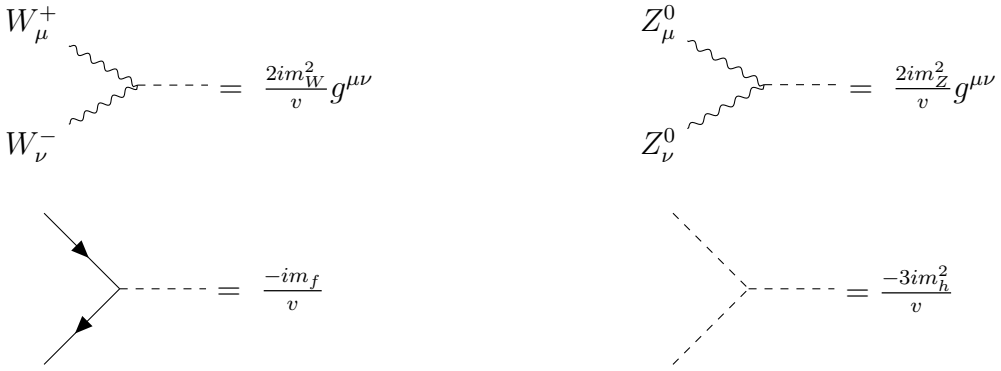

The masses of the W and Z bosons can be directly measured from experiments. The coupling g is given by the Fermi constant G_F as $g^2 = 8m_W^2 G_F/\sqrt{2}$. From this, the Higgs vacuum expectation value is calculated as $v = \left(\sqrt{2}G_F\right)^{-1/2} \approx 246\,\text{GeV}$. This is one of the reasons why the ILC was initially proposed as a future electron-positron collider operating at a center-of-mass energy of 250 GeV, which corresponds to the energy of the vacuum expectation value of the Higgs doublet.

Operating the ILC at energies above 250 GeV enables access to other significant Standard Model (SM) processes. Among the various Higgs boson couplings, two are inaccessible at 250 GeV energy scale: the top quark Yukawa coupling and the Higgs boson self-coupling. The top quark Yukawa coupling is of particular interest because the top quark is the heaviest particle in the Standard Model (SM), and its mass is directly proportional to this coupling constant. Within the SM framework, a large top quark mass implies a correspondingly large Yukawa coupling. If new physics is responsible for enhancing the top quark mass, deviations from the SM prediction may appear as corrections to the Yukawa coupling constant of the top quark. Therefore, precise measurements of the Yukawa coupling constant of the top quark serve as a sensitive probe of potential new physics beyond the Standard Model.

Moreover, the top quark's spin, weak interaction properties, and decay into polarized particles via $t \to bW$ provide many independent observables in $t\bar{t}$ production. An e^+e^- collider with beam polarization and sufficient energy, such as the ILC operating above the $t\bar{t}$ threshold at 500 GeV, can fully exploit these features. This makes top quark physics a sensitive probe for deviations from SM predictions and a powerful tool in the search for new physics.

Chapter 3

Theory of Superconductivity

3.1 London Theory

The London theory is a phenomenological framework introduced by Fritz and Heinz London in 1935 to explain key electromagnetic properties of superconductors. It provides a simplified yet remarkably successful description of two fundamental features of superconductivity : Zero Electrical Resistance and Expulsion of Magnetic Field. It is based on a two-fluid picture, in which electrons coexist in both normal and superfluid states. The electrons in the normal state are described by Ohm's law:

$$\mathbf{j}_n = \sigma_n \mathbf{E} \tag{3.1}$$

where σ_n represents the electrical conductivity of the normal component of the electron, defined by Drude conductivity. On the other hand, the electrons in the superfluid state are described by the super current and Newton's equation of motion :

$$\mathbf{j}_s = -en_s\mathbf{v}_s, \quad \frac{d\mathbf{v}_s}{dt} = \frac{\mathbf{F}}{m} = -\frac{e\mathbf{E}}{m} \tag{3.2}$$

where n_s is the number density of superfluid electrons, and $\mathbf{v}_s$ is the velocity of it. By differentiate both side on the equation of super current, we have:

$$\frac{\partial \mathbf{j}_s}{\partial t} = \frac{e^2 n_s}{m}\mathbf{E} \tag{3.3}$$

Which is the *First London Equation*. The second equation can be derived by taking the curl of the above equation, which gives :

$$\frac{\partial}{\partial t}\nabla \times \mathbf{j}_s = \frac{e^2 n_s}{m}\nabla \times \mathbf{E} = -\frac{e^2 n_s}{mc}\frac{\partial \mathbf{B}}{\partial t} \tag{3.4}$$

where we used Faraday's Law in the second step. Then integrate both side of the above equation with respect to time, we have :

$$\nabla \times \mathbf{j}_s = -\frac{e^2 n_s}{mc}\mathbf{B} \tag{3.5}$$

This is the *Second London Equation*. Note that when integrating with respect to time, the indefinite integral includes an integration constant, which must be determined by the

initial conditions. If we assume that both the magnetic field and the current are initially zero inside the superconductor, then this constant will be zero. However, to account for the observed Meissner effect that superconductors expel magnetic fields regardless of their previous magnetic history, London theory made a bold postulate that the integration constant always satisfy $\mathbf{C} = 0$ even if the magnetic field was present before the material entered the superconducting state. This assumption leads directly to the Second London Equation:

$$\nabla \times \mathbf{j}_s = -\frac{e^2 n_s}{mc}\mathbf{B}, \tag{3.6}$$

Taking the curl of the Ampere's law we find :

$$\nabla \times \nabla \times \mathbf{B} = -\frac{4\pi e^2 n_s}{mc^2}\mathbf{B} + \frac{4\pi}{c}\sigma_n \nabla \times \mathbf{E} = -\frac{4\pi e^2 n_s}{mc^2}\mathbf{B} \tag{3.7}$$

where the total current is the sum of super-current and normal current, and the curl of super-current has been replace by the *Second London Equation*. Also, the magnetic field is assumed to be stationary here so the time derivative of B is ignored. The curl of the curl of the magnetic field $\mathbf{B}$ simplifies to the Laplacian of $\mathbf{B}$, since $\nabla \cdot \mathbf{B} = 0$. Then equation(3.7) will reduce to a Helmholtz-type equation for the magnetic field $\mathbf{B}$:

$$\nabla^2 \mathbf{B} = \frac{1}{\lambda_L^2}\mathbf{B} \tag{3.8}$$

where λ_L is the *London Penetration Depth* defined as:

$$\lambda_L := \sqrt{\frac{mc^2}{4\pi e^2 n_s}} \tag{3.9}$$

The solution of equation (3.8) will be characterized by an exponential decay factor e^{-x/λ_L}, where x axis is perpendicular to the surface of a superconductor. The magnetic field decays exponentially as x increase. Therefore, the magnetic field is indeed zero inside the superconductor, and we reproduced Messiner effect by using London equations. Typically, λ_L for conventional superconductors ranges from about 30 nm (for pure Nb) to 100 nm (for Nb3Sn), while for high T_c superconductors it can reach several hundred nanometers.

London equations appear simple and effectively describe the fundamental phenomena of superconductivity. However, one important restriction should be noted: in the derivation of the London equations, it is assumed that both n_n and n_s are independent of space and time, which means their distributions are uniform and stationary. This is a significant restriction, which will be addressed by the Ginzburg–Landau theory introduced in the next section.

3.2 Ginzburg Landau Theory

The Ginzburg–Landau theory is the generalization of London theory. Unlike the London theory, which assumes a constant superfluid density, Ginzburg–Landau theory allows

for spatial variations. To be able to describe the spatially non-uniform distribution, Ginzburg and Landau included the gradient of ψ into the expression of free energy:

$$F[\psi] = \int d^3r \left[\alpha|\psi|^2 + \frac{\beta}{2}|\psi|^4 + \gamma\left(\nabla\psi\right)^* \cdot \nabla\psi\right] \tag{3.10}$$

where ψ is a one-particle wave function, and $|\psi|^2$ is interpreted as the local number density of superfluid particles at position $\vec{r}$. More importantly, $|\psi|$ is called *order parameter*, and the free energy $F[\psi]$ is a functional of $|\psi|$. The order parameter is a thermodynamic quantity that characterizes a phase transition. It is zero in the symmetric phase before the transition and non-zero in the broken-symmetry phase after the transition.

Like we minimize the action to derive Euler-Lagrangian equation, we can derive a differential equation for ψ by minimizes the functional $F[\psi]$. We start by varying ψ by $\psi(r) = \psi_0(r) + \delta\psi$, then the change of $F[\psi]$ due to the variation of $\psi(r)$ is given by:

$$\begin{aligned}
F[\psi_0 + \delta\psi] &= F[\psi_0] \\
&\quad + \int d^3r \left[\alpha\psi_0^*\delta\psi + \alpha\delta\psi^*\psi_0 + \beta\psi_0^*\psi_0^*\psi_0\delta\psi + \beta\psi_0\psi_0\psi_0^*\delta\psi^*\right. \\
&\quad \left. + \frac{\hbar^2}{2m^*}(\nabla\psi_0)^* \cdot \nabla\delta\psi + \frac{\hbar^2}{2m^*}(\nabla\delta\psi)^* \cdot \nabla\psi_0\right] + \mathcal{O}(\delta\psi, \delta\psi^*)^2 \\
&= F[\psi_0] + \int d^3r \left[\alpha\psi_0^*\delta\psi + \alpha\delta\psi^*\psi_0 + \beta\psi_0^*\psi_0^*\psi_0\delta\psi + \beta\psi_0\psi_0\psi_0^*\delta\psi^*\right. \\
&\quad \left. - \frac{\hbar^2}{2m^*}(\nabla^2\psi_0)^*\delta\psi - \frac{\hbar^2}{2m^*}\delta\psi^*\nabla^2\psi_0\right] + \mathcal{O}(\delta\psi, \delta\psi^*)^2
\end{aligned} \tag{3.11}$$

where we have used $\gamma = \frac{\hbar^2}{2m^*}$, and m^* is the effective mass of the particles forming the condensate. The second line is obtained by integrating the first line by parts. Since $\delta\psi$ is arbitrary, the coefficients in front of $\delta\psi$ and $\delta\psi^*$ must vanish. This leads to the following equation:

$$-\frac{\hbar^2}{2m^*}\nabla^2\psi + \alpha\psi + \beta|\psi|^2\psi = 0 \tag{3.12}$$

This is called Gross-Pitaevskii equation (GPE). GPE is a nonlinear Schrödinger-type equation that describes the ground state of a quantum system of identical bosons. It is formally analogous to the time-independent Ginzburg Landau equation, but it arises in the context of interacting superfluids rather than superconductivity. To describe superconductors, it is necessary to account for the electric charge of the particles that form the condensate. Although this charge is typically equal to the electron charge, we allow for the more general case in which the charge is not the electron charge. As a consequence, two modifications must be introduced into the Landau free energy functional $F[\psi]$. The first is that the canonical momentum operator must be replaced by $\frac{\hbar}{i}\nabla \;\rightarrow\; \frac{\hbar}{i}\nabla - \frac{q}{c}\mathbf{A}$. In other words, the gradient operator is modified to include the electromagnetic vector potential. The second is that the energy density of the magnetic field, $B^2/8\pi$, has to be considered when we solving any electric magnetic problem. After some manipulations, the Landau free energy functional $F[\psi]$ takes the form:

$$F[\psi, \mathbf{A}] \simeq \int d^3r \left[\alpha|\psi|^2 + \frac{\beta}{2}|\psi|^4 + \frac{1}{2m^*}\psi^*\left(\frac{\hbar}{i}\nabla - \frac{q}{c}\mathbf{A}\right)^2\psi + \frac{B^2}{8\pi}\right] \tag{3.13}$$

Note that the free energy functional $F[\psi]$ now depends on both $\psi(\mathbf{r})$ and $\mathbf{A}(\mathbf{r})$, which means that there are two fields over which the functional must be varied. When performing the variation with respect to one field, the other must be held fixed to ensure that the resulting change in $F[\psi]$ is only due to the variation of that specific field. By independently varying $\psi(\mathbf{r})$ and $\mathbf{A}(\mathbf{r})$, we obtain two coupled differential equations [23].

$$\frac{1}{2m^*}\left(\frac{\hbar}{i}\nabla - \frac{q}{c}\mathbf{A}\right)^2 \psi + \alpha\psi + \beta|\psi|^2\psi = 0, \tag{3.14}$$

$$\mathbf{j} = i\frac{q\hbar}{2m^*}\left((\nabla\psi^*)\psi - \psi^*\nabla\psi\right) - \frac{q^2}{m^*c}|\psi|^2\mathbf{A}. \tag{3.15}$$

Equations (3.14) and (3.15) are called the *Ginzburg-Landau equations*. In the limit that $\psi(\mathbf{r})$ is uniform distributed in space, we have $\nabla\psi^* = \nabla\psi = 0$. Then equation (3.15) reduces to:

$$\mathbf{j} = -\frac{q^2}{m^*c}|\psi|^2\mathbf{A}. \tag{3.16}$$

This equation should reproduce London equation, therefore we have the normalization condition for $\psi(\mathbf{r})$: $\frac{q^2|\psi|^2}{m^*} = \frac{e^2 n_s}{m}$. Take the convention based on flux quantization experiments that $m^* = 2m_e,$, and $q = -2e$, we can now write the penetration depth as:

$$\lambda = \sqrt{\frac{mc^2}{4\pi e^2 n_s}} = \sqrt{\frac{mc^2}{8\pi e^2|\psi|^2}} \simeq \sqrt{\frac{mc^2}{8\pi e^2(-\frac{\alpha}{\beta})}} \tag{3.17}$$

The Ginzburg Landau theory provides a phenomenological framework for describing superconductivity using a complex order parameter field coupled to the electromagnetic field. It captures key features of superconductors such as critical temperature and London penetration depth. Importantly, the London theory is recognized as a special case of the Ginzburg Landau theory in the limit where the order parameter is spatially uniform. In this regime, the Ginzburg Landau equations reduce to the London equations, which shows the consistency between the two theories.

While the Ginzburg–Landau (GL) theory provides a result of London penetration depth of superconductors (Equation 3.17), it still has limitations. It is a phenomenological model, which means it does not explain the London penetration depth from a microscopic perspective. To address this shortcoming, the Bardeen–Cooper–Schrieffer (BCS) theory was proposed to calculate parameters α and β in equation (3.17) in a microscopic approach.

3.3 BCS Theory

The Bardeen-Cooper-Schrieffer(BCS) theory is a non-relativistic quantum field theory which explains conventional superconductivity as a phenomenon arising from the formation of Cooper pairs of electrons [24]. It is also a mean-field theory that approximates the complex many-body electron interaction system with an effective average field. To derive the Hamiltonian of BCS theory, we start by replacing the self-interaction energy term of a many-particles Coulomb interaction system with a contact interaction modeled

by a delta function: $\frac{e^2}{|\vec{x}-\vec{y}|} \to -g\,\delta^3(\vec{x}-\vec{y})$. After integrating over $\vec{y}$, we obtain the following form of the Hamiltonian for the interacting many-particle system:

$$H = \int d^3\vec{x} \left\{ \sum_{\sigma=\uparrow\downarrow} \psi^*_\sigma(\vec{x}) \left(-\frac{\vec{D}^2}{2m} \right) \psi_\sigma(\vec{x}) - g\,\psi^*_\uparrow(\vec{x})\psi^*_\downarrow(\vec{x})\psi_\downarrow(\vec{x})\psi_\uparrow(\vec{x}) \right\} \tag{3.18}$$

where $\vec{D} = \vec{\nabla} - ie\vec{A}(\vec{x})$, and $\vec{A}(\vec{x})$ is an external vector potential field. The summation is over all possible spin states of the electrons. The order parameter is defined as the expectation value of fermion pair annihilation operators:

$$\varphi(\vec{x}) \equiv \langle \hat{\psi}_\uparrow(\vec{x})\hat{\psi}_\downarrow(\vec{x}) \rangle = \frac{\mathrm{Tr}\left[\hat{\psi}_\uparrow(\vec{x})\hat{\psi}_\downarrow(\vec{x}) e^{-\beta(\hat{H}-\mu\hat{N})}\right]}{\mathrm{Tr}\left[e^{-\beta(\hat{H}-\mu\hat{N})}\right]} \tag{3.19}$$

The gauge transformation takes as: $\psi(\vec{x}) \to e^{i\theta(\vec{x})}\psi(\vec{x})$, and $\varphi(\vec{x}) \to e^{2i\theta(\vec{x})}\,\varphi(\vec{x})$, which corresponds to a local phase rotation. The above Hamiltonian is gauge invariant if the vector potential transform as: $\vec{A}(\vec{x}) \to \vec{A}(\vec{x}) + \frac{1}{e}\nabla\theta(\vec{x})$. In the case of the Higgs mechanics, when the $SU(2)_L \times U(1)_Y$ gauge symmetry is spontaneously broken, the Higgs doublet acquires a non-zero vacuum expectation value. Similarly, below the critical temperature, the order parameter in a superconductor acquires a non-zero vacuum expectation value, leading to the spontaneous breaking of the $U(1)$ gauge symmetry.

To recast the four-fermion interaction (quartic term) into a bilinear form, we introduce an auxiliary field defined by $\phi = g\psi_\downarrow(\vec{x})\psi_\uparrow(\vec{x})$. With the auxiliary field, we can rewrite the Hamiltonian as:

$$\begin{aligned} H = \int d^3\vec{x} \Bigg\{ & \sum_{\sigma=\uparrow\downarrow} \psi^*_\sigma(\vec{x}) \left(-\frac{\vec{D}^2}{2m} \right) \psi_\sigma(\vec{x}) \\ & - \phi^*(\vec{x})\psi_\downarrow(\vec{x})\psi_\uparrow(\vec{x}) - \phi(\vec{x})\psi^*_\uparrow(\vec{x})\psi^*_\downarrow(\vec{x}) + \frac{1}{g}|\phi(\vec{x})|^2 \Bigg\} \end{aligned} \tag{3.20}$$

The variation of the Hamiltonian in equation (3.20) with respect to ϕ and ϕ^* gives:

$$\frac{\partial H}{\partial \phi} = -\psi^*_\uparrow(\vec{x})\psi^*_\downarrow(\vec{x}) + \frac{1}{g}\phi^*(\vec{x}) = 0 \tag{3.21}$$

$$\frac{\partial H}{\partial \phi^*} = -\psi_\downarrow(\vec{x})\psi_\uparrow(\vec{x}) + \frac{1}{g}\phi(\vec{x}) = 0 \tag{3.22}$$

These equations show that Hamiltonian in equation (3.20) is equivalent to the original quartic interaction Hamiltonian. To quantize the Hamiltonian, we apply the standard second quantization: $\psi_\sigma \to \hat{\psi}_\sigma$, $\psi^*_\sigma \to \hat{\psi}^\dagger_\sigma$, $\phi \to \hat{\phi}$, $\phi^* \to \hat{\phi}^\dagger$. Moreover, if $\vec{A}(\vec{x}) = \vec{0}$, we can use mean field theory: $\hat{\phi}(\vec{x}) \to \varphi \equiv \langle\hat{\phi}(\vec{x})\rangle$, which replaces the expectation value of auxiliary field with the order parameter. After applying the mean field approximation, the effective Hamiltonian can be expressed as:

$$H_{eff} \simeq \int d^3\vec{x} \left\{ \sum_\sigma \hat{\psi}^\dagger_\sigma \left(\frac{-\vec{\nabla}^2}{2m} - \mu \right) \hat{\psi}_\sigma - \varphi^*\hat{\psi}_\downarrow\hat{\psi}_\uparrow - \varphi\hat{\psi}^\dagger_\uparrow\hat{\psi}^\dagger_\downarrow + \frac{1}{g}|\varphi|^2 \right\} \tag{3.23}$$

The Fourier expansion of the field operator takes the form:

$$\hat{\psi}_\sigma(\vec{x}) = \int \frac{d^3\vec{k}}{(2\pi)^3}\, e^{i\vec{k}\cdot\vec{x}}\, \hat{c}(\vec{k},\sigma) \tag{3.24}$$

where $\hat{c}$ is the momentum-space annihilation operator, and $\hat{c}^\dagger$ is the corresponding creation operator. Substituting this expression into the Hamiltonian and integrating over $\vec{x}$, we obtain the following result:

$$\hat{H}_{\text{eff}} \simeq \int \frac{d^3\vec{k}}{(2\pi)^3} \left\{ \sum_\sigma \xi_{\vec{k}}\, \hat{c}^\dagger(\vec{k},\sigma)\hat{c}(\vec{k},\sigma) - \varphi^*\, \hat{c}(-\vec{k},\downarrow)\hat{c}(\vec{k},\uparrow) - \varphi\, \hat{c}^\dagger(\vec{k},\uparrow)\hat{c}^\dagger(-\vec{k},\downarrow) \right\} \tag{3.25}$$

Here we defined: $\xi_{\vec{k}} = \frac{\vec{k}^2}{2m} - \mu = \frac{\vec{k}^2 - k_F^2}{2m}$, where k_F is the fermi momentum. The effective Hamiltonian can be expressed in a diagonal form in terms of $\hat{a}$ and $\hat{a}^\dagger$ by applying the Bogoliubov transformations:

$$\begin{cases} \hat{c}^\dagger(\vec{k},\uparrow) = \mathcal{U}_{\vec{k}}\hat{a}_0^\dagger(\vec{k}) + \mathcal{V}_{\vec{k}}^*\hat{a}_1(\vec{k}) \\ \hat{c}(-\vec{k},\downarrow) = -\mathcal{V}_{\vec{k}}\hat{a}_0^\dagger(\vec{k}) + \mathcal{U}_{\vec{k}}^*\hat{a}_1(\vec{k}) \end{cases}$$

$$\begin{cases} \hat{c}(\vec{k},\uparrow) = \mathcal{U}_{\vec{k}}^*\hat{a}_0(\vec{k}) + \mathcal{V}_{\vec{k}}\hat{a}_1^\dagger(\vec{k}) \\ \hat{c}^\dagger(-\vec{k},\downarrow) = -\mathcal{V}_{\vec{k}}^*\hat{a}_0(\vec{k}) + \mathcal{U}_{\vec{k}}\hat{a}_1^\dagger(\vec{k}) \end{cases}$$

where the Bogoliubov coefficients have the diagonalization conditions: $2\,\xi_{\vec{k}}\mathcal{U}_{\vec{k}}\mathcal{V}_{\vec{k}} - \varphi\mathcal{U}_{\vec{k}}^2 + \varphi^*\mathcal{V}_{\vec{k}}^2 = 0$, $2\,\xi_{\vec{k}}\mathcal{U}_{\vec{k}}^*\mathcal{V}_{\vec{k}}^* - \varphi^*(\mathcal{U}_{\vec{k}})^2 + \varphi(\mathcal{V}_{\vec{k}})^2 = 0$. The diagonalized Hamiltonian takes the simple form:

$$\hat{H}_{\text{eff}} \simeq \int \frac{d^3\vec{k}}{(2\pi)^3}\, E_{\vec{k}} \left(\hat{a}_0^\dagger\hat{a}_0 + \hat{a}_1^\dagger\hat{a}_1 \right) \tag{3.26}$$

Going to momentum space and using the Bogoliubov transformation, the order parameter becomes:

$$\varphi = g\int \frac{d^3\vec{k}}{(2\pi)^3} \left\langle \hat{c}_{-\vec{k},\downarrow}\hat{c}_{\vec{k},\uparrow} \right\rangle = g\int \frac{d^3\vec{k}}{(2\pi)^3}\, \mathcal{U}_{\vec{k}}\mathcal{V}_{\vec{k}} \left(1 - 2f(E_{\vec{k}})\right) \tag{3.27}$$

where $f(E_{\vec{k}})$ is the fermi distribution and the Bogoliubov coefficients $\mathcal{U}$ and $\mathcal{V}$ can be solved from the diagonalization conditions. If the U(1) symmetry is spontaneously broken, the order parameter will acquire an non-zero vacuum expectation value, which gives us the gap equation:

$$\frac{2}{gV_0} = \int \frac{d^3\vec{k}}{(2\pi)^3}\, \frac{1}{E_{\vec{k}}} \tanh\left(\frac{\beta E_{\vec{k}}}{2}\right) \tag{3.28}$$

where V_0 is the total volume of the system and $E_{\vec{k}} = \sqrt{\xi_{\vec{k}}^{\,2} + \Delta(T)^2}$. $\Delta(T)$ is the energy gap, and $\xi_{\vec{k}}$ is the single-particle energy relative to the Fermi energy level, defined as $\xi_{\vec{k}} = \epsilon_{\vec{k}} - \mu$. In the case of weak-coupling BCS theory, the integral region of equation(3.28) is taking to be the vicinity of fermi surface. This is because only those electrons with the energy around fermi surface can form cooper pairs. Thus the integral is simplified by:

$$\int \frac{d^3\vec{k}}{(2\pi)^3} \simeq \int_{k_F-\epsilon}^{k_F+\epsilon} \frac{d|\vec{k}|}{(2\pi)^3} \times 4\pi k_F^2 \equiv \int_{-\omega_c}^{\omega_c} d\xi_{\vec{k}}\, D(E_F) \tag{3.29}$$

where $|\vec{k}| \simeq k_F$, $\xi_{\vec{k}} = \frac{\vec{k}^2}{2m}$, and ω_c is the energy cut-off. Performing the integral, we can derive the following equation:

$$k_B T_c \simeq \frac{2e^{\gamma_E}}{\pi}\,\omega_c \exp\left(-\frac{1}{gV_0 D(E_F)}\right) \simeq 1.13\,\omega_c \exp\left(-\frac{1}{gV_0 D(E_F)}\right) \tag{3.30}$$

where γ_E is the Euler constant. From the above equation, we can determine the expression for the critical temperature of the superconductor. Furthermore, the temperature dependence of the London penetration depth can be determined from the following equation:

$$1 - \left[\frac{\lambda(0)}{\lambda(T)}\right]^2 = -\frac{2}{3\rho}\int k^2 \frac{\partial f(E_{\vec{k}})}{\partial E_{\vec{k}}}\frac{d^3k}{(2\pi)^3} \tag{3.31}$$

This equation can be obtained by using a semiclassical approach [25]. Inside this equation, $E_{\vec{k}}$ has the same definition with equation (3.28), and $\Delta(T)$ is determined from equation (3.28). $f(E_{\vec{k}})$ is the Fermi-Dirac distribution function. In the low temperature limit, the solution of equation (3.31) is indistinguishable with the following expression [40]:

$$\lambda(T) = \frac{\lambda(0)}{\sqrt{1-T^4}}, \tag{3.32}$$

This equation is well known as the empirical formula for London penetration depth temperature dependence. In this thesis, we want to determine the London penetration depth at 0 K, and equation (3.32) is very accurate when the temperature is close to 0 K. Therefore, instead of using a more complicated solution of equation (3.31), this thesis used equation (3.32) to fit the experimental data in Chapter 8.

Chapter 4

Mathematical Preliminaries

In this chapter, we review some basic mathematical tools used in this research.

1. Section 1 reviews the procedure for obtaining the magnetic vector potential using the Green's function method.
2. Section 2 reviews the integral representation of the Legendre function used in this research.
3. Section 3 reviews the integral representation of the Bessel function used in this research.
4. Section 4 summarizes the basic concept of the Hankel transformation, along with a useful identity applied in this research.

In this research, the integral representations reviewed in this chapter are used to convert the magnetic vector potential obtained by the Green's function method into that obtained by the Hankel transformation, which demonstrates the consistency between the two different approaches and enhances the reliability of the solutions obtained from both.

4.1 Green's Function Solution to Maxwell's Equations

Maxwell's equations describe the fundamental laws governing electric and magnetic fields. They consist of a set of four partial differential equations, which form the theoretical foundation of classical electrodynamics, optics, and electromagnetic wave theory. With the potential theory formalism [26], Maxwell's equations can be written in a very neat form in different gauge choices. In this research, we use the Maxwell's equations in Coulomb gauge (div$\vec{A}$=0):

$$\nabla^2 \vec{A} = -\mu_0 \vec{J} \tag{4.1}$$

where $\vec{J}$ is an arbitrary current density. In an inductance experiment, we consider the configuration that the coil was placed below the sample by a distance h. By separating the coil current density from the sample explicitly, we have:

$$\vec{J} = \vec{J}_{\text{coil}} + \vec{J}_{\text{sample}} \tag{4.2}$$

If we assume the supercurrent density obeys Ohm's law, then $\vec{J}_{\text{sample}}$ can be written as:

$$\vec{J}_{\text{sample}} = i\omega\sigma\vec{A}\omega \tag{4.3}$$

where $\sigma = \frac{1}{\omega\mu_0\lambda^2}$ is the imaginary part of the complex conductivity in London regime [17].

Equation (4.3) is nothing but the combination of two London equations. So this assumption is highly reasonable when the sample is at Meissner state. We can solve equation (4.1) by using the Green's function:

$$\left(\nabla^2 + k^2\right) G(\vec{r}, \vec{r'}) = -\delta^3(\vec{r} - \vec{r'}) \tag{4.4}$$

$$k^2 \equiv i\mu_0\omega\sigma_\omega \tag{4.5}$$

Equation (4.4) can be solved by using the Fourier transform of Green's function(equation (4.6)), the solution was given by equation (4.7) and equation (4.8) respectively:

$$G(\vec{r}, \vec{r'}) = \frac{1}{(2\pi)^{3/2}} \int g(\vec{s}) e^{i\vec{s}\cdot(\vec{r}-\vec{r'})}\, d^3s \tag{4.6}$$

$$g(\vec{s}) = \frac{-1}{(2\pi)^{3/2}} \frac{1}{s^2 - k^2} \tag{4.7}$$

$$G(\vec{r}, \vec{r'}) = \frac{-1}{4\pi} \frac{e^{-ik|\vec{r}-\vec{r'}|}}{|\vec{r} - \vec{r'}|} \tag{4.8}$$

where equation (4.8) can be derived by using Residue theory. The pole can be chosen as $s = \pm i\epsilon$, and ϵ is an infinitesimal parameter. When performing the residue calculation to derive $G(\vec{r}, \vec{r'})$, we always choose the contour such that the analytic part of the integrand vanishes at infinity. This indicates that the solution obtained by this method is only applicable to cases where the vector potential vanishes at infinity. Using this Green's function, the vector potential can be calculated as

$$\vec{A}(\vec{r}) = \frac{\mu_0}{4\pi} \iiint \frac{e^{-ik|\vec{r}-\vec{r'}|}}{|\vec{r} - \vec{r'}|} \vec{J}_{\text{coil}}(\vec{r'})\, d^3r' \tag{4.9}$$

Equation (4.9) is a very general expression in the sense that it only requires the current density $\vec{J}_{coil}$. It is not limited to axial symmetric configurations and can therefore also be applied to solve non-axial symmetric problems. In the region that the coil is present and the sample is not, the solution is given by:

$$\vec{A}(\vec{r}) = \frac{\mu_0}{4\pi} \iiint \frac{1}{|\vec{r} - \vec{r'}|} \vec{J}_{\text{coil}}(\vec{r'})\, d^3r' \tag{4.10}$$

Equation (4.10) can be used to calculate the inhomogeneous solution of Maxwell's equations under the assumption that the magnetic vector potential vanishes at infinity.

4.2 Integral Representation of the Legendre Function

In this section, we will review the integral representation of Bessel function used in this research and some related mathematics of it.

With the Green's function introduced in the previous section, we derive the solution to Maxwell's equations under the boundary condition that the magnetic vector potential vanishes at infinity. In this study, we use a specific integral representation of the Legendre function of the second kind to demonstrate the equivalence between the solution obtained via the Green's function and that derived from the Hankel transformation.

By using formulas (9.33) and (9.34) from Appendix, we can write the Legendre Function of the first kind in an alternative form. This form turns out to be particularly useful for obtaining the integral representation of Legendre function of the second kind. Once we determine the expression of Legendre function of the first kind, we can use equation (9.34) to construct another linear independent solution of Legendre equation. The two linear independent solutions of Legendre equation with hypergeometric function can be expressed in the following way:

$$P_n(t) = t^n F\left(-\frac{n}{2}, \frac{1-n}{2}; 1; 1-\frac{1}{t^2}\right) \tag{4.11}$$

$$Q_n(t) = \frac{\sqrt{\pi}}{(2t)^{n+1}} \frac{\Gamma(n+1)}{\Gamma(n+3/2)} F\left(1+\frac{n}{2}, \frac{1+n}{2}; n+\frac{3}{2}; \frac{1}{t^2}\right) \tag{4.12}$$

where the Gama function together with the 2^{-n-1} factor in $Q_n(t)$ are normalization factors. Under this normalization, it can give us a simple result of integral representation.

$$Q_n(z) = \frac{1}{2^{n+1}} \int_{-1}^{1} \frac{(1-t^2)^n}{(z-t)^{\nu+1}}\, dt \tag{4.13}$$

The explicit derivation of the above expression can be found in the Appendix. We could extend this integral to the complex plane and allow n takes non-integer values. If n is not an integer, i.e., $n = \nu$, the term $(1-t^2)^n$ introduces a branch cut between the branch points $t = \pm 1$. The contour in the complex plane can be chosen such that the integral vanishes beside the path from -1 to 1. One of the choice is shown in Figure 4.1. Along this contour, the integrand on the path above the branch cut and the path below it will differ by a factor of $e^{2\pi i}$, since the integration passes through the branch cut. The two small circles around the branch points will not contribute. The pole at $t = z$ lies outside the contour, since the Hypergeometric function is defined under the condition $\left|\frac{1}{z^2}\right| < 1$. Note that the contour below the branch cut introduces a minus sign in the integrand to match the sign of the original integral. The final expression of the integral representation of Legendre function of the second kind in complex plane can be expressed as:

$$Q_\nu(z) = \frac{2^{-\nu}}{4i \sin \nu\pi} \oint_C \frac{(t^2-1)^\nu}{(t-z)^{\nu+1}}, dt \tag{4.14}$$

Amazingly, it has the same form with the Schlaefli integral for the Legendre function of the first kind, which is given by the following equation(derivation can be found in the

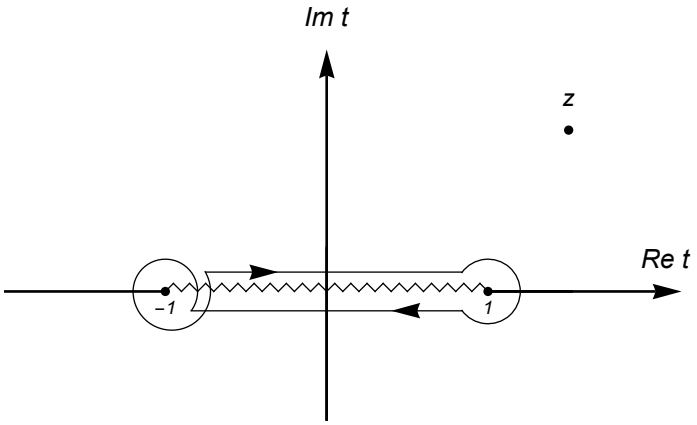

Figure 4.1: Contour for Schlaefli integral in the complex t-plane.

Appendix):

$$P_v(x) = \frac{2^{-v}}{2\pi i} \oint_C \frac{(t^2-1)^v}{(t-x)^{v+1}}\, dt \tag{4.15}$$

Equation (4.14) has many applications in solving practical problem. But in this research we will use an alternative expression of equation (4.14):

$$Q_v(z) = \frac{1}{\sqrt{2}} \left\{ \int_0^\pi dt\, \frac{t\, \cos\left(v+\frac{1}{2}\right)}{(z-\cos t)^{1/2}} - \cos v\pi \int_0^\infty dt\, \frac{e^{-(v+\frac{1}{2})t}}{(z+\cosh t)^{1/2}} \right\} \tag{4.16}$$

Equation (4.16) can be proved by making a change of variable in Equation (4.14):

$$z \to u(z) = \frac{1-z^2}{2(x-z)} \tag{4.17}$$

This transformation introduces a branch cut between two points, and the integral is rewritten over a new contour that encircles the branch point without crossing it. By parameterizing this contour appropriately and simplifying the resulting expression using properties of square roots on different Riemann sheets, equation (4.16) can be obtained.

4.3 Integral Representation of the Bessel Function

To show the equivalence between the solution obtained from Hankel transformation and Green's function, we need another useful identity comes from the integral representation of Bessel function. In this section we will briefly review the integral representation of Bessel function used in this research.

In many physical problems possessing cylindrical or spherical symmetry, the resulting differential equations reduce to a form known as the Bessel differential equation. The standard form of the Bessel equation of order ν is given by:

$$z^2 \frac{d^2y}{dz^2} + z\frac{dy}{dz} + (z^2-\nu^2)y = 0, \tag{4.18}$$

We can apply series solution method to this equation just like we did in Hypergeometric equation in the Appendix. The solution of this differential equation $y(z)$ is called the

Bessel function, and ν is a real or complex parameter called the order of the Bessel function. Bessel functions play a crucial role in various branches of mathematical physics, including electromagnetic theory, wave propagation, and quantum mechanics.

The two linearly independent solutions of Equation(4.18) are defined as the Bessel function of the first kind $J_\nu(z)$ and the Bessel function of the second kind $Y_\nu(z)$, respectively. In this research, the integral representation of the Bessel function of the first kind will be used. The Frobenius solution of the Bessel function of the first kind are given by:

$$J_n(z) = \sum_{s=0}^{\infty} \frac{(-1)^s}{s!(n+s)!} \left(\frac{z}{2}\right)^{n+2s}. \tag{4.19}$$

Additional, an important integral representation of Bessel function of the first kind is given by:

$$J_\nu(z) = \frac{\Gamma\left(\frac{1}{2}-\nu\right)\left(\frac{z}{2}\right)^\nu}{2\pi i\,\Gamma\left(\frac{1}{2}\right)} \int_C e^{izt}(t^2-1)^{\nu-\frac{1}{2}}\,dt. \tag{4.20}$$

This is Hankel representation. The complete derivation of this integral representation can be found in Appendix. If we let $\nu = 0$, we obtain the special case of it:

$$J_0(\omega) = \frac{1}{2\pi} \int_{-\pi}^{\pi} e^{i\omega\cos\theta}\,d\theta \tag{4.21}$$

where ω is defined as:

$$\omega = \sqrt{z^2 + z'^2 - 2zz'\cos\phi}. \tag{4.22}$$

where z, z' and ϕ are all complex variables. This representation naturally arises in problems with axial symmetry, and it reflects the close connection between Bessel function and Fourier transformation. It is also sometimes referred to as Parseval's integral in the literature. This integral representation is particularly useful in various physical applications, including the calculation of the magnetic vector potential in cylindrical coordinates. One of the important addition theorems come out of this integral representation is the following formula [28]:

$$\int_0^\infty e^{-at} J_\nu(bt) J_\nu(ct)\,dt = \frac{1}{\pi\sqrt{bc}} Q_{\nu-\frac{1}{2}}\left(\frac{a^2+b^2+c^2}{2bc}\right) \tag{4.23}$$

This formula is a classical result in the theory of special functions and it has applications in many physical problems, particularly in the axis-symmetric case. The appearance of the Legendre function $Q_{\nu-1/2}$ reflects the underlying axial symmetry of the problem. In this research, the parameters a, b, and c are assumed to be positive real numbers. The derivation of this formula is also provided in the Appendix. Although the derivation process is somewhat complicated, it originates from a very simple integral representation introduced in the Appendix (Poisson integral representation). In chapter 5, we will apply this formula to the magnetic vector potential solution of Maxwell's equations derived from Green's function.

4.4 Hankel Transformation

The Hankel transformation is a powerful integral transform commonly used in problems possessing general axial symmetry. It is particularly useful for solving Maxwell's

equations possessing the axial symmetric current in cylindrical coordinates, where the axial symmetry simplifies the mathematical treatment significantly. The Hankel transform can be regarded as a two dimensional Fourier transformation, or as the the radial analogue of the Fourier transform replacing the plane wave basis with Bessel functions, which naturally arise in systems with circular or cylindrical source distribution. In the context of this research, the Hankel transformation provides an efficient method to analyze the electromagnetic fields generated by current distributions with rotational symmetry along z axis, such as pancake coils or circular loops. The use of the Hankel transform is essential for converting partial differential equations into a simple form of ordinary differential equations. The Hankel transformation and inverse Hankel transformation are defined respectively as follows [29]:

$$\tilde{f}_\nu(k) = \int_0^\infty r J_\nu(kr) f(r)\, dr, \quad f(r) = \int_0^\infty k J_\nu(kr) \tilde{f}_\nu(k)\, dk. \tag{4.24}$$

where $J_\nu(kr)$ is the Bessel function of the first kind of order ν. The inverse Hankel transform allows for reconstructing the physical field configuration from its transform representation. In the following sections, we will call this representation the Hankel transform representation. It turns out that in the Hankel transform representation, we can analytically solve Maxwell's equation in different regions, and calculate the boundary condition coefficients of the solutions in a very simple way. To see why, we introduce another useful relation hold in Hankel transformation:

$$\int_0^\infty dr\, r J_\nu(kr) \left(\frac{\partial^2}{\partial r^2} + \frac{1}{r}\frac{\partial}{\partial r} - \frac{\nu^2}{r^2} \right) f(r) = -k^2 \tilde{f}_\nu(k) \tag{4.25}$$

This property is particularly useful for solving partial differential equations with cylindrical symmetry, as it allows the radial part of the Laplacian operator to be replaced by a simple multiplication by $-k^2$ in the Hankel transform space. In this research, we can use Hankel transformation to solve all Maxwell's equations with axis-symmetric inhomogeneous term. The formula derived from the integral representation of Legendre function of the second kind and the integral representation of Bessel in last section, serves as a double check, which will give the exactly same result with Hankel transformation. Moreover, although Hankel transformation is very powerful in solving problems with axis-symmetric current distributions, it can not be applied in spiral current distribution case because the current distribution in spiral coil dose not possess the axial symmetry. Therefore the approach using Green's function can not be completely replaced by Hankel transformation in this research.

Chapter 5

Derivation of Inversion Formula for Different Coils

In this section, the analytical solutions of Maxwell's equations with different coils will be presented.

To validate the solution obtained from Green's function and integral representation of special functions, the analytical solution in the case of Pancake coil is revisited, and the result of inductance reported in the previous study has been successfully reproduced [17]. In order to derive the analytical solutions for spiral coil, an approximation model for spiral coil was proposed in this thesis. For axis-asymmetric case, the Green's function solution to Maxwell's equations in the case of Archimedean spiral coil were calculated as well. Moreover, a parametrized inductance based on the approximation model of spiral coil was proposed to account for the effect from finite cross-section size and axial asymmetry of the coil.

5.1 The General Theory for Axis-Symmetric Coil

In this section, we review the theoretical approach for calculating the magnetic vector potential generated by axis-symmetric currents together with a bulk superconducting sample. An axis-symmetric coil refers to a coil structure that is invariant under rotation along the z-axis in cylindrical coordinates. Due to this symmetry, the only nonzero components of current vector is along θ direction:

$$J(r,z) = 0 \cdot \hat{r} + J_\theta(r,z)\hat{\theta} + 0 \cdot \hat{z} \tag{5.1}$$

Under this assumption, the vector potential $\vec{A}$ only possesses a nonzero component along the θ direction, i.e., $A_\theta(r,z)$, while the r and z components vanish. This is because the source current does not have the r and z components.

$$A(r,z) = 0 \cdot \hat{r} + A_\theta(r,z)\hat{\theta} + 0 \cdot \hat{z} \tag{5.2}$$

We can use the following formula to calculate $A_\theta(r,z)$ and J_θ respectively:

$$A_\theta(r,z) = A(r,z) \cdot \hat{\theta} \tag{5.3}$$

$$J_\theta(r,z) = J(r,z)\cdot\hat{\theta} \tag{5.4}$$

This simplification significantly reduces the complexity of solving Maxwell's equations. The induced screening current density on the sample is given by the relation:

$$\vec{J}_{\rm s} = \sigma\vec{E} = i\omega\sigma A(r,z)\,\hat{\theta}, \tag{5.5}$$

where σ is the imaginary part of complex conductivity of the superconductor(In high frequency limit, the real part of σ is nearly zero [1]).

The Maxwell's equations to the coil current J_θ and a superconducting sample under a coil are determined by the Heaviside function in cylindrical coordinates:

$$\nabla^2 A_\theta(r,z) = -\mu_0\left[J_\theta(r,z) + i\omega\sigma H_d(-z)A_\theta(r,z)\right] \tag{5.6}$$

In this expression, $H_d(z)$ denotes the Heaviside step function, which takes the value of unity within the region $0 \le z \le d$, and vanishes outside this interval:

$$H_d(z) = \begin{cases} 1, & 0 < z < d \\ 0, & \text{else} \end{cases} \tag{5.7}$$

where d represents the thickness of the sample. By using a complex length defined as $\ell \equiv \sqrt{\frac{i}{\mu_0\sigma\omega}}$, equation (5.5) can be rewritten as:

$$\vec{J}_{\rm s} = -\frac{1}{\mu_0\ell^2}A(r,z), \tag{5.8}$$

where the complex length ℓ will be reduced to London penetration depth at low temperature. With equation (5.8), Maxwell's equations can now be expressed explicitly in cylindrical coordinates as follows:

$$\left(\frac{\partial^2}{\partial r^2} + \frac{1}{r}\frac{\partial}{\partial r} - \frac{1}{r^2} + \frac{\partial^2}{\partial z^2}\right)A(r,z) = -\mu_0 J_\theta \quad (z \le 0), \tag{5.9}$$

$$\left(\frac{\partial^2}{\partial r^2} + \frac{1}{r}\frac{\partial}{\partial r} - \frac{1}{r^2} + \frac{\partial^2}{\partial z^2} - \frac{1}{\ell^2}\right)A(r,z) = 0 \quad (0 \le z \le d), \tag{5.10}$$

$$\left(\frac{\partial^2}{\partial r^2} + \frac{1}{r}\frac{\partial}{\partial r} - \frac{1}{r^2} + \frac{\partial^2}{\partial z^2}\right)A(r,z) = 0 \quad (d \le z). \tag{5.11}$$

Furthermore, by using equation (4.25) introduced in the section of Hankel transformation, the Maxwells' equations are reduced to ordinary differential equations for $\tilde{A}(k,z)$ in the Hankel transformed space, which can be solved analytically in each region [33]:

$$\left(\frac{\partial^2}{\partial z^2} - k^2\right)\tilde{A}(k,z) = 0 \quad (z \le 0), \tag{5.12}$$

$$\left(\frac{\partial^2}{\partial z^2} - \beta^2\right)\tilde{A}(k,z) = 0 \quad (0 \le z \le d), \tag{5.13}$$

$$\left(\frac{\partial^2}{\partial z^2} - k^2\right)\tilde{A}(k,z) = 0 \quad (d \le z). \tag{5.14}$$

where we assumed $J_\theta = 0$ in the above expression, and β is defined as $\beta \equiv \lambda^{-1}\sqrt{1+s^2\lambda^2}$. Solving the above equations will give us homogeneous solutions of equations(5.9), (5.10), and (5.11). The integral solution of the vector potential $A_\theta(r,z)$ is also provided based on Green's function formalism, which explicitly describes the contribution from the source current density $J_\theta(r',z')$ distributed in the coil. One must realize that this solution is not the solution which encodes the presence of the superconductor. Because Green's function formalism assumes that vector potential will vanish at the infinity, and in other places it is free to propagate. So in this sense we can call this solution the "free solution" of the Maxwell's equations in cylindrical coordinate system. The expression of $A_\theta(r,z)$ in cylindrical coordinate system is given by:

$$A_\theta(r,z) = \frac{\mu_0}{4\pi}\iiint \frac{r' J_\theta(r',z')\cos\phi}{\left[r^2+r'^2+(z-z')^2-2rr'\cos\phi\right]^{1/2}}\,d\phi\,dr'\,dz' \tag{5.15}$$

where $\phi \equiv \theta - \theta'$. In the following calculation, we will replace the integration over θ with the integral representation of special functions. From a deeper logical perspective, the reason why we can perform the above replacement in the integral lies in the fact that, for an axis-symmetric problem, the solution should not contain any dependence on the polar angle θ. Furthermore, the Legendre equation corresponds to the solution of an axis-symmetric system, while the associated Legendre function corresponds to the solution of a spherically symmetric system. If we recall the solutions of the Schrödinger equation for the hydrogen atom, the angular part of the wave function can be expressed in terms of the associated Legendre functions [31], where the two indices l and m correspond to the angular momentum quantum number and the magnetic quantum number, respectively. The situation here is analogous: the Legendre function is used to represent the solution of an axis-symmetric problem. In general, one should try to find an integral representation of the Legendre function for the solutions of axis-symmetric solutions. And the attempt made here turns out to be successful. In our case, the integration over the azimuthal angle ϕ appears naturally when calculating the vector potential in an axis-symmetric system. The integrand has the form:

$$\int \frac{\cos\phi\,d\phi}{\left[r^2+r'^2+(z-z')^2-2rr'\cos\phi\right]^{1/2}}. \tag{5.16}$$

where the integration is from 0 to π. By comparing this expression with equation (4.16), we can identify that the denominator has the same structure as in $Q_v(z)$, if we make the following substitution:

$$z = \frac{r^2+r'^2+(z-z')^2}{2rr'}. \tag{5.17}$$

This substitution corresponds to the standard variable transformation in the addition theorem of Legendre functions. Since we are dealing with the case $v = 1/2$, the corresponding $Q_{1/2}(z)$ has an explicit integral representation, which matches exactly with the angular integral over ϕ in equation (5.15). Therefore, equation (5.18) follows directly from applying the integral representation of $Q_{1/2}(z)$ to the ϕ integration, with an additional factor $1/\sqrt{rr'}$ coming from the normalization of the integral:

$$\int \frac{\cos\phi\, d\phi}{[r^2 + r'^2 + (z-z')^2 - 2rr'\cos\phi]^{1/2}} = \frac{1}{\sqrt{rr'}} Q_{1/2}\left(\frac{r^2 + r'^2 + (z-z')^2}{2rr'}\right). \tag{5.18}$$

Next we should verify that: The solution calculated by the Green's function approach and the Hankel transformation approach is identical. To verify this, we need to use equation(4.23) in the section of integral representation of Bessel function. The reason for applying equation(4.23) is straight forward, because the integrand of Hankel transformation contains Bessel function. So naturally we would like to express Legendre function in terms of the integral of Bessel function. If we chose $\nu = 1$, $a = |z - z'|$, $b = r$, and $c = r'$ in equation(4.23), it yields:

$$\int_0^\infty e^{-s|z-z'|} J_1(rs) J_1(r's)\, ds = \frac{1}{\pi\sqrt{rr'}} Q_{1/2}\left(\frac{(z-z')^2 + r'^2 + r^2}{2rr'}\right). \tag{5.19}$$

where $a = |z - z'| \geq 0$ and this ensures that the integral does not diverge. Put the above formula back to the vector potential we obtained:

$$A_\theta(r,z) = \frac{\mu_0}{2} \iiint r' J_\theta(r',z') e^{-s|z-z'|} J_1(sr) J_1(sr')\, ds\, dr'\, dz' \tag{5.20}$$

where J_θ is the current source in the θ direction. $J_1(sr)$ is the first order Bessel function. Using this formula we can calculate the vector potential A_θ created by any source $\vec{J}$ which only has nonzero component in θ direction. Moreover, from equation(5.20), we can derive a 2-D Green's function:

$$G(r,r',z,z') = \frac{\mu_0}{2} \int r' e^{-s|z-z'|} J_1(sr) J_1(sr')\, ds \tag{5.21}$$

Then equation (5.20) can be calculated by integrating the Green's function together with the source. This will serve as an inhomogeneous solution of the Maxwell equation in region $z \leq 0$. Then we can compare it with the result derived from solving equation(5.12). The comparison will be done in the following section.

This theoretical formulation lays the foundation for calculating the analytical expression of the vector potential created by the coil-superconductor system in the subsequent sections.

5.2 The Pancake Coil Revisit

To show that the calculation in this research can give the same result in previous research [17] [32], we consider a typical configuration of a pancake coil for the purpose of inductance measurement and penetration depth analysis in superconducting samples. As shown in Figure 5.1, the coil system consists of two identical pancake coils symmetrically placed with respect to the center axis with a minimum radius R. It is composed of M turns in the radial direction and L layers in the z axis direction. The radial spacing between adjacent turns is denoted by ΔR, and the axial spacing between adjacent layers is denoted by ΔL. The coil is placed below the superconducting sample at a distance $-h$.

This configuration provides an effective model to analyze the coupling between the coil-generated magnetic field and the sample's electromagnetic response. In particular, the cylindrical symmetry of the pancake coil allows for the simplification of the vector potential and magnetic field calculation using Hankel transforms or integral with Bessel functions derived in the last section.

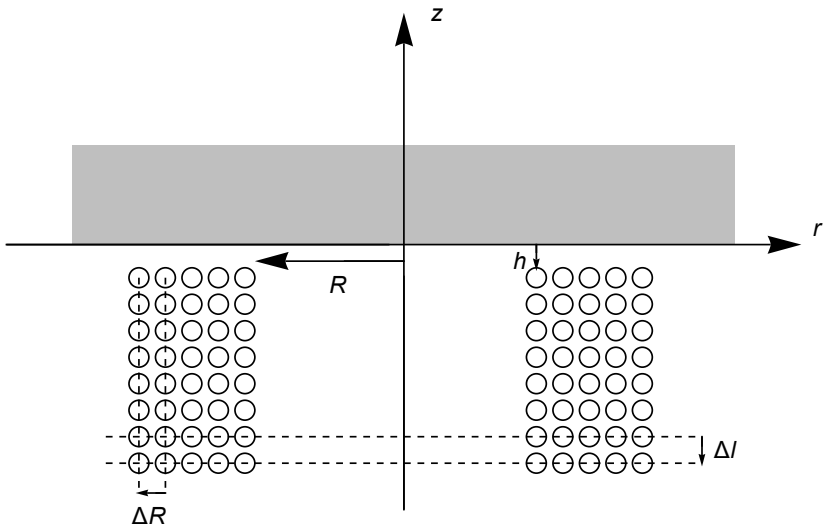

Figure 5.1: Cross-sectional view of the pancake coil together with the sample block.

Since the pancake coil model satisfies the condition of axial symmetry, we can start from equation (5.21) to derive the two-dimensional Green's function. This Green's function will then be used to obtain the particular solution of the second-order inhomogeneous differential equation. At region $z < 0$, the current of the pancake coil is given by:

$$J_\theta(r,z) = I \sum_{l=0}^{L-1} \delta(z+h+l\Delta h) \sum_{m=0}^{M-1} \delta(r-R-m\Delta R) \tag{5.22}$$

By integrating the two dimensional Green's function multiplied by the source term (the current) with respect to the variable s, we obtain:

$$A_\theta(r,z) = \frac{\mu_0 I}{2} \sum_{l=0}^{L-1} \sum_{m=0}^{M-1} r_m \int e^{-s|z+h+l\Delta h|} J_1(sr) J_1(sr_m)\, ds \tag{5.23}$$

where r_m is defined as:

$$r_m \equiv R + m\Delta R \tag{5.24}$$

From the definition of inverse Hankel transformation, we have:

$$A_\theta(r,z) = \int_0^\infty s J_\nu(sr) \tilde{A}(s)\, ds \tag{5.25}$$

By comparing equation (5.23) and (5.25)(when ν=1), we have:

$$\tilde{A}_\theta(s,z) = \frac{\mu_0 I}{2} \sum_{l=0}^{L-1} \sum_{m=0}^{M-1} r_m J_1(sr_m) \frac{1}{s} e^{-s|z+h+l\Delta h|} \tag{5.26}$$

Equation (5.26) is a particular solution of the inhomogeneous differential equation in region $z < 0$. The homogeneous solution can be calculated by using equation (5.12) $\sim$ (5.14) in the previous section. The general solution is the homogeneous term adding the inhomogeneous term:

$$\tilde{g}(s,z) \equiv \frac{\mu_0 I}{2} \sum_{l=0}^{L-1} \sum_{m=0}^{M-1} r_m J_1(s r_m) \frac{1}{s} e^{-s|z+h+l\Delta h|} \tag{5.27}$$

$$\tilde{A}(s,z) = \tilde{g}(s,z) + C_1(s) e^{sz}, \quad (z \leq 0) \tag{5.28}$$

where we defined the Hankel transformation of the inhomogeneous solution as $\tilde{g}(s,z)$ for simplification. The vector potential at region $0 \leq z \leq d$ and $d \leq z$ only possess the homogeneous terms:

$$\tilde{A}(s,z) = C_2(s) e^{-\beta z} + C_3(s) e^{\beta z}, \quad (0 \leq z \leq d) \tag{5.29}$$

$$\tilde{A}(s,z) = C_4(s) e^{-s(z-d)}, \quad (d \leq z) \tag{5.30}$$

where λ is the penetration depth of the superconducting materials used in the experiment. The information of the superconductor was encoded in the parameter β, defined as $\beta = \frac{1}{\lambda}(1 + s^2\lambda^2)^{\frac{1}{2}}$. At this point, we can impose the boundary conditions to this solutions, and they are completely solvable. To determine the coefficients $C_1(s)$ through $C_4(s)$ in the general solution for the vector potential, we apply the boundary conditions across the interfaces between different regions. These boundary conditions arise from the continuity of the magnetic field components, which are governed by Maxwell's equations. The radial component of the magnetic field $B_r(r,z)$ is related to the vector potential $A(r,z)$ through:

$$B_r(r,z) = -\frac{\partial A_\theta(r,z)}{\partial z} = \int_0^\infty ds\, s J_1(sr) \left(-\frac{\partial \tilde{A}_\theta(s,z)}{\partial z} \right) \tag{5.31}$$

which follows directly from the definition $\vec{B} = \nabla \times \vec{A}$ in cylindrical coordinates under the assumption of azimuthal symmetry. where $\tilde{A}(s,z)$ denotes the Hankel-transformed vector potential. Imposing the boundary condition $H_{r1} - H_{r2} = B_{r1}/\mu_1 - B_{r2}/\mu_2 = 0$ at $z = 0$ and $z = d$ lead to the following equations:

$$\frac{\mu_0 I}{2} \sum_m (-1)^m r_m J_1(s r_m) \frac{1}{s} e^{-sh} - C_1 = \frac{\beta}{s}(C_2 - C_3), \tag{5.32}$$

$$C_2 e^{-\beta d} - C_3 e^{\beta d} = \frac{s}{\beta} C_4 \tag{5.33}$$

where we assumed that $\mu_1 = \mu_2$. In the following chapter, our simulation software will also use this condition. These two equations form part of the four boundary conditions required to determine the coefficients. The remaining two conditions arise from the continuity of the perpendicular component of the magnetic field B_z at $z = 0$ and $z = d$, which can be calculated by the following formula:

$$B_z(r,z) = \frac{1}{r}\left(A_\theta + r\frac{\partial A_\theta}{\partial r} \right) = \int_0^\infty ds\, s \left(\frac{J_1(sr)}{r} + s J_1(sr) \right) \tilde{A}(s,z), \tag{5.34}$$

Imposing the boundary condition $B_{z1} - B_{z2} = 0$ at $z = 0$ and $z = d$ will give us the following equations:

$$\frac{\mu_0 I}{2} \sum_m (-1)^m r_m J_1(s r_m) \frac{1}{s} e^{-sh} + C_1 = C_2 + C_3, \tag{5.35}$$

$$C_2 e^{-\beta d} + C_3 e^{\beta d} = C_4, \tag{5.36}$$

By solving these four equations, the coefficients $C_1(s)$ to $C_4(s)$ can be uniquely determined, which enables the construction of the complete solution for the vector potential in each region:

$$C_1 = \frac{(-1 + e^{2\beta d})(s - \beta)(s + \beta)\, \tilde{g}(s, 0)}{(-1 + e^{2\beta d})\, s^2 + 2\,(1 + e^{2\beta d})\, s\beta + (-1 + e^{2\beta d})\, \beta^2} \tag{5.37}$$

$$C_2 = \frac{2 e^{2\beta d}\, s\, (s + \beta)\, \tilde{g}(s, 0)}{(-1 + e^{2\beta d})\, s^2 + 2\,(1 + e^{2\beta d})\, s\beta + (-1 + e^{2\beta d})\, \beta^2} \tag{5.38}$$

$$C_3 = \frac{2\, s\, (s - \beta)\, \tilde{g}(s, d)}{(-1 + e^{2\beta d})\, s^2 + 2\,(1 + e^{2\beta d})\, s\beta + (-1 + e^{2\beta d})\, \beta^2} \tag{5.39}$$

$$C_4 = \frac{4\, e^{\beta d}\, s\, \beta\, \tilde{g}(s, d)}{(-1 + e^{2\beta d})\, s^2 + 2\,(1 + e^{2\beta d})\, s\beta + (-1 + e^{2\beta d})\, \beta^2} \tag{5.40}$$

After obtain the solution of vector potential in different regions. We are ready to calculate the impedance and the inductance of the circuit now. The integration along the coil are given by:

$$\int_{\text{coil}} dl \quad \rightarrow \quad \sum_m \sum_l \int dr \times\, r\delta(r - r_m) \int d\theta \int dz\, \delta(z + h + l\Delta h) \tag{5.41}$$

Hence, we find:

$$Z(\beta) = i\pi\omega\mu_0 \int \mathcal{N}(s) ds + i\pi\omega\mu_0 \int_0^\infty ds\, \frac{\left(\frac{s}{\beta} - \frac{\beta}{s}\right)}{2\coth(\beta d) + \left(\frac{s}{\beta} + \frac{\beta}{s}\right)}\, \mathcal{M}(s) \tag{5.42}$$

$$\mathcal{M}(s) = \left\{ e^{-hs} \sum_{l=0}^{L-1} e^{-l\Delta h s} \sum_{m=0}^{M-1} J_1(s r_m)\, r_m \right\}^2 \tag{5.43}$$

$$\mathcal{N}(s) = \left\{ \sum_m (-1)^m r_m J_1(s r_m) \right\}^2 \tag{5.44}$$

The change of the inductance L due to the variation of penetration depth λ can be calculated by using $\Delta Z_\omega \simeq i\omega\Delta L$. Hence we have:

$$L(\beta) = L_0 + \pi\mu_0 \int_0^\infty \frac{\left\{e^{-hs}\sum_{l=0}^{L-1} e^{-l\Delta hs}\sum_{m=0}^{M-1} J_1(sr_m)\times r_m\right\}^2}{1+2s\lambda\coth(\beta d)}\,ds$$
$$= L_0 + \pi\mu_0 \int_0^\infty ds\,\frac{\left(\frac{s}{\beta}-\frac{\beta}{s}\right)}{2\coth(\beta d)+\left(\frac{s}{\beta}+\frac{\beta}{s}\right)}\,\mathcal{M}(s) \tag{5.45}$$

here, L_0 denotes the inductance of the coil at the room temperature, which can be measured in the experiment.

When the sample is a superconductor, λ represents the penetration depth, typically ranging from approximately 100 nm to 1000 nm. The expression of $\mathcal{M}(s)$ includes the exponential factor e^{-2hs}, which decays rapidly when $s \gg (2h)^{-1} \sim 10^4$. Therefore, the integral can be cut-off around $s \sim 10^6$. In this regime, since $s\lambda < 10^{-2}$, we may approximate $\beta \sim \frac{1}{\lambda}$, leading to $\frac{s}{\beta}-\frac{\beta}{s} = -\frac{1}{s\lambda}$, $\quad \frac{s}{\beta}+\frac{\beta}{s} = \frac{1}{s\lambda}$. Under this approximation, equations (5.42) and (5.45) can be simplified as follows:

$$Z(\lambda) = i\pi\omega\mu_0 \int \mathcal{N}(s)ds - i\pi\omega\mu_0 \int_0^\infty \frac{\mathcal{M}(s)}{1+2s\lambda\coth\left(\frac{d}{\lambda}\right)}\,ds \tag{5.46}$$

$$L(\lambda) = L_0 - \pi\mu_0 \int_0^\infty \frac{\mathcal{M}(s)}{1+2s\lambda\coth(\frac{d}{\lambda})}\,ds \tag{5.47}$$

Using the above equations, we can evaluate the change in impedance and inductance of the coil induced by temperature variations—that is, by changes in the London penetration depth.

5.3 An Axial-Symmetric Approximation Model of The Spiral Coil

A spiral coil is a type of coil in which a wire is wound in a spiral or helical pattern. Unlike conventional spiral coils, the wire line of the spiral coil used in this thesis goes from a single continuous line, and the line that reaches the center from the outer periphery passes through the gaps between the inward-going line and returns to the outer periphery in the opposite direction. As a result, the current flowing through adjacent wires flows in opposite directions, generating a magnetic field only near the coil and reducing the magnetic flux reaching distant areas. This makes the coil highly sensitive to changes in the magnetic field distribution near the coil.

An axial symmetry approximation model means that we replace the spiral shape of the coil by a set of circle coils, so we can use the general theory of axial symmetric coil to calculate this model.

We adopt the following experiment configuration: The coil was placed below the superconductor with distance h, the distance between the adjacent turn was given by ΔR. The thickness of sample was given by d. In this case we only consider one layer in z direction. We will solve this case in the cylindrical coordinate as well. The current

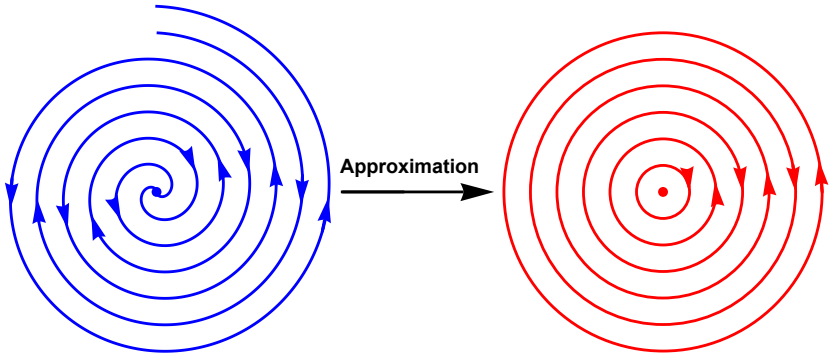

Figure 5.2: Schematic diagram of the approximation process for spiral coil [34]. The arrows denote the direction of the currents.

distribution in this case can be described by an additional $(-1)^m$ factor to indicate the inverse direction of the current in adjacent turn:

$$J_\theta(r,z) = I\delta(z+h)\sum_m (-1)^m \delta(r-r_m) \tag{5.48}$$

In this case we can still use the Green's function in equation(5.21), and multiply it with the source current and integrate it over the variable s to give the inhomogeneous solution in region $z<0$:

$$A_\theta = \frac{\mu_0 I}{2}\sum_m (-1)^m r_m \int e^{-s|z+h|} J_1(sr) J_1(sr_m)\, ds \tag{5.49}$$

The solution in the Hankel-transformed space can be obtained from the inverse Hankel transformation as follows:

$$A_\theta(r,z) = \int_0^\infty s J_\nu(sr)\tilde{A}(s,z)\, ds \tag{5.50}$$

$$\tilde{A}_\theta(s,z) = \frac{\mu_0 I}{2}\sum_{m=0}^{M-1}(-1)^m r_m J_1(sr_m)\frac{1}{s}e^{-s|z+h|} \tag{5.51}$$

In both here and the previous section, the above solution was not derived using the Hankel transformation but the Green's function. In this section, we apply the Hankel transformation at region $z<0$ and derive the solution again, aiming to compare the results from two different approaches and thereby enhance the reliability of the solution. With the similar way to obtain (5.12), the equation at region $z<0$ are given by:

$$\left(\frac{\partial^2}{\partial z^2} - s^2\right)\tilde{A}_\theta(s,z) = -\mu_0 I\delta(z+h)\sum_m (-1)^m r_m J_1(sr_m). \tag{5.52}$$

Take the Fourier transformation on both side of the above equation, the delta function on the right-hand side will become an exponent in the Fourier space, which yields the solution of $\tilde{A}_\theta(s,z)$ in Fourier space:

$$\tilde{A}_F(s,q) = \mu_0 I \sum_m (-1)^m \frac{r_m J_1(s r_m)}{q^2+s^2} e^{-iqh} \tag{5.53}$$

Then by taking the inverse Fourier transformation of $\tilde{A}_F(s,q)$, we derived the solution of equation (5.52):

$$\begin{aligned}\tilde{A}_\theta(s,z) &= \int_{-\infty}^{\infty} \tilde{A}_F(s,q) e^{iqz}\, dq. \\ &= \frac{\mu_0 I}{2} \sum_{m=0}^{M-1} (-1)^m r_m J_1(s r_m) \frac{1}{s} e^{-s|z+h|}\end{aligned} \tag{5.54}$$

Comparing equation (5.54) and equation (5.51), we find that they match exactly the same with each other. Below, we will denote this result as f to avoid confusion with the special solution in pancake coil case:

$$\tilde{f}(s,z) \equiv \frac{\mu_0 I}{2} \sum_{m=0}^{M-1} (-1)^m r_m J_1(s r_m) \frac{1}{s} e^{-s|z+h|} \tag{5.55}$$

The general solution can be obtained by adding the homogeneous terms in the region $z < 0$, while in the other regions we only have the homogeneous terms:

$$\tilde{A}(s,z) = \tilde{f}(s,z) + C_1(s) e^{sz}, \quad (z \le 0) \tag{5.56}$$

$$\tilde{A}(s,z) = C_2(s) e^{-\beta z} + C_3(s) e^{\beta z}, \quad (0 \le z \le d) \tag{5.57}$$

$$\tilde{A}(s,z) = C_4(s) e^{-s(z-d)}, \quad (d \le z) \tag{5.58}$$

$$\beta \equiv \lambda^{-1} \sqrt{1 + s^2 \lambda^2} \tag{5.59}$$

Similarly, in the case of the pancake coil, the four coefficients C1 to C4 are determined by the continuity conditions of all components of the magnetic field at each boundary. Here we only need to substitute all the $\tilde{g}(s,0)$ into $\tilde{f}(s,z)$ in equations (5.37) $\sim$ (5.40) to get the boundary coefficients in spiral coil case:

$$C_1 = \frac{(-1+e^{2\beta d})(s-\beta)(s+\beta)\,\tilde{f}(s,0)}{(-1+e^{2\beta d})\,s^2 + 2\,(1+e^{2\beta d})\,s\beta + (-1+e^{2\beta d})\,\beta^2} \tag{5.60}$$

$$C_2 = \frac{2e^{2\beta d}\,s\,(s+\beta)\,\tilde{f}(s,0)}{(-1+e^{2\beta d})\,s^2 + 2\,(1+e^{2\beta d})\,s\beta + (-1+e^{2\beta d})\,\beta^2} \tag{5.61}$$

$$C_3 = \frac{2\,s\,(s-\beta)\,\tilde{f}(s,d)}{(-1+e^{2\beta d})\,s^2 + 2\,(1+e^{2\beta d})\,s\beta + (-1+e^{2\beta d})\,\beta^2} \tag{5.62}$$

$$C_4 = \frac{4\,e^{\beta d}\,s\,\beta\,\tilde{f}(s,d)}{(-1+e^{2\beta d})\,s^2 + 2\,(1+e^{2\beta d})\,s\beta + (-1+e^{2\beta d})\,\beta^2} \tag{5.63}$$

The impedance and the inductance of the circuit can be calculated respectively by integrating along the coil at region $z \leq 0$. The integration along the coil takes the form:

$$\int_{\text{coil}} dl \quad \rightarrow \quad \sum_m \int dr \times r(-1)^m \delta(r - r_m) \int d\theta \int dz\, \delta(z + h) \tag{5.64}$$

After the integration, we can obtain the expression of impedance and inductance as follows:

$$\begin{aligned} Z &= \frac{i\omega}{I} \sum_m 2\pi r_m (-1)^{m+1} \int_0^\infty ds\, s J_1(s r_m) \tilde{A}(s, -h) \\ &= Z_0 - i\pi\omega\mu_0 \int_0^\infty \frac{\mathcal{L}(s)}{1 + 2s\lambda \coth\left(\frac{d}{\lambda}\right)} ds \end{aligned} \tag{5.65}$$

$$\mathcal{L}(s) = \left\{ e^{-sh} \sum_{m=0}^{M-1} (-1)^m J_1(s r_m) \times r_m \right\}^2 \tag{5.66}$$

$$\begin{aligned} L &= \frac{1}{I} \sum_m 2\pi r_m (-1)^m \int_0^\infty ds\, s J_1(s r_m) \tilde{A}(s, -h) \\ &= L_0 - \pi\mu_0 \int_0^\infty \frac{\mathcal{L}(s)}{1 + 2s\lambda \coth\left(\frac{d}{\lambda}\right)} ds \end{aligned} \tag{5.67}$$

The important part is the inductance effect from the sample, which we will denote it as Z_{s} and L_{s} respectively:

$$Z_{\text{s}} = -i\pi\omega\mu_0 \int_0^\infty \frac{\mathcal{L}(s)}{1 + 2s\lambda \coth\left(\frac{d}{\lambda}\right)} ds \tag{5.68}$$

$$L_{\text{s}} = -\pi\mu_0 \int_0^\infty \frac{\mathcal{L}(s)}{1 + 2s\lambda \coth\left(\frac{d}{\lambda}\right)} ds \tag{5.69}$$

The variation of the penetration depth will change the value of the above two equations. The variation of the inductance will cause the variation of the resonant frequency. Then by reading the variation of the resonant frequency of the circuit from experiment device, we can transform the raw data of frequency into the penetration depth of the superconductor at different temperatures. And finally we will get the penetration depth as a function of temperature, which enables us to compare it with the result from BCS theory.

5.4 Axial-Asymmetry Model: The Archimedean Spiral Coil

An Archimedean spiral coil is a type of planar spiral coil where the radius of each loop increases linearly with the angle as the coil spirals outward from the center(as shown in

Figure 5.3). The parametrization of a spiral shape in two dimensional polar coordinate is defined as:

$$r(\theta) = a + b\theta \tag{5.70}$$

where $r(\theta)$ represents the radial distance from the center as a function of the polar angle θ, where a is the initial radius (offset from the center), and b is the spacing constant that determines how tightly the spiral is wound, and θ is the polar angle. In order to solve Maxwell's equations in the presence of a spiral coil, we first define the current of the spiral coil. We place the coil at a two dimensional plane $z = -h$ located below the superconductor. Since the spiral coil does not possess the axial symmetry along z axis, the current will be a vector with two non-zero components. Again we use delta function to give the current a spiral shape:

$$J_\theta(r,\theta,z) = I\delta(z+h)\sum_{n=0}^{m}\delta\left(r - a - \frac{\Delta R}{\pi}(\theta + 2n\pi)\right)\cos\alpha \tag{5.71}$$

$$J_r(r,\theta,z) = I\delta(z+h)\sum_{n=0}^{m}\delta\left(r - a - \frac{\Delta R}{\pi}(\theta + 2n\pi)\right)\sin\alpha \tag{5.72}$$

$$\tan\alpha = \frac{dr_m}{r_m d\theta}, \quad r_m(\theta) = a + \frac{\Delta R}{\pi}(\theta + 2m\pi), \quad dr_m = \frac{\Delta R}{\pi}d\theta \tag{5.73}$$

where ΔR is the radial spacing between adjacent turns, and a is the initial length of the radius. α is the angel between the direction along the spiral coil and the direction of θ axis in polar coordinate. Another red solid line along the r direction is perpendicular to the red solid line along θ direction.

Followed by the above definition, the $\sin\alpha$, $\cos\alpha$ and $\tan\alpha$ can be calculated as:

$$\tan\alpha = \frac{\frac{\Delta R}{\pi}d\theta}{r_m \cdot d\theta} = \frac{\Delta R}{\pi r_m(\theta)}, \quad \cos\alpha = \left(\frac{1}{1+\tan^2\alpha}\right)^{\frac{1}{2}}, \quad \sin\alpha = \left(\frac{\tan^2\alpha}{1+\tan^2\alpha}\right)^{\frac{1}{2}} \tag{5.74}$$

Followed by equations (5.71) and (5.72), we can immediately tell that the vector potential $\vec{A}(\vec{r})$ will have two non-zero components A_r, A_θ. This is different from the axis-symmetric case, where we only have one non-zero component. If we adopt the Coulomb gauge condition ($\nabla \cdot \vec{A} = 0$) and assume that $A_z = 0$, then by evaluating the expression $\nabla \times (\nabla \times \vec{A})$, we obtain:

$$\begin{aligned}\nabla \times (\nabla \times \vec{A}) = \frac{1}{r}\Bigg\{ & \left[\frac{1}{r}\frac{\partial}{\partial\theta}\left(\frac{\partial(rA_\theta)}{\partial r} - \frac{\partial A_r}{\partial\theta}\right) - \frac{\partial^2 A_r}{\partial z^2}\right]\hat{r} \\ & + \left[-r\frac{\partial^2 A_\theta}{\partial z^2} - \frac{\partial}{\partial r}\left(\frac{1}{r}\left(\frac{\partial(rA_\theta)}{\partial r} - \frac{\partial A_r}{\partial\theta}\right)\right)\right]\hat{\theta} \\ & + \left[\frac{\partial^2 A_r}{\partial r\partial z} + \frac{\partial^2 A_\theta}{\partial\theta\partial z}\right]\hat{z}\Bigg\}\end{aligned}$$

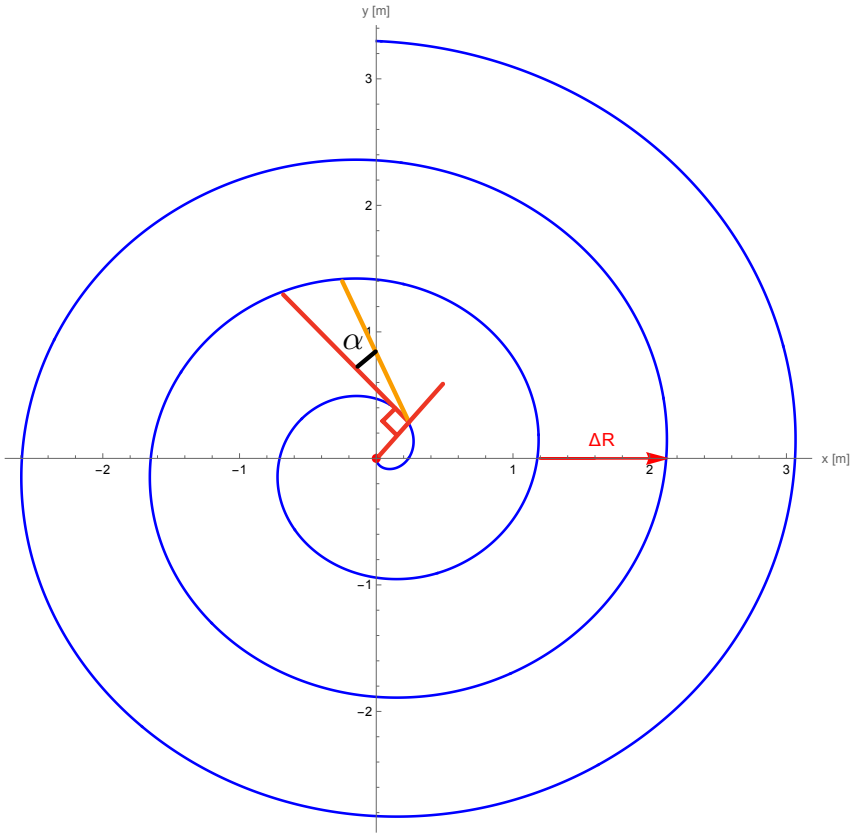

Figure 5.3: The Archimedean spiral when a = 0. The orange line represents the tangent to the spiral curve, while the two red lines are perpendicular to each other, pointing in the radial (r) and angular (θ) directions of the polar coordinate, respectively.

Although the axial symmetry is broken in this case, the magnetic vector potential $\vec{A}$ created by the supercurrent still obeys London's equations in the low magnetic field limit. Therefore, we can still use the following relation to describe the induced screening current on the surface of the sample:

$$\begin{aligned}\vec{J}_{\theta s} &= -\frac{1}{\mu_0 \ell^2} A_\theta(r,z)\,\hat{\theta} \\ \vec{J}_{rs} &= -\frac{1}{\mu_0 \ell^2} A_r(r,z)\,\hat{r}\end{aligned} \tag{5.75}$$

The Maxwell's equations in three different regions and two different components of magnetic vector potential are given by:

$$\begin{aligned}&\frac{1}{r^2}\frac{\partial}{\partial\theta}\left(\frac{\partial A_r}{\partial\theta} - \frac{\partial(rA_\theta)}{\partial r}\right) + \frac{1}{r}\frac{\partial^2 A_r}{\partial z^2} \\ &\quad = -\mu_0 I \delta(z+h) \sum_{n=0}^{m} \delta\left(r - a - \frac{\Delta R}{\pi}(\theta + 2n\pi)\right) \sin\alpha\,, \quad (z \le 0)\end{aligned} \tag{5.76}$$

$$\frac{1}{r}\frac{\partial}{\partial\theta}\left(\frac{\partial A_r}{\partial\theta} - \frac{\partial(rA_\theta)}{\partial r}\right) + \frac{\partial^2 A_r}{\partial z^2} - \frac{1}{\ell^2} A_r = 0\,, \qquad (0 \le z \le d) \tag{5.77}$$

$$\frac{1}{r^2}\frac{\partial}{\partial\theta}\left(\frac{\partial A_r}{\partial\theta} - \frac{\partial(rA_\theta)}{\partial r}\right) + \frac{1}{r}\frac{\partial^2 A_r}{\partial z^2} = 0\,, \qquad (d \le z) \tag{5.78}$$

$$\begin{aligned}&\frac{\partial^2 A_\theta}{\partial z^2} + \frac{\partial}{\partial r}\left(\frac{1}{r}\frac{\partial(rA_\theta)}{\partial r} - \frac{1}{r}\frac{\partial A_r}{\partial\theta}\right) \\ &\quad = -\mu_0 I \delta(z+h) \sum_{n=0}^{m} \delta\left(r - a - \frac{\Delta R}{\pi}(\theta + 2n\pi)\right) \cos\alpha\,, \quad (z \le 0)\end{aligned} \tag{5.79}$$

$$\frac{\partial^2 A_\theta}{\partial z^2} + \frac{\partial}{\partial r}\left(\frac{1}{r}\frac{\partial(rA_\theta)}{\partial r} - \frac{1}{r}\frac{\partial A_r}{\partial\theta}\right) - \frac{1}{\ell^2} A_\theta = 0\,, \qquad (0 \le z \le d) \tag{5.80}$$

$$\frac{\partial^2 A_\theta}{\partial z^2} + \frac{\partial}{\partial r}\left(\frac{1}{r}\frac{\partial(rA_\theta)}{\partial r} - \frac{1}{r}\frac{\partial A_r}{\partial\theta}\right) = 0\,, \qquad (d \le z) \tag{5.81}$$

If we assume axial symmetry on these equations ($\partial A_\theta/\partial\theta = 0$) and that the radial component of the vector potential vanishes ($A_r = 0$), the left-hand side of these equations simplifies as (without the screening current part):

$$\frac{\partial^2 A_\theta}{\partial z^2} + \frac{\partial}{\partial r}\left(\frac{1}{r}A_\theta + \frac{\partial A_\theta}{\partial r}\right) = \frac{\partial^2 A_\theta}{\partial z^2} + \left(-\frac{1}{r^2}A_\theta + \frac{1}{r}\frac{\partial A_\theta}{\partial r} + \frac{\partial^2 A_\theta}{\partial r^2}\right) \tag{5.82}$$

This is exactly the left-hand side part of differential equation in axis-symmetric case. The solutions of these Maxwell's equations can be calculated from the general solution in equation (4.10) derived by the Green's function at different regions, respectively. Specifically, we are interested in the solutions at the region $z < 0$, where the spiral coil is present. The solutions in this region are given by:

$$A_r = \mathbf{A} \cdot \hat{\mathbf{r}}, \quad A_\theta = \mathbf{A} \cdot \hat{\theta} \tag{5.83}$$

$$A_r = \frac{\mu_0}{4\pi} \iiint \frac{1}{|\mathbf{r} - \mathbf{r}'|} \left(\mathbf{J}(\mathbf{r}', t) \cdot \hat{\mathbf{r}}\right) \, d^3\mathbf{r}' \tag{5.84}$$

$$A_\theta = \frac{\mu_0}{4\pi} \iiint \frac{1}{|\mathbf{r} - \mathbf{r}'|} \left(\mathbf{J}(\mathbf{r}', t) \cdot \hat{\theta}\right) \, d^3\mathbf{r}' \tag{5.85}$$

$$\begin{cases} \hat{\boldsymbol{\theta}} \cdot \hat{\boldsymbol{\theta}}' = \hat{\mathbf{r}}' \cdot \hat{\mathbf{r}} = \cos\theta' \cos\theta + \sin\theta' \sin\theta = \cos(\theta' - \theta), \\ \hat{\mathbf{r}} \cdot \hat{\boldsymbol{\theta}}' = -\hat{\boldsymbol{\theta}} \cdot \hat{\mathbf{r}}' = -\cos\theta \sin\theta' + \cos\theta' \sin\theta = \sin(\theta - \theta'). \end{cases} \tag{5.86}$$

After integrating with respect to r' and z', the solution of vector potential in region $z < 0$ under the boundary condition that $\vec{A}$ vanishes at infinity can be written as:

$$\begin{aligned} A_r(r, \theta, z) = \frac{\mu_0 I}{4\pi} \sum_{m=0}^{n} \int_0^{2\pi} & \left[r^2 + (r_m + b\theta')^2 + (z + h)^2 - 2r(r_m + b\theta')\cos(\theta' - \theta)\right]^{-\frac{1}{2}} \\ & \times \left[\cos(\theta' - \theta)\sin\alpha - \sin(\theta' - \theta)\cos\alpha\right](r_m + b\theta')\, d\theta' \end{aligned} \tag{5.87}$$

$$\begin{aligned} A_\theta(r, \theta, z) = \frac{\mu_0 I}{4\pi} \sum_{m=0}^{n} \int_0^{2\pi} & \left[r^2 + (r_m + b\theta')^2 + (z + h)^2 - 2r(r_m + b\theta')\cos(\theta' - \theta)\right]^{-\frac{1}{2}} \\ & \times \left[\cos(\theta' - \theta)\cos\alpha + \sin(\theta' - \theta)\sin\alpha\right](r_m + b\theta')\, d\theta' \end{aligned} \tag{5.88}$$

Equation (5.87) and (5.88) will serve as the inhomogeneous solution of the r and θ component of magnetic vector potential in region $z < 0$ respectively. It has imposed the boundary condition that $\vec{A}$ will vanish at infinity, which means the superconductor is not present in this solution. Furthermore, with the spiral shape, the vector potential $\vec{A}$ will depend on the polar angel θ, which means it no longer has an axial symmetric distribution in x-y plane. In other words, we can neither apply the Hankel transformation to the differential equations, nor express the inhomogeneous solution at $z < 0$ as a Bessel function integral representation, as we did in the axis-symmetric case. This makes the derivation of analytical expression very difficult, and the analytical result of $\vec{A}$ after imposing boundary conditions is still unsolved in this thesis. But still the "free solution" of $\vec{A}$ provides us an analytical solution of the exact spiral coil in free space, which needs further exploration.

Except its failure to give the analytical solutions with given boundary conditions in this study, it still can give us a way to calculate the inductance of the spiral coil at room temperature. To calculate the inductance of the spiral coil, we need to perform the following integration:

$$\begin{aligned} IZ &= i\omega \oint_{\text{coil}} \vec{A} \cdot d\vec{l} \\ &= i\omega \int \left[A_\theta(r(\theta), \theta)\, r\, d\theta + A_r(r, \theta(r))\, dr\right] \\ &\propto i\omega \left[\sum_i A_{r,i}\, \Delta l_r + \sum_i A_{\theta,i}\, \Delta l_\theta\right] \end{aligned} \tag{5.89}$$

Instead of directly performing the integral, it is more meaningful to consider its discretized form. This is because, in the next step, we will use COMSOL [35] simulations to calculate the vector potential generated by the spiral coil, which was performed when a superconductor with finite thickness is present. When solving electromagnetic problems, three-dimensional simulation software such as COMSOL typically outputs the vector potential in discretized form. Therefore, in the last line of the equation above, we express the integral in its discretized form.

In this study, the Cartesian components of the magnetic vector potential at any point on the spiral coil can be obtained from COMSOL simulations. It is thus necessary to convert these components into their corresponding polar coordinate components using the following formulas.

$$\vec{A} = (A_x \cos\theta + A_y \sin\theta)\,\hat{r} + (-A_x \sin\theta + A_y \cos\theta)\,\hat{\theta} \tag{5.90}$$

where the radial and angular components of the magnetic vector potential can be identified by the term in front of the corresponding unit vector. The z-component of the magnetic vector potential is typically about one percent of the x- and y-components, and thus its contribution can be neglected during integration.

The space position of all the data points can be specified by the distance away from origin along the spiral coil, which can be calculated by the following formula(if we set θ_1 to zero):

$$L = \frac{b}{2}\left[\theta\sqrt{1+\theta^2} + \operatorname{arcsinh}\theta\right]\Bigg|_{\theta_1}^{\theta_2} \tag{5.91}$$

Δl_r and Δl_θ in equation (5.92) and (5.93) are defined as radial and angular components of an infinitesimal length along the spiral coil, which can be calculated from the formula established above:

$$\Delta l_\theta = \Delta l \cdot \cos\alpha = \Delta l \cdot \left(\frac{1}{1+\tan^2\alpha}\right)^{1/2} \tag{5.92}$$

$$\Delta l_r = \Delta l \cdot \sin\alpha = \Delta l \cdot \left(\frac{\tan^2\alpha}{1+\tan^2\alpha}\right)^{1/2} \tag{5.93}$$

5.5 An Effective Theory for Inductance of Spiral Coil

Since obtaining an analytical solution of magnetic vector potential in the case of a planar spiral coil placed below a superconductor bulk with finite thickness is extremely difficult, this study proposes an effective theory to approximately calculate the inductance of the spiral coil. An important observation regarding the inductance integral is that regardless of whether the coil is uniformly or non-uniformly distributed in r direction of cylindrical coordinate, the result of the inductance integral remains linear within a certain range of penetration depth. This observation can be tested by performing numerical integral in Mathematica and see the result in a very short range of penetration depth. Therefore, to account for the effect of the spiral geometry and coil cross-section, we only need two parameters to modify the axial-symmetric approximation model developed in previous section. These two parameters can be determined by fitting with the simulation

result obtained from COMSOL(See figure 5.4(a)). The effective inductance integral is given by:

$$L = a \cdot L_0 + c \cdot L_s(\lambda) \tag{5.94}$$

where a and c are parameters accounting for the effects of the coil's cross-sectional size and its spiral geometry. $L_s(\lambda)$ is defined in Equation (5.69). Although L_0 can be absorbed into the parameter a to simplify the expression, it is retained here to emphasize the physical meaning of each component, with L_0 representing the inductance of the spiral coil at room temperature. Equation (5.94) is only accurate within a very short range of London penetration depth, thus it is called an effective theory of spiral coil inductance.

Table 5.1 summarizes the result of the inductance of spiral coil at room temperature L_0 calculated from theory, simulation, and measured from experiment, where we used the axis-symmetric approximation model to calculate the theoretical value. From the table, it is evident that the value calculated using the theoretical model(when $a = 1$, and $c = 1$) shows a large discrepancy compared to both the simulation and experimentally measured values. After fitting equation (5.94) with COMSOL simulation, we can determine the value of parameter a and c. The fitted values of a and c are shown in Table 5.2. From equation (5.94) and equation (8.1) in Chapter 8 we can determine the resonant frequency as a function of London penetration depth in our measurement. The absolute value of resonant frequency will be further calibrated by experimental data point, where we made an assumption that $f(100\,\text{nm}) = f(8.903\,\text{K})$. This assumption is equivalent to saying that the London penetration depth of the measured sample is 100 nm at 8.903 K. The result of resonant frequency as a function of London penetration depth after the absolute calibration based on the above assumption is shown in Figure 5.4(b).

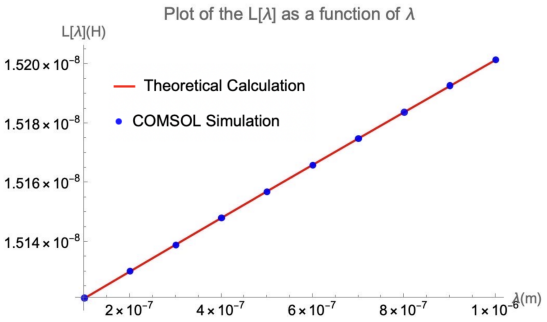

(a) The effective inductance integral fitted by COMSOL simulation result.

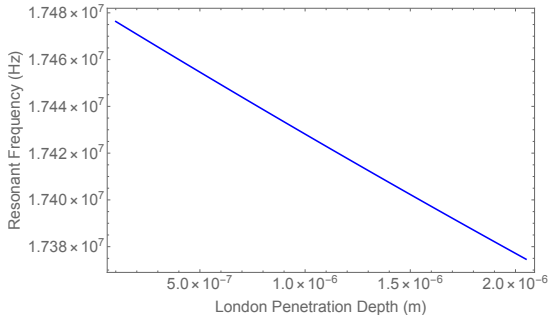

(b) The resonant frequency as a function of London penetration depth after absolute calibration.

Figure 5.4: The plot of effective inductance L and resonant frequency f as function of London penetration depth.

Table 5.1: Comparison of L_0 from different approaches

Source of result	L_0
Experiment	21.9 nH (Coil1) / 22.5 nH (Coil2)
Simulation	21.54 nH
Theory	11.70 nH

Table 5.2: Fitted parameter values

Parameter	**Fitted Value**
a	1.8442
c	0.5535

Chapter 6

Numerical Calculation in Mathematica

6.1 Introduction

Mathematica is a powerful computational software [36], which is widely used in scientific, engineering, and mathematical fields for symbolic computation, numerical calculation, data visualization, and algorithm development. It combines a high-level programming language with an extensive library of built-in functions, which enables users to perform complex mathematical operations with simple and readable code.

In this thesis, the following numerical calculations were performed within Mathematica:

1. Definite Integral of Magnetic vector potential produced by axis-symmetric coil
2. Definite Integral of Inductance of axis-symmetric coil
3. Definite Integral of Resonant frequency of resonant circuits

6.2 Parameters Setting

6.2.1 The Pancake Coil

In the pancake coil calculation, various physical and geometrical parameters were defined to model the experimental setup. The current density J_c was set to -2.0×10^{-2} A/m^2. The magnetic permeability of free space was defined as $\mu_0 = 4\pi \times 10^{-7}$ H/m. The vertical distance between the pancake coil and the superconducting film was taken as $h = -30$ μm, with the negative sign indicating that the coil is located below the film. The film thickness d was normalized to 1 for simplification, and the value of inductance at room temperature $L_0 = 7.779 \times 10^{-6}$ H was used.

To make the resonant frequency around $f = 2 \sim 4 \times 10^6$ MHz, the capacitance in circuit was chosen as $C_0 = 1 \times 10^{-9}$ F. The resistance $R = 0.2\ \Omega$ represents the resistance of the coil. The spatial coordinates of the coil turns were defined using two ranges: r specifies the radial positions of the current elements, ranging from 250 μm to 448 μm in steps of 18 μm, while l defines the vertical positions from the coil to the film surface,

ranging from $30\mu m$ to 192 μm, also in 18 μm steps. These parameters together specify the geometry, and material properties required for the numerical calculation of the vector potential and magnetic flux in the system.

6.2.2 The Spiral Coil in axis-symmetric approximation

In the spiral coil calculation, some of the parameters were adjusted to meet the future experimental conditions. The current density was set to $J_c = -50.0 \times 10^{-3}\,\mathrm{A/m^2}$, which is larger than the pancake coil case [17]. The magnetic permeability of free space have the same value as $\mu_0 = 4\pi \times 10^{-7}\,\mathrm{H/m}$. The excitation frequency was taken to be $\omega = 18 \times 10^6\,\mathrm{rad/s}$, corresponding to an resonant frequency signal in the MHz range.

The vertical separation between the coil and the superconducting film was specified as $h = 58.5\,\mu\mathrm{m}$, and the film thickness was also normalized to $d = 1$ for simplification. The base inductance of the circuit was set to $L_0 = 15.6 \times 10^{-9}\,\mathrm{H}$, and the resistance and capacitance were assigned as $R = 1.8 \times 10^{-3}\,\Omega$ and $C_0 = 10 \times 10^{-9}\,\mathrm{F}$, respectively, to satisfy the resonant frequency in the MHz range of circuit in figure 8.3.

The spacing between adjacent coil turns was defined as $b = 100\,\mu\mathrm{m}$. The radial length of the current circles was assigned using a discretized array r_m ranging from πb to $3000\,\mu\mathrm{m}$, with steps of πb, where $b = 100\mu m$ is the parameter in the parametrization equation of spiral coil.

6.3 Numerical Calculation

6.3.1 Inductance

We will use equation (5.47) to calculate the inductance of the Pancake coil. Two numerical integrations were performed using Mathematica's high-precision numerical integration function `NIntegrate`. Each numerical integral defines an inductance as a function of λ, with the integration method carefully controlled to ensure numerical stability and precision.

The first numerical integral is defined as:

$$L_s[\lambda] := -\pi\mu_0 \cdot \texttt{NIntegrate}\left[\frac{M[s]}{1 + 2s\lambda \coth\left(\frac{d}{\lambda}\right)}, \left\{s, 0, 10^6\right\}, \text{Method} \rightarrow \right.$$
$$\left.\texttt{"GlobalAdaptive"}, \text{MinRecursion} \rightarrow 3, \text{MaxRecursion} \rightarrow 6, \text{AccuracyGoal} \rightarrow 15\right] \tag{6.1}$$

This numerical integration is based on equation (5.47), which serves as an approximation of equation (5.45). Therefore, it is valid in the regime of very small λ, typically ranging from 100 nm to 1000 nm. The upper cut-off for the integration variable s is chosen as 10^6, satisfying the condition $s \gg 10^4$. Numerical results confirm that increasing the cut-off beyond 10^6 does not lead to any significant change in the value of the integral, which indicates that the chosen cut-off is sufficient for accurate evaluation.

The second numerical integral is defined as:

$$L_{ss}[\lambda] := \pi\mu_0 \cdot \texttt{NIntegrate}\left[\frac{\left(\frac{\gamma}{B[\gamma,\lambda]} - \frac{B[\gamma,\lambda]}{\gamma}\right) M[\gamma]}{\left(\frac{\gamma}{B[\gamma,\lambda]} + \frac{B[\gamma,\lambda]}{\gamma}\right) + 2\coth(B[\gamma,\lambda]\cdot d)}, \left\{\gamma, 0, 10^6\right\},\right.$$

$$\text{Method} \to \texttt{"GlobalAdaptive"}, \text{MinRecursion} \to 3, \text{MaxRecursion} \to 6,$$

$$\left.\text{AccuracyGoal} \to 15\right] \tag{6.2}$$

This numerical integration is based on equation (5.45), which involves no approximation. Therefore, it does not impose any inherent limitation on the range of validity for the integral itself. However, the entire theoretical framework used to derive the inductance as a function of the penetration depth is constructed under the assumption that the sample remains in the superconducting state or close to the superconducting state. As a result, the first numerical integral should be regarded as an effective inductance that is valid only in the low-temperature regime where London penetration depth of the sample is around 30 nm to 1000 nm.

In both cases, the use of the `"GlobalAdaptive"` method allows the integrator to dynamically allocate more sampling points in regions where the integrand changes rapidly. The settings `MinRecursion` $\to$ `3`, `MaxRecursion` $\to$ `15`, and `AccuracyGoal` $\to$ `15` were chosen to ensure both efficient calculation and precision requirement.

The resulting inductance values were plotted over a range of λ values (As shown in Figure 6.1). For the first integral $L_s[\lambda]$, the range was taken as $\lambda \in [240\,\text{nm}, 80\,\text{nm}]$, while for the second integral $L_{\text{ss}}[\lambda]$, a broader range $\lambda \in [1\,\text{mm}, 80\,\text{nm}]$ was used to see behavior at lager λ of this integral. Although the physical applicability of the second integral L_{ss} may be quite limited, it can still provide insight into the effective range of validity of the overall integral. From Figure 6.1 we can see that the inductance increases linearly as penetration depth increases, while the inductance becomes non-linear at a large region of temperature shown in Figure 6.2.

In the case of the spiral coil, an axis-symmetric approximation model has been applied. Similar to the pancake coil case, two numerical integrals have been evaluated, with the exact same definitions as in equations (5.67) and (5.69), except for the definition of $M[s]$, which differs. To examine the convergence of both integrals, we plot $M[s]$ for the pancake coil and the spiral coil, respectively.

In the case of the pancake coil, $M[s]$ exhibits a sharp initial rise (as shown in Figure 6.3), which reaches the maximum value around $s \approx 5000\,\text{m}^{-1}$. Beyond the peak, the function gradually decays and displays damped oscillation behavior. As s increases further, $M[s]$ asymptotically approaches zero, indicating that the integral converges at around $s = 2 \times 10^5\,\text{m}^{-1}$.

While in the spiral coil case, $M[s]$ exhibits a series of oscillations with increasing amplitude (as shown in Figure 6.4), leading to a dominant peak around $s \approx 9500\,\text{m}^{-1}$. The diameter of the spiral coil is approximately 2 mm, and the midpoint of the radius is

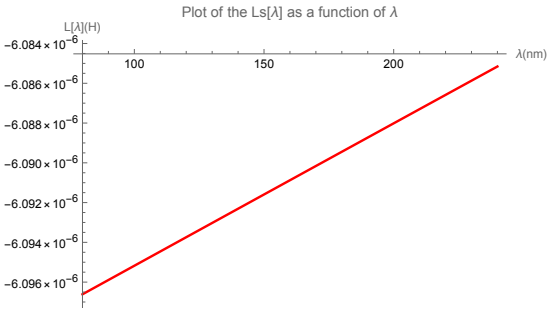

Figure 6.1: The Inductance of the pancake coil as a function of λ in the low temperature region. The plot corresponds to the numerical result of equation (6.1), which is valid only for $\lambda < 1000\,\mathrm{nm}$.

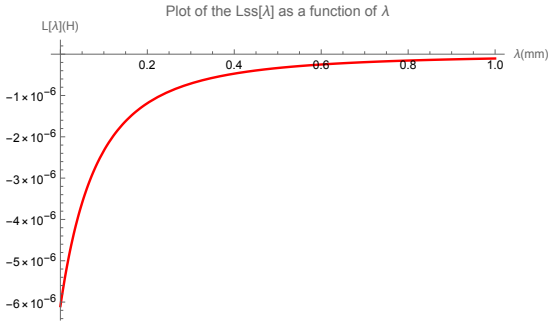

Figure 6.2: Inductance of the pancake coil as a function of the London penetration depth λ over a wider range of λ. The plot corresponds to the numerical result of equation (6.2), which remains effective when λ is large.

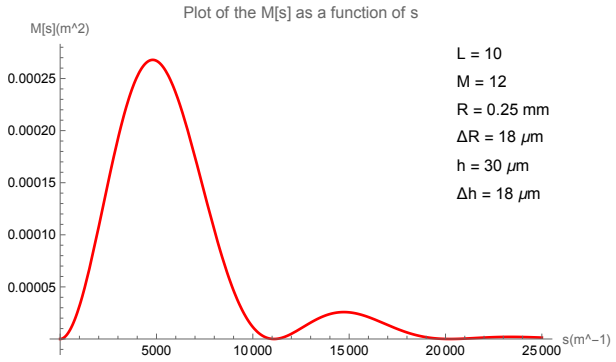

Figure 6.3: Plot of M[s] as a function of s for pancake coil, detailed geometric information are given in the figure.

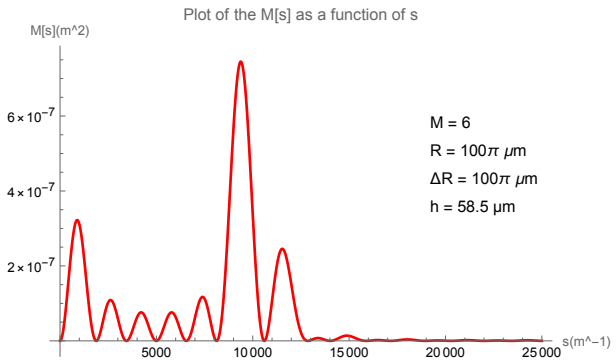

Figure 6.4: Plot of M[s] as a function of s for spiral coil, detailed geometric information are given in the figure.

around 1 mm. This corresponds to the region where the dominant peak appears in the plot, as expected. Following the peak, the function decays rapidly and displays similar damped oscillation behavior. As s increases further, $M[s]$ asymptotically approaches zero, indicating that the integral converges at around $s = 1.6 \times 10^5\,\mathrm{m}^{-1}$.

Although the behavior of $M[s]$ as a function of s differs significantly between the pancake coil and the spiral coil, the resulting inductance integrals show similar trends in both case, as shown in Figure 6.1 and Figure 6.5. It is worth noting that the magnitude of the inductance integrals differs significantly between the two cases. This is because the approximation model for the spiral coil contains significantly fewer current loops than that of the pancake coil, and the inductance integral is proportional to the integration range when the vector potential and the integration direction are the same.

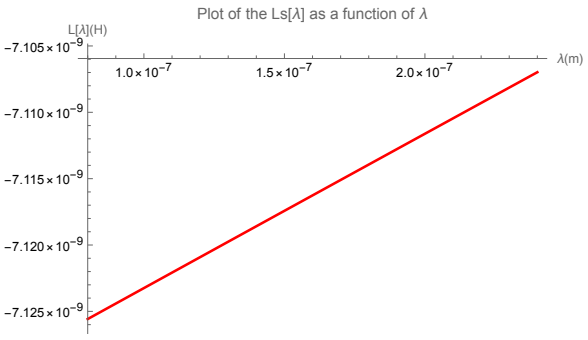

Figure 6.5: The inductance of the spiral coil as a function of λ in the low temperature region

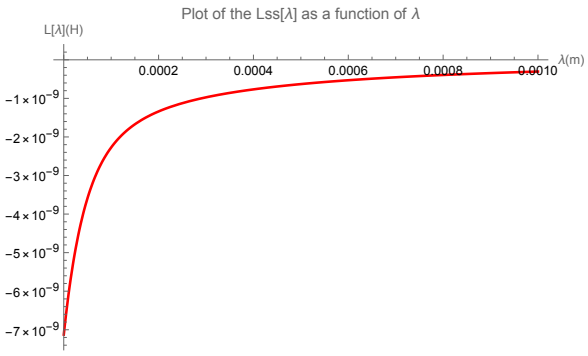

Figure 6.6: The inductance of the spiral coil as a function of λ in the full temperature region

6.3.2 Resonant Frequency

As inspired by the previous research [17], we assumed that the resonant frequency is given by the following equation :

$$f(T) = \frac{1}{2\pi}\sqrt{\frac{1}{L(T)C} - \left[\frac{R(T)}{L(T)}\right]^2} \tag{6.3}$$

This equation corresponds to the equivalent circuit shown in Figure 6.7. Note that in our measurement, we will not use the resonant circuit in Figure 6.7. The purpose of use equation (6.3) here is just to test the behavior of resonant frequency.

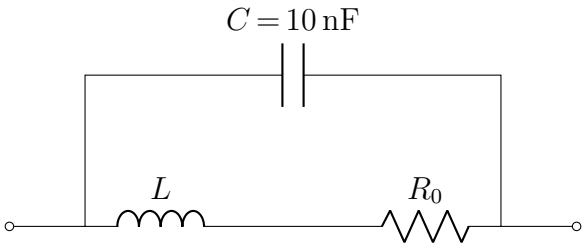

Figure 6.7: Equivalent Resonant Circuit

In the following discussion, we apply equation (6.3) to the pancake coil model. We want to verify that the resulting resonant frequency is on the order of MHz and that its variation is sufficiently large to be detected experimentally. In the case of the spiral coil model, we will instead use equation defined in chapter 8, which corresponds to the resonant circuit being used in this study.

In the case of the pancake coil, the parameters in equation (6.3) must be carefully chosen to keep the resonant frequency of the circuit within the range of 2–4 MHz. As a successful example, when $R = 0.2\,\Omega$ and $L_0 = 7.8 \times 10^{-6}\,\mathrm{H}$, the resulting resonant frequency is approximately 3.85 MHz, as shown in Figure (6.8). Figure (6.8) shows the resonant frequency as a function of the penetration depth λ. The result demonstrates a clear linear decrease in frequency with increasing λ. The above result agrees with the expected range of resonant frequency from Gauzzi's paper [17].

On the other hand, the change in the resonant frequency Δf is also of great importance from an experimental perspective. Δf can be calculated as the difference between the integral result of f with the sample and the value of f without the sample, where the latter is a constant determined by L_0. The results are plotted over a broad range of λ and within a narrower effective range corresponding to the low-temperature region, as shown in Figure 6.9 and Figure 6.10, respectively. Similarly, we can plot the inductance of spiral coil by using this method. The resonant frequency of spiral coil is not plotted here is because the equivalent circuit is different in the case of spiral which will be explained in

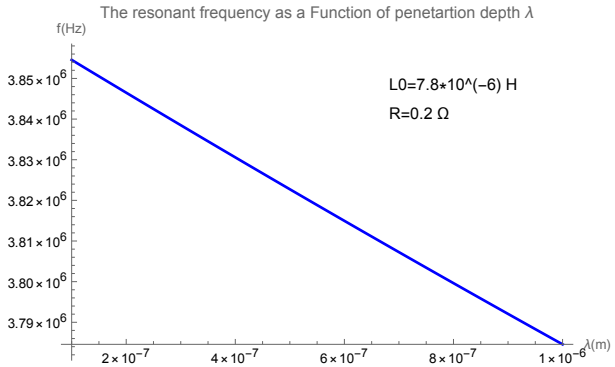

Figure 6.8: The resonant frequency of the circuit using pancake coil as a function of penetration depth λ

chapter 8.

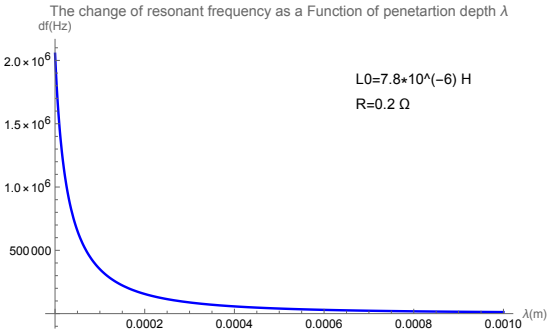

Figure 6.9: The change of resonant frequency as a function of penetration depth λ in all region

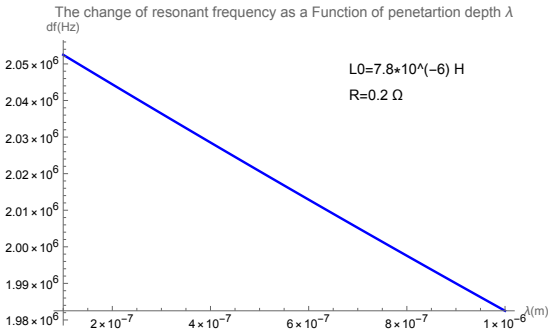

Figure 6.10: The change of resonant frequency as a function of penetration depth λ in low temperature region

6.3.3 Magnetic Vector Potential

While the numerical value of the vector potential may not be directly measured in experiments since we are only interested in the change of resonant frequency, it plays an important role in comparing the theoretical model with simulation results. In the axial-symmetric case, this comparison is straightforward because the only nonzero component of the vector potential is the θ-component in cylindrical coordinates. Theoretically, the θ-component can be computed via numerical integration, as defined by equations (5.26) and (5.54). In this study, only the numerical result of equation (5.54) was calculated. This is because, first, the geometry setup for the approximated spiral coil model in FEMM is relatively simple, as will be explained in the next section; and second, the approximated spiral coil model is more relevant from our experimental perspective and remains a theoretically unverified model.

First, we calculated the vector potential along an arbitrary straight line at the vicinity of a spiral coil. This line must not get to close to the spiral coil as it will cause the divergence problem in theoretical model. And also not too far away because the vector potential becomes too small at there therefore lost the meaning of comparison. One of the proper choice is the line parallel to z axis, located at $r = 30\mu m$ in the cylindrical coordinate, and one can omit the polar angel because the potential is axial-symmetrical. The result of the vector potential calculated base on theoretical model is shown in Figure 6.11. As seen in the plot, the magnitude of magnetic vector potential A initially increases as z approaches the coil from top, reaching a maximum at around $z = -50\mu m$, and then decreases. The coil is positioned at $z = -48.5$ μm, and the point (30 μm, -48.5 μm) corresponds to the location closest to the coil. As a result, the maximum of the vector potential appears at this point in the figure.

Secondly, we make the numerical integral of vector potential as a function of λ. Figure 6.12 shows the magnetic vector potential in a range of penetration depths, including $\lambda = 9 \times 10^{-4}$ m, 9×10^{-5} m, 9×10^{-6} m, and 9×10^{-7} m, corresponding to different temperature conditions. It should be noted that the entire theoretical framework is only valid in the low-temperature regime, specifically in the region of very small penetration

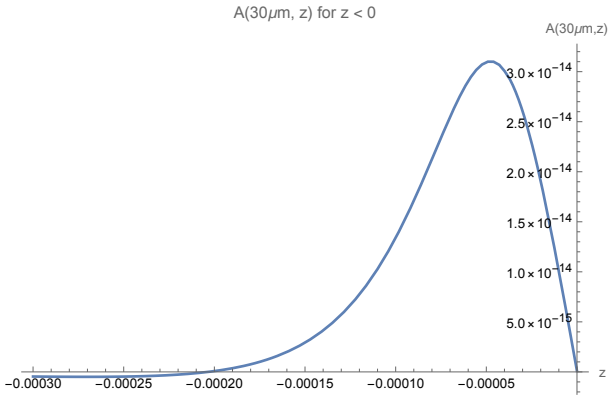

Figure 6.11: The magnitude of the magnetic vector potential of the spiral coil calculated by the axis-symmetric theoretical model plotted along the line parallel to z axis, ranging from ($30\mu m$,0) to ($30\mu m$,$-300\mu m$), where r and z represent the radial length r and height z in cylindrical coordinate respectively.

depths, typically around 100 nm to 1000 nm. The above range of variation is quite larger than the effective region, this is because our primary intention here is to test the effect of varying penetration depth on the magnetic penetration behavior. To make the effect more obvious, a large range of variation of penetration depth was tested. In reality, a superconductor exhibits such variation only within a specific temperature range. Namely, between the 0 K and critical temperature, where the material remains in the mixed state and the penetration depth depends sensitively on temperature.

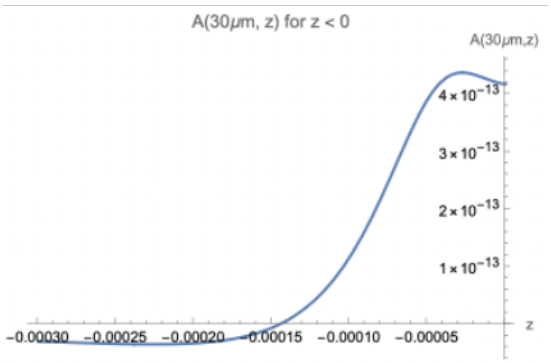

(a) $\lambda = 9 \times 10^{-4}\,\mathrm{m}$

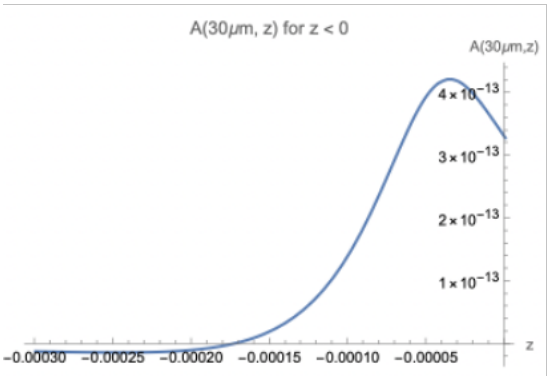

(b) $\lambda = 9 \times 10^{-5}\,\mathrm{m}$

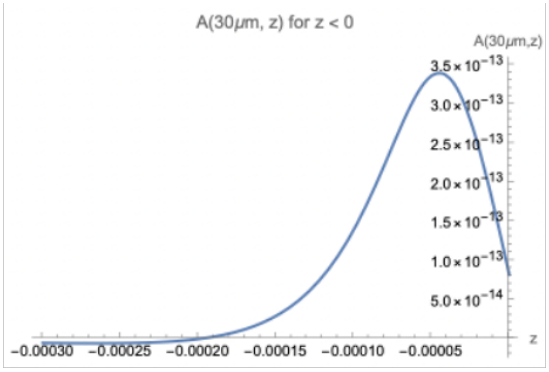

(c) $\lambda = 9 \times 10^{-6}\,\mathrm{m}$

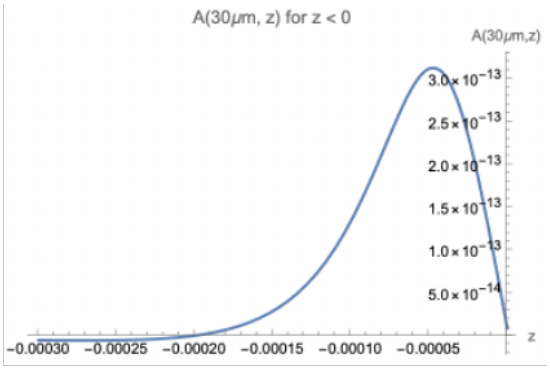

(d) $\lambda = 9 \times 10^{-7}\,\mathrm{m}$

Figure 6.12: Magnetic vector potential calculated in Mathematica for different effective London penetration depths λ of the superconducting block.

Chapter 7

Magnetic Field Simulation

7.1 FEMM Simulation

7.1.1 Introduction

The Finite Element Method Magnetics(FEMM) is a two dimensional simulation tool specifically designed for solving electromagnetic problems [37]. FEMM operates by discretizing the geometry into finite elements and solving Maxwell's equations numerically using the magnetic vector potential formulation.

FEMM consists of three main components: a graphical user interface for geometry construction and boundary condition definition, a mesh generator for spatial discretization, and a solver that computes field quantities such as the magnetic vector potential and the magnetic flux density.

It is important to note that FEMM is limited to two-dimensional simulations, and its applicability is confined to systems that are either planar or 3d problems possessing axial symmetry. This constraint implies that FEMM cannot simulate general three dimensional current distributions or asymmetric configurations. However, for some of the axis-symmetric coils considered in this work, FEMM provides an efficient and reliable way of evaluating the magnetic vector potential distribution.

Since FEMM is a Windows-based application and does not have any version for macOS, the simulation was performed on a Mac computer using virtualization software. In this work, VMware Fusion was used to run a Windows 11 virtual machine on macOS, which enables the installation and execution of FEMM at a macOS laptop.

7.1.2 Geometry and Material Properties Setup

Since we want to simulate the axis-symmetric coil, the problem type was set to `Axis-symmetric`. The length unit was chosen as `Millimeters`, and the operating frequency was defined as 4 MHz, consistent with the experimental setup. A depth value of 1 was used, which in axis-symmetric mode acts as a normalization factor rather than a physical thickness.

The mesh quality was controlled by setting the solver precision to 1×10^{-8}. A minimum angle of 30° was chosen to enhance the quality of mesh elements, and the `Smart Mesh` option was enabled to allow FEMM to automatically refine the mesh based on geo-

metric features. The AC magnetic solver was set to `Successive Approximation`, which is appropriate for weakly nonlinear materials.

In the FEMM simulation, the 3-d axis-symmetric geometry was defined in a 2D cross-sectional plane. The coil was modeled with a rectangular cross-section of $75\,\mu\text{m} \times 37\,\mu\text{m}$, placed at a height of $h = 40\,\mu\text{m}$ below the x-y plane. The geometry includes six coil turns, evenly spaced at $150\,\mu\text{m}$ intervals to approximate an Archimedean spiral shape coil.

The coil wire was modeled as copper with a gauge of 18 AWG. The relative permeability was assigned as $\mu_r = 1$, which assumes that the wire is non-magnetic material. The electrical conductivity was set to $\sigma = 58$ MS/m, corresponding to the typical value for high-purity copper. The currents in adjacent cross-sections flow in opposite directions, as required by the geometry of the spiral coil.

The superconducting sample used in the simulation was modeled as a rectangular block located above the spiral coil, centered along the z axis. The surface of sample towards the coil cross-section was placed at z=0 plane(as shown in Figure 7.2).

In the FEMM model, the material properties of Nb_3Sn were approximated based on its superconducting behavior under the operating frequency of 4 MHz. Since FEMM does not directly support superconducting materials, the superconductor was represented as a linear material with extremely high electrical conductivity and near-unity relative permeability. Specifically, the relative permeability was set to $\mu_r = 1$, assuming that the material does not exhibit magnetic enhancement, and the electrical conductivity was set to $\sigma = 1 \times 10^8$ S/m to approximate the zero-resistance condition typical of superconductors.

These parameters ensure that the induced current distribution in the Nb_3Sn film accurately reflects its shielding behavior, allowing the simulation to capture the correct magnetic field perturbation at the vicinity of the coil.

The simulation domain was extended sufficiently far from the coil to avoid boundary-induced field distortion. To emulate an open boundary condition in the two dimensional FEMM simulation, the outer semicircular region was divided into multiple annular blocks (u1 to u7), each assigned a distinct relative permeability(as shown in Figure 7.1). The permeability was carefully chosen to alternate between high and low values (e.g., $\mu_r = 0.033$ to $\mu_r = 429$), forming an artificial absorbing boundary. This graded magnetic shell functions analogously to a perfectly matched layer, which makes magnetic flux to gradually decay without artificial reflection at the boundary.

7.1.3 Magnetic Flux Simulation

The simulation was first performed with the superconducting sample in its superconducting state, modeled with a conductivity of $\sigma = 1 \times 10^8$ S/m. In this simulation, the relative permeability was naively set to $\mu_r = 1$. However, in reality, a superconductor in the superconducting state exhibits perfect diamagnetism, and the ideal value should be $\mu_r = 0$ except within the thin surface region at the order of the penetration depth. Despite this naive assumption, the simulation results remained consistent with expectations. When $\sigma = 1 \times 10^8$ S/m, the sample exhibited a nearly perfect Meissner effect, with the magnetic flux inside the superconducting block being almost entirely expelled(as shown in Figure 7.3).

In order to compare the above result with theoretical model, the result of the magnetic flux along the line located at center of the coil was extracted. The exact location of data

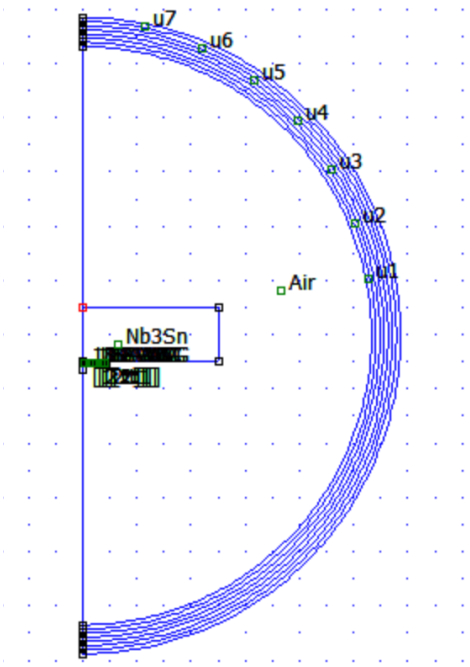

Figure 7.1: Overall geometry defined on the 2D cross section.

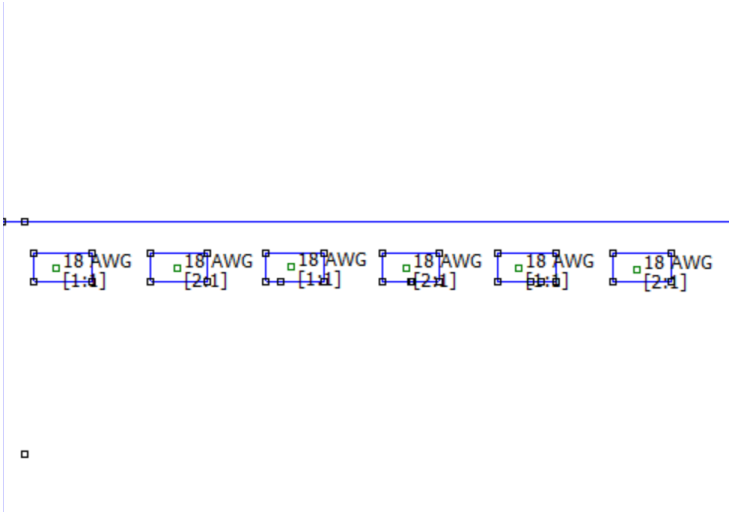

Figure 7.2: Locally magnified view of the coil cross section.

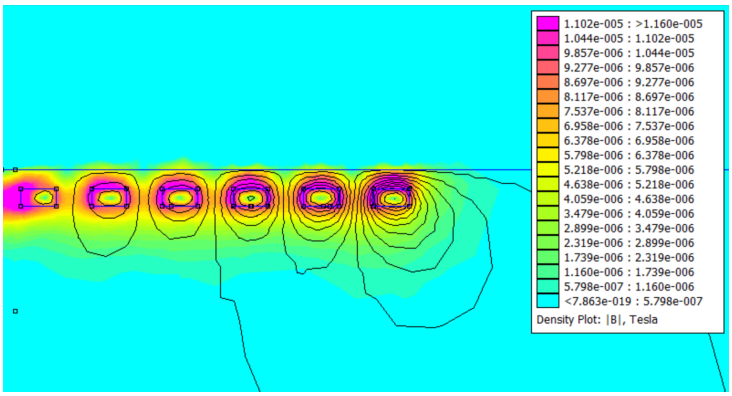

Figure 7.3: The simulation result with wire cross-section $75\,\mu\text{m} \times 37\,\mu\text{m}$, where conductivity of the sample is set as $\sigma = 1 * 10^8 S/m$.

extraction line was placed at $30\mu m$ off the z-axis, perpendicular to the surface of the sample, i.e. the x-y plane. The extracted data includes the real part, imaginary part, and magnitude of the magnetic flux in units of Weber(Wb). As shown in Figure 7.4, the magnetic flux reaches a maximum when it has the same z axis value with the center of the coil cross-section($z = -58.5\mu m$), and decreases as it get far away from the coils. The real component dominates, while the imaginary component remains relatively small, indicating that the system is primarily inductive. This observation agrees with conclusion from the two-fluid model of superconductor.

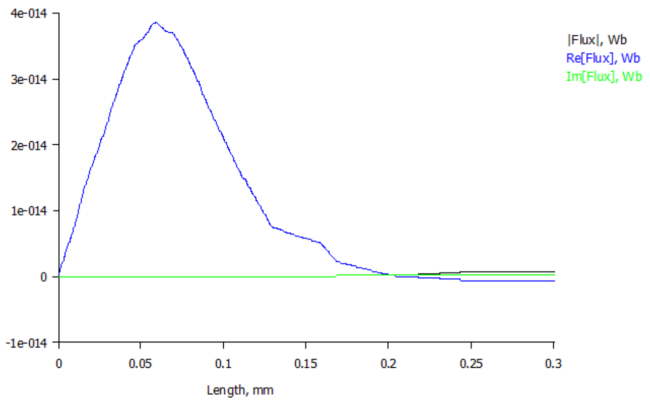

Figure 7.4: The simulation result of magnetic flux density distribution on the z-axis with wire cross-section $75\,\mu\text{m} \times 37\,\mu\text{m}$, conductivity of the sample $\sigma = 1 * 10^8 S/m$. The horizontal axis represents the position along the cut-line in millimeters.

Another simulation was conducted to evaluate the effect of the wire cross-sectional size on the simulation results using a point cross-section approximation. This was achieved by reducing the cross-sectional area of the wire by a factor of 100 (As shown in Figure 7.5). The results show that the peak of the magnetic flux curve becomes less sharp when the cross-section is reduced(As shown in Figure 7.6). This result will later be used for comparison with the theoretical predictions of magnetic flux. It is expected that a smaller cross-sectional size leads to better agreement with the theoretical results calculated in

chapter 5.

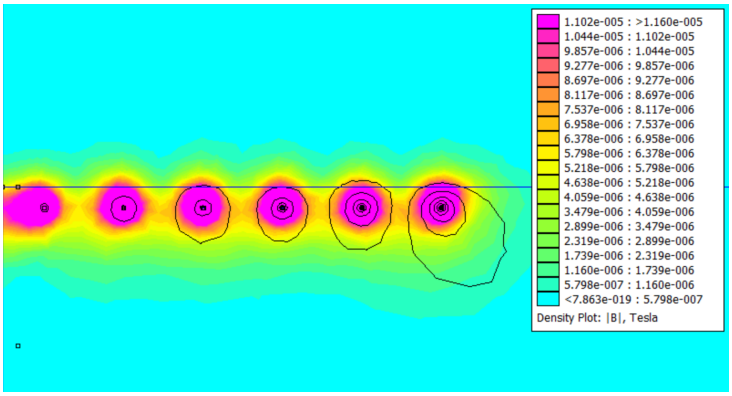

Figure 7.5: The simulation result of magnetic flux density distribution on x-y plane with wire cross-section 7.5 μm $\times$ 3.7 μm, conductivity of the sample $\sigma = 1 * 10^8 S/m$.

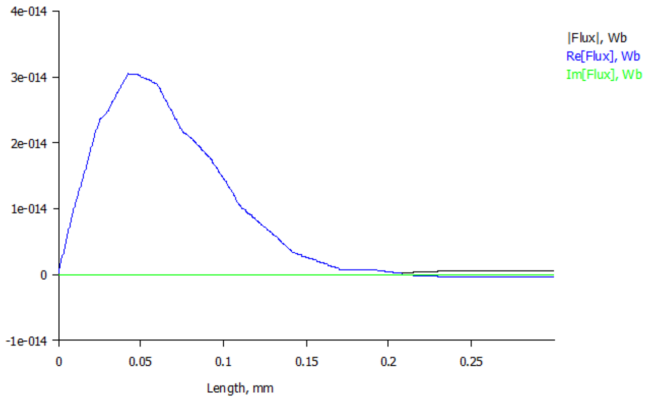

Figure 7.6: The simulation result of the magnetic flux along the line located $r = 30\mu m$, perpendicular to the sample surface, with wire cross-section 7.5 μm $\times$ 3.7 μm and conductivity of the sample $\sigma = 1 * 10^8 S/m$.

Next, to investigate the effect of temperature, the penetration depth λ was varied by adjusting the electrical conductivity from 1×10^8 S/m to 1×10^2 S/m. While the range of conductivity used here is much larger than what would be expected in real physical systems, this setup serves as a toy model intended to clearly demonstrate the phenomenology of magnetic field penetration into a superconductor.

As shown in figure 7.6, when the sample is in superconducting state with high conductivity, the magnetic flux density starts from zero at $r = 0$, indicating perfect shielding consistent with the Meissner effect. However, as the conductivity decreases and the effective penetration depth increases, magnetic fields begin to penetrate the surface of the superconductor(See figure 7.7). This results in a nonzero initial value of flux density at the surface of the sample, which indicates that the magnetic field is no longer completely excluded at the surface of the sample block.

These results confirmed the qualitative behavior expected from superconducting phenomenology and provided valuable simulation results for comparison with both theoretical

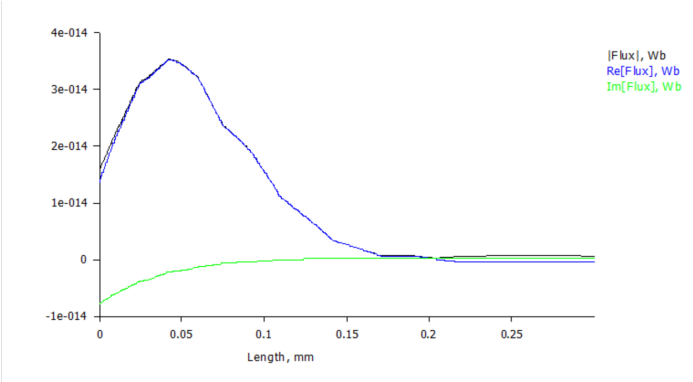

Figure 7.7: The simulation result of the magnetic flux along the line located $r = 30\mu m$, perpendicular to the sample surface, with wire cross-section $7.5\,\mu\text{m} \times 3.7\,\mu\text{m}$ and conductivity of the sample $\sigma = 1 * 10^2 S/m$.

models and experimental data.

7.1.4 Comparison with Axial-Symmetrical Model

In this section, the theoretical values of the magnetic vector potential obtained from the approximation model of the spiral coil are compared with the results of the FEMM simulation. The data extraction was performed along a line from $z = -300\mu m$ to $z = 0\mu m$ located at $r = 30\,\mu\text{m}$ in polar coordinates, perpendicular to the $r - \theta$ plane, where the value $30\,\mu\text{m}$ was chosen arbitrarily. Since the approximation model yields a magnetic vector potential that is uniform in the θ-direction, it is not necessary to specify the value of θ when extracting the data.

The geometric setup in the FEMM simulation is the same as that described in the previous section, which means that the approximated coil model, rather than the actual spiral coil, is being simulated. Nevertheless, it is still meaningful to compare the simulation results with the theoretical expressions in this case, as this serves to validate the correctness of the theoretical model developed in chapter 5, which will lead to the parametrized inductance formula that we used in experiment. It is important to note that the ultimate quantity of experimental interest is the inductance of the coil or the resonant frequency of the circuit, not the magnetic vector potential. For the comparison between theoretical and simulation results, FEMM can directly output the magnetic vector potential or magnetic flux, making it more convenient to perform the comparison using the magnetic vector potential.

Theoretically, the magnetic vector potential is given by:

$$A_\theta(r,z) = \frac{\mu_0 I}{2}\int_0^\infty sJ_\nu(sr)\left(\sum_{m=0}^{M-1}(-1)^m r_m J_1(sr_m)\frac{1}{s}e^{-s|z+h|} + C_1(s)e^{sz}\right)ds \qquad (7.1.4.1)$$

where $C_1(s)$ is defined in equation (5.37). The above expression represents the magnetic vector potential in the region $z < 0$. In the FEMM simulation, the magnetic flux density is obtained along a specified data extraction line. To perform the comparison between simulation and theory, we must calculate the magnetic flux predicted by the theoretical model.

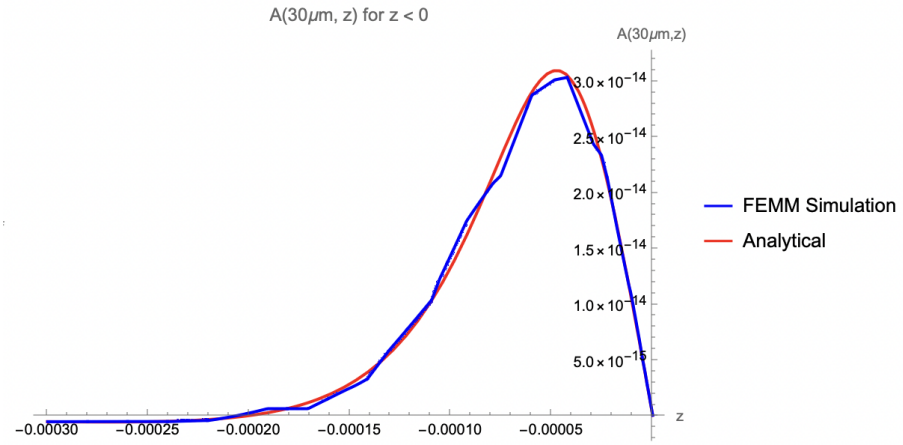

Figure 7.8: Comparison between the approximation model of the spiral coil calculated in Chapter 5 and the FEMM simulation result, where the unit of the horizontal axis is mm.

The magnetic flux penetrating some area is given as the integral of the vector potential along the boundary of that area. The spiral coil approximation model possesses an axis-symmetric distribution of the magnetic vector potential, the magnetic flux through a circular path can be computed using the formula $\Phi = A \cdot 2\pi R$, where $R = 3 \times 10^{-4}$ m. The the magnetic flux is given by:

$$\Phi(r,z) = \pi R \mu_0 I \int_0^\infty s J_\nu(sr) \left(\sum_{m=0}^{M-1} (-1)^m r_m J_1(s r_m) \frac{1}{s} e^{-s|z+h|} + C_1(s) e^{sz} \right) ds \quad (7.1.4.2)$$

The comparison for the theoretical model with FEMM simulation result is shown in Figure 7.8.

7.2 COMSOL Simulation

7.2.1 Introduction

This research uses COMSOL Multiphysics version 6.2 to run the simulation [35]. COMSOL Multiphysics is a powerful finite element analysis software designed to simulate physical phenomena in a wide range of engineering and scientific research. It offers a flexible platform for modeling complex physical systems involving electromagnetism, heat transfer, structural mechanics, fluid dynamics, and more.

The key advantage of COMSOL compared with FEMM is its ability to treat three-dimensional geometries using arbitrarily parameterized curves, making it particularly well-suited for simulating axis-asymmetric coil structures such as spiral coils. Furthermore, the Meissner effect can be effectively simulated by the cancellation of the magnetic field inside the superconductor due to mirror currents induced at the surface or by defining a region in which the magnetic field is excluded.

Table 7.1: List of Parameters Used in COMSOL

Parameter	Expression	Value	Unit
f	18×10^6	1.8×10^7	Hz
μ_0	$4\pi \times 10^{-7}$	1.2566×10^{-6}	H/m
ω	$2\pi f$	2.5133×10^7	rad/s
σ_{im}	$\frac{1}{\omega\mu_0\lambda^2}$	3.909×10^{12}	S/m
h_0	$-40 - \frac{c}{2}$	-58.5	μm
c	37	37	μm
d	75	75	μm
a	0	0	μm
b	100	100	μm
λ	90×10^{-9}	9×10^{-8}	m

7.2.2 Parameters Setting

Table 7.1 summarizes all the parameters defined in the COMSOL simulation of this research. These parameters include physical constants such as the permeability of free space μ_0, operating resonant frequency f, and the resulting angular frequency ω. a, b, c,d are parameters used for geometry construction which will be explained in the next section. Particularly, an imaginary conductivity σ_{im} was defined by the following formula:

$$\sigma_{im} = \frac{1}{\omega\mu_0\lambda^2} \tag{7.1}$$

This definition could produce Messiner effect in COMSOL as shown in Figure 7.9. But this formula fails to predict the variation of inductance of the coil, as it gives the inverse trend of inductance as penetration depth increase, which is against the theoretical prediction(see Figure 7.10 and Figure 7.11). The solution to this problem is to change the way the Meissner effect is produced. Instead of defining a purely imaginary conductivity, the superconductor can be treated as a region completely impervious to magnetic fields. The variation of the penetration depth is then realized by gradually moving the superconducting region away from the coil, where the distance of separation representing the change in penetration depth.

7.2.3 Geometry Construction

The geometry of the inductance experiment with a spiral coil was constructed using a combination of simple geometries prepared inside COMSOL, parametric curves, and work planes. As shown in Figure 7.12, the core structure consists of several rectangular blocks that define the simulation domain, where the magnetic field will vanish at those boundary. Parametric curves (`pc1`, `pc2`) were used to define the spiral coil trajectory,

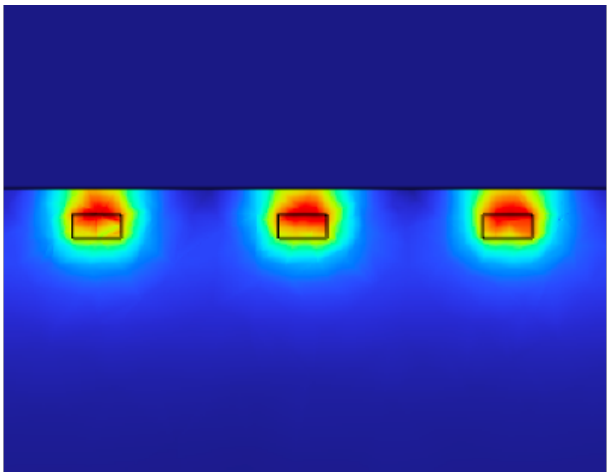

Figure 7.9: The magnetic flux distribution on the y-z plane(the coil was located at x-y plane). The electrical response of the sample gives a perfect Messier effect by using equation(7.1), where the red region represents the highest magnetic flux density.

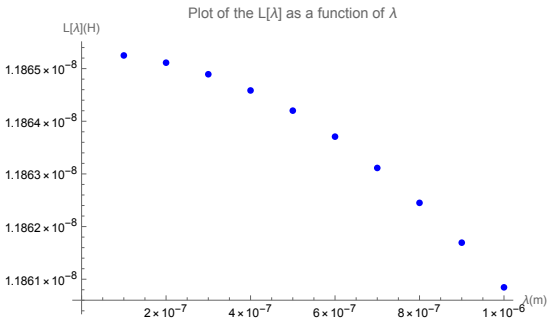

Figure 7.10: Simulation result of the inductance of spiral coil at different penetration depths from COMSOL

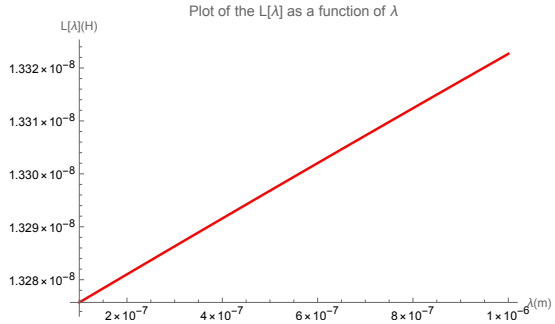

Figure 7.11: Theoretical value of inductance of spiral coil predicted by the approximation model in section 5.3.

where the following parameterizations are used for spiral 1 and spiral 2:

$$x = (a + bt)\cos\left(t + \frac{\pi}{2}\right)$$
$$y = (a + bt)\sin\left(t + \frac{\pi}{2}\right)$$

$$x = (a + bt)\cos\left(t + \frac{3\pi}{2}\right)$$
$$y = (a + bt)\sin\left(t + \frac{3\pi}{2}\right)$$

where a and b are two parameters listed in the previous section as the initial length and distance between adjacent loop of the spiral coil. By defining $\frac{\pi}{2}$ and $\frac{3\pi}{2}$ inside the sin function, the spiral coil can spiral in and out as shown in Figure 7.13

The rectangular cross-section of the spiral coil was defined on two work planes, and the size of cross-section is determined by parameters c and d as the length and width

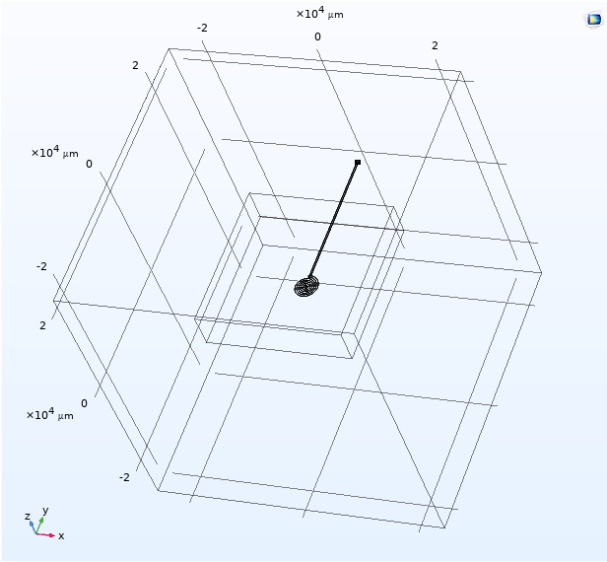

Figure 7.12: The solution boundary defined in the COMSOL. Since the spiral coil has rectangular cross-section, it is better to define the rectangular boundary.

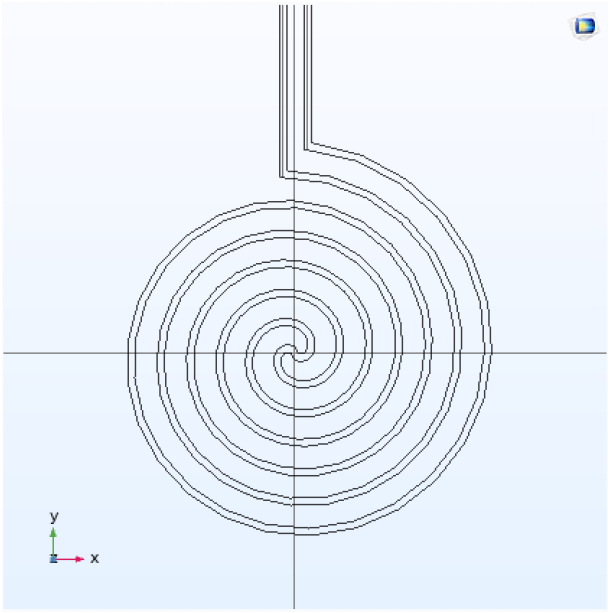

Figure 7.13: The geometry construction of spiral coil in COMSOL.

of the rectangular. The cross-section was swept along defined spiral curve (`pc1`, `pc2`) to generate three-dimensional spiral coil structures, and further extended outside the simulation domain using the `extrude` function (`ext1`, `ext2`). After all features were generated, the geometry fixing function has been used to remove unnecessary details caused by the swept function, which can optimize the meshing and reduce the simulation time significantly.

This detailed geometry setting ensures that both the spiral coil and the superconducting sample domain are modeled with high precision, which will give us the accurate prediction of the experimental value.

7.2.4 Material and Magnetic Field Setting

In this simulation, three different materials were defined: *Air*, *Copper*, and *Nb_3Sn*, each assigned to their corresponding geometric domains. The spiral coil was made using copper due to its high conductivity, while the rectangular block underneath the coil was assigned Nb_3Sn, and the material property of Nb_3Sn was assigned with default value inside COMSOL. The surrounding domain was set as air, which allows the magnetic field to propagate freely outside the superconductor.

Different physical laws are applied in each region to calculate the magnetic field, which can be achieve by using *Magnetic Fields (mf)* interface. In the air region, the magnetic field is calculated using Ampère's law in fluids. Inside the coil, the magnetic field is computed using the built-in coil feature, where the *Coil* feature in the *Magnetic Fields (mf)* interface is used to model the magnetic field produced by a coil without explicitly meshing the wire geometry. More importantly, to simulate the Meissner effect, the superconductor is modeled as a magnetic insulator. This setting is based on the consideration that the magnetic field is sufficiently low in our experiment and superconducting sample is at Messiner state, so the magnetic field can be treated as zero inside the superconductor block. However, the real physics behind it might not be described in a very accurate way since the magnetic field decays gradually in real physical world (followed by London's equations).

Table 7.2: Material and the corresponding magnetic field option in COMSOL

Geometry Name	**Material Type**	**Magnetic Field**
Spiral Coil	Copper	Terminal current
Superconducting Plate	Nb_3Sn	Magnetic insulation
Surrounding Domain	Air	Ampère's law in fluids

7.2.5 Magnetic Vector Potential Simulation Result

To calculate the inductance of the spiral coil in the presence of a superconductor placed above it, it is necessary to obtain the distribution of the magnetic vector potential along the two spiral curves. Therefore, a finite element simulation was performed using COMSOL Multiphysics. Figure 7.14 presents the simulation result of the magnetic vector potential $\vec{A}$ along the two spiral curves. The red and dark blue curves extend over a

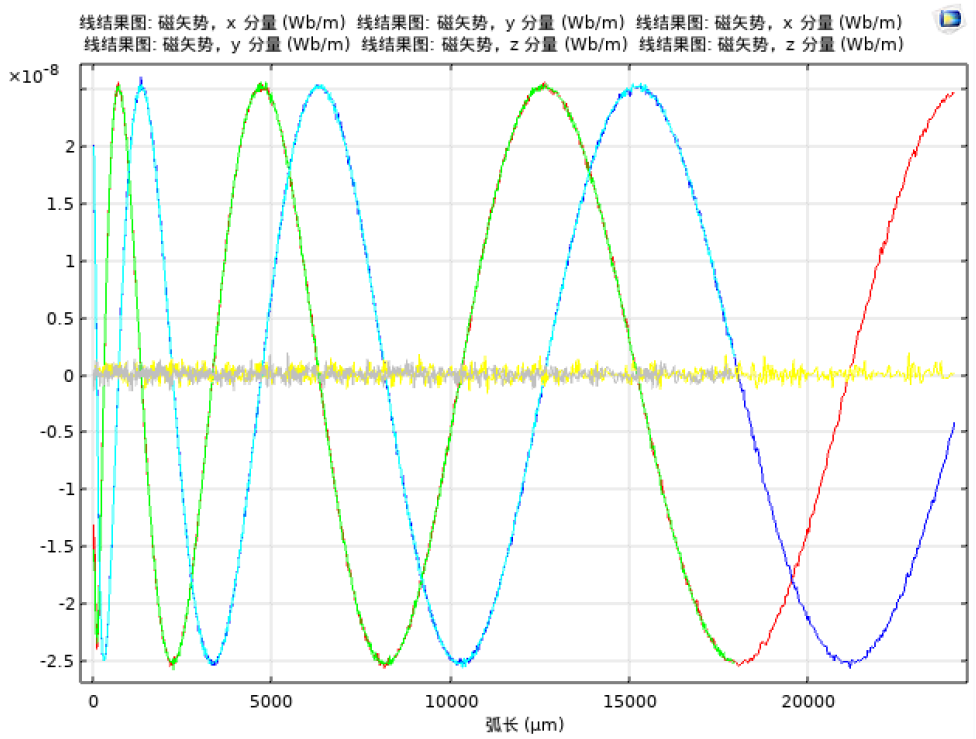

Figure 7.14: Simulation result of the x, y, and z components of magnetic vector potential along two spiral curves in Cartesian coordinate. 6 colors are used here to denote them. The horizontal axis represents the arc length along the spiral path, while the vertical axis shows the magnitude of the magnetic vector potential. The red and dark blue curves represent the x- and y-components of the magnetic vector potential along Spiral 1, respectively, while the green and light blue curves correspond to the x- and y-components along Spiral 2. The gray and yellow curves in the middle of the plot represent the z-component of the magnetic vector potential along Spiral 1 and Spiral 2, respectively.

longer range in horizontal axis than the green and light blue curves because Spiral 1 is longer than Spiral 2.

The A_x and A_y components exhibit oscillatory behavior with increasing period, which corresponds to the increasing radius of the spiral coil. In contrast, the A_z component does not display a clear periodic structure, as the current flow in the z-direction is negligible and spatially random. Furthermore, the magnitude of the A_z component is over two orders of magnitude smaller than that of A_x and A_y, and can therefore be neglected when computing the line integral of the magnetic vector potential along the spiral path.

This numerical result is used as a reference to validate the analytical expression of $A(r, z)$ derived in the section 5.4. A detailed comparison will be presented in the next subsection, where the analytical results are plotted alongside the simulation output.

7.2.6 Comparison with Axis-Asymmetric Model

To validate the axial-asymmetrical theoretical model derived in Section 5.4, the simulation results of the magnetic vector potential were compared with the corresponding numerical calculations. In the simulation, the superconducting block was removed, since

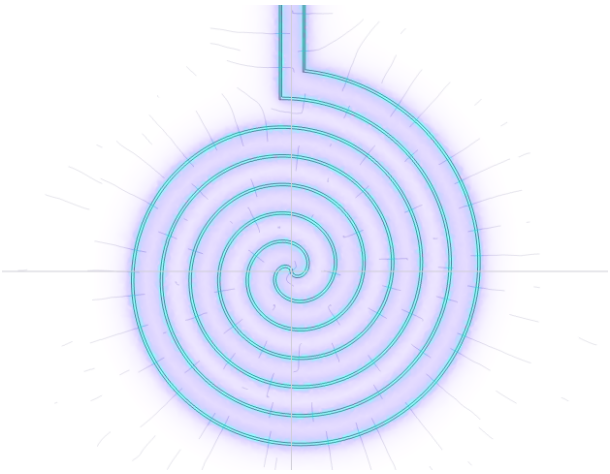

Figure 7.15: Magnetic flux distribution around the spiral coil simulated in COMSOL.

the theoretical model of section 5.4 does not account for boundary conditions induced by the Meissner effect. The comparison was carried out on the x–y plane located at $z = -1058.5\,\mu$m, which is sufficiently far from the spiral coil to avoid divergence issues in the numerical integration.

Figure 7.16 presents the comparison between the θ-component of the magnetic vector potential A_θ along the spiral coil, obtained from both the theoretical model and the COMSOL simulation. It can be seen that the simulation result agrees with the theoretical prediction to a certain extent, though some discrepancies are present. These discrepancies may be caused by the cross-sectional size of the spiral coil, as the theoretical model treats the wire cross-section as a point.

On the other hand, Figure 7.17 shows the comparison for the r-component of the magnetic vector potential A_r along the spiral coil, where a significant deviation between the theoretical and simulated values is observed. This discrepancy may be attributed to the presence of a z-component of the magnetic vector potential, as shown in Figure 7.18. Figure 7.18 illustrates the x, y, and z components of the magnetic vector potential on the x–y plane at $z = -1058.5\,\mu$m. In regions far from the coil, the z-component exhibits a comparable magnitude to the x and y components, which contradicts the theoretical model. In the theoretical formulation, the z-component of the vector potential is strictly zero, as the source current contains no z-component.

On the other hand, slight deviations in the region far away from the interface between the superconductor and coil are expected. Because the mesh densities go down significantly at the region far away from the spiral coil. Our data extraction line was located as close as possible to the region of spiral coil to make sure that the theoretical value does not diverges while maintain the enough mesh density.

Despite these differences, the periodic behavior and overall trend of the θ component of magnetic vector potential distribution are consistent between the simulation result and theoretical result as shown in Figure 7.16.

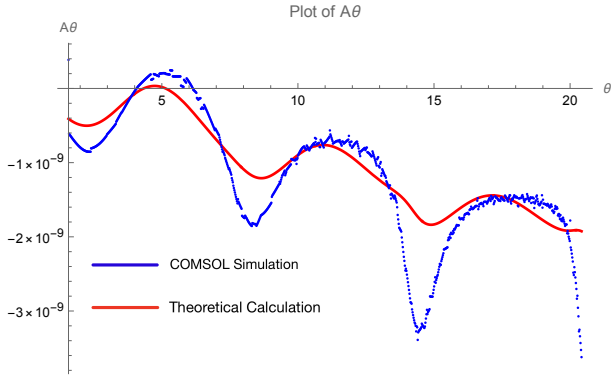

Figure 7.16: Comparison of A_θ between theoretical and COMSOL results.

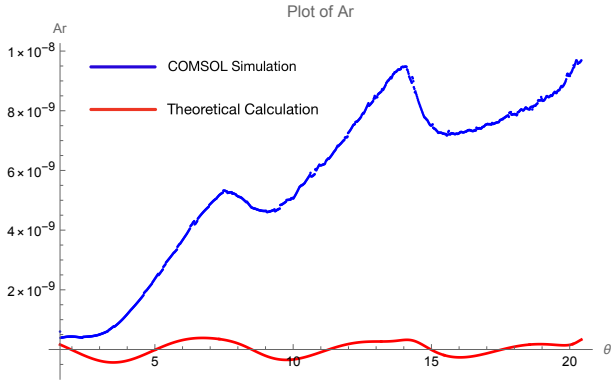

Figure 7.17: Comparison of A_r between theoretical and COMSOL results.

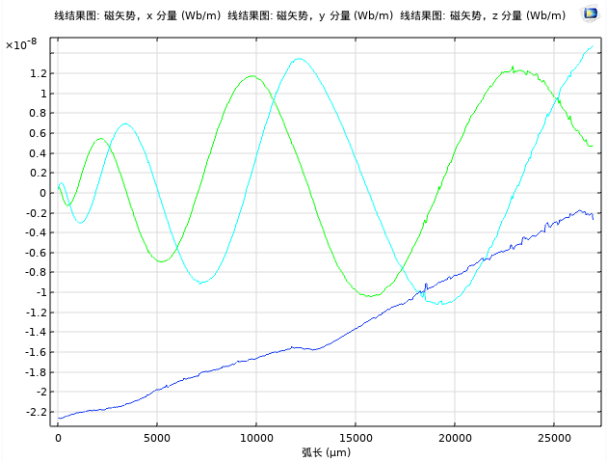

Figure 7.18: The value of x, y, and z component of magnetic vector potential along the spiral curve located at z=-1058.5μm x-y plane, where the green curve, blue curve, and deep blue curve represent the x component, y component, and z component, respectively.

Chapter 8

London Penetration Depth Measurement

In this chapter, measurements were performed both at room temperature and at cryogenic temperature. The measurement object is the resonant frequency of two resonant circuits, where a spiral coil is implemented on each of them. In both cases, the resonant frequency is recorded using a network analyzer, while the temperature during cryogenic measurement is monitored by a temperature sensor.

The room temperature measurement serves to verify the presence of resonance, determine its frequency, and evaluate the quality factor of the circuit. From the measured S_{11} parameters and resonant frequency of the circuit, one can calculate the characteristic parameters of the resonant circuit such as effective resistance and inductance of the coil.

Cryogenic temperature measurements were carried out inside a cryostat, where liquid helium was used to cool the environment around samples down to 4 K. The spiral coil boards were installed on a plane within the cryostat, positioned approximately 40 μm above the surface of the niobium samples. As the temperature changes, the penetration depth of the niobium samples varies, leading to a corresponding change in the inductance of the spiral coil, which is captured by the network analyzer. The raw resonant frequency data exhibits a sudden drop at around 9.3 K, which is identified as the critical temperature of the niobium samples. For each sample, the raw frequency data were converted into London penetration depth at different temperatures by using the inversion formula developed in Chapter 5.

8.1 Measurement at Room Temperature

8.1.1 Objective of the Measurement

The purpose of performing resonance measurements at room temperature is to determine the characteristic parameters of the resonant circuit. Specifically, the resonant frequency, the equivalent resistance R_0 and inductance L of the coil at room temperature will be determined (see Figure 8.3). The measurement is performed using an *E5071C* network analyzer, which operates over a frequency range of 300 kHz to 20 GHz. By analyzing the reflection coefficient S_{11} as a function of frequency, the resonant frequency f_0 can be identified as the point where S_{11} exhibits a sharp minimum. From the measured values of

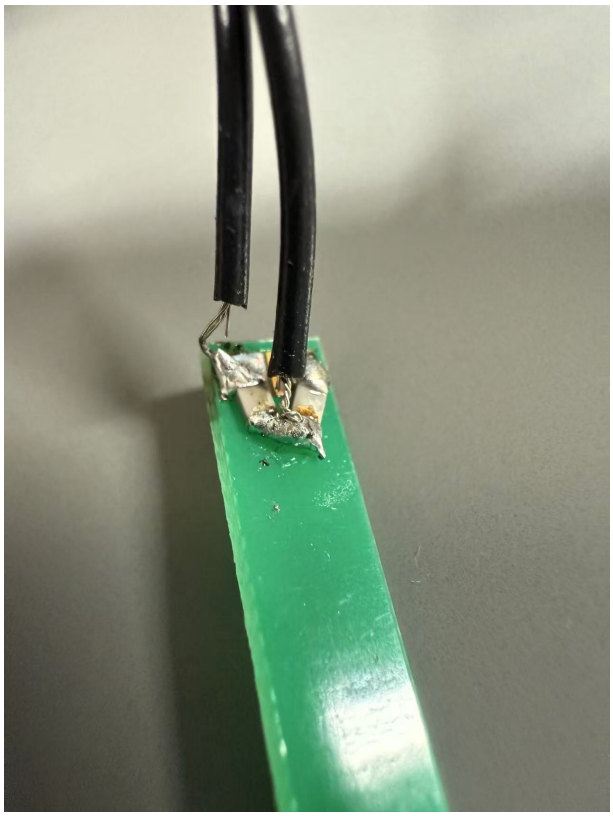

Figure 8.1: Resonant circuit composed of a spiral coil and ceramic capacitors. The spiral coil is located on the opposite side of the board. A photograph of the spiral coil is presented in Figure 8.2.

S_{11} at resonance, one can extract the resistance using the standard impedance-reflection coefficient relation. The room temperature measurement serves as a baseline reference for further research on temperature-dependent behavior of the resonant circuit at the low temperature region.

8.1.2 Experimental Setup and Methodology

The resonant circuit used in this study consists of a spiral coil and two ceramic capacitors. The PCB for the coil was provided by Dr. Iwashita, who kindly donated a PCB that had been used in previous verification experiments. The capacitors used in this study is Murata GRM2195C1H103JA01D. Murata GRM2195C1H103JA01D is a reliable multilayer ceramic capacitor designed for surface-mount applications. It is known for precision and stability, which makes it suitable for constructing various high-frequency resonant circuits. The two capacitors were installed into the circuit by using soldering. Figure 8.1 shows a photograph of the connection area where the two capacitors are installed.

The spiral coil used in this study is formed by shifting semicircles with equal radius increments in a series. The shape of the spiral coil is approximated by the parametric equation $r = a + b\theta$, where a represents the initial radius of the spiral and b represents the radius increase per turn. In this study, a is approximately zero, and b is chosen to be around $100\,\mu$m, resulting in an overall coil diameter of about 2 mm. The design values for

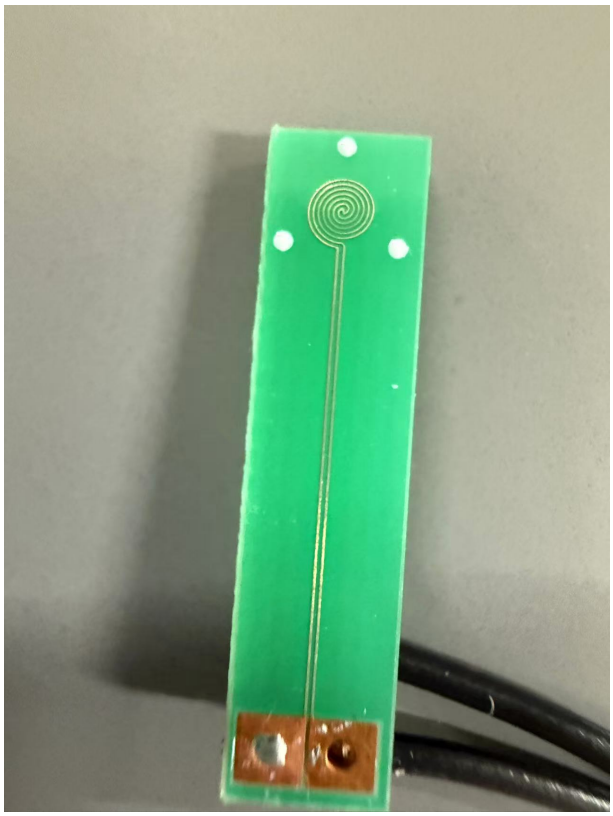

Figure 8.2: Photograph of the fabricated spiral coil on the PCB

the cross-sectional dimensions of the wire are $75\,\mu\text{m} \times 37\,\mu\text{m}$, which are consistent with the values used in the simulation section of this thesis.

The resonant circuit described above can be characterized by an equivalent circuit, which is shown in Figure 8.3.

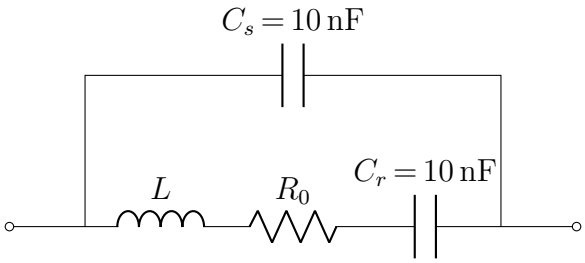

Figure 8.3: Equivalent Resonant Circuit

In the equivalent circuit, the series branch consists of an inductance L of the spiral coil and a resistance R_0 which accounts for the ohmic losses in the conductor. Two capacitors C_r and C_s have known capacitance $10nF$ as indicated in Figure 8.3 . The main target of the measurement at room temperature is to measure L and R_0 in the equivalent circuit, which can be achieved by using a network analyzer. A typical network analyzer, such as the Keysight E5071C used in this study, is equipped with two ports. Port.1 functions as the signal source, generating and delivering a known RF signal to the device under test (DUT). Port.2 is used to receive the signal transmitted through the

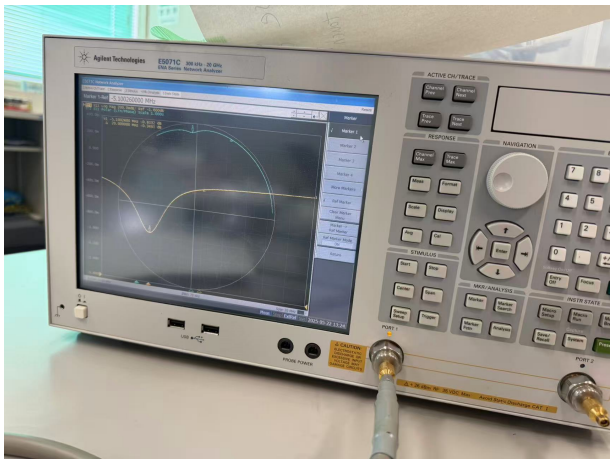

Figure 8.4: S_{11} Parameter Measurement Using Agilent E5071C Network Analyzer for coil 1.

DUT. By measuring the reflected signal at Port.1 and the transmitted signal at Port.2, the network analyzer can determine the S-parameters, such as S_{11} (the reflection coefficient) and S_{21} (the transmission coefficient). Additionally, by changing the signal source to port 2, S_{22} can also be measured. In this study, since only the resonance frequency is required, by connecting coils independently to Port 1 and Port 2 and measuring the reflection coefficients of each, two coils can be measured in a single setup, allowing two samples to be measured with a single cooling cycle. The measured quantities are the reflection coefficients S_{11} for each. With the measured value of resonant frequency and reflection coefficient S_{11} at resonant point, the L, R_0 in the equivalent circuit can be uniquely determined by solving two equations.

The first equation is the resonant frequency of the equivalent circuit, which is given by the following expression :

$$f = \frac{1}{2\sqrt{2}\pi}\left[\frac{3}{LC} - \frac{R_0^2}{L^2} + \sqrt{\left(\frac{R_0^2}{L^2} - \frac{3}{LC}\right)^2 - \frac{8}{L^2C^2}}\right]^{1/2} \approx \frac{1}{\sqrt{2}\pi}\frac{1}{\sqrt{LC}} \tag{8.1}$$

here, C_r is denoted as C. On the other hand, C_s is a coupling capacitor for the 50Ω transmission line, which does not greatly affect the resonance frequency. The R_0 here represents the resistance of the spiral coil(as shown in Figure 8.3). Using the condition $\frac{R^2}{L^2} \ll \frac{1}{LC}$, we can neglect the terms containing R_0 in the resonant frequency, and the final expression of resonant frequency is the same as a series RLC resonator.

The resonant frequency of the circuit can be identified from the S_{11} log magnitude plot displayed on the network analyzer screen. The magnitude of S_{11} is minimized at resonance, indicating better impedance matching and minimal power reflection.

In the displayed trace, the vertical axis corresponds to the logarithm magnitude of $|S_{11}|$ in dB, and the horizontal axis corresponds to the frequency. The resonant frequency is located at the point where this curve reaches its lowest value. As shown in Figure 8.4 and Figure 8.5, the minimum of the yellow curve occurs at approximately 14.99984 MHz for coil 1, and 15.179768 MHz for coil 2, which is thus identified as the resonant frequency. The relation between the reflection coefficient and the characteristic impedance of the circuit are given by:

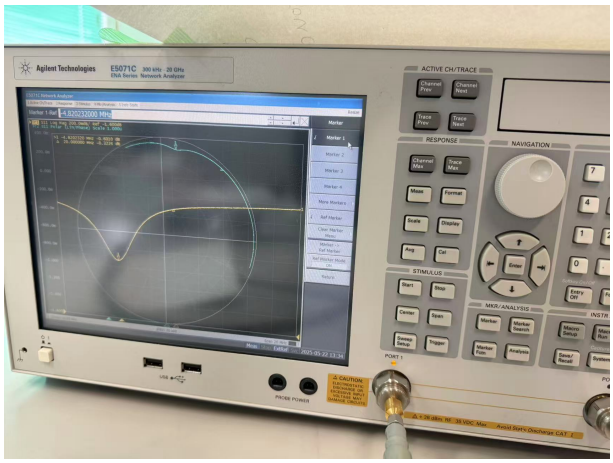

Figure 8.5: S_{11} Parameter Measurement Using Agilent E5071C Network Analyzer for coil 2.

$$S_{11} = \left.\frac{V_1^-}{V_1^+}\right|_{V_2^+=0} = \Gamma^{(1)}\big|_{V_2^+=0} = \left.\frac{Z_{\text{in}}^{(1)} - Z_0}{Z_{\text{in}}^{(1)} + Z_0}\right|_{Z_0 \text{ on port 2}} \tag{8.1.2}$$

Here, S_{11} represents the reflection coefficient at port 1 of a two-port network analyzer. The variables V_1^+ and V_1^- denote the voltage of incident and reflected waves at port 1, respectively. The condition $V_2^+ = 0$ implies that there is no incident signal at port 2, which is consistent with experimental setup. Under this condition, S_{11} is equivalent to the input reflection coefficient denoted as $\Gamma^{(1)}$, which is determined by the ratio of the difference and sum of the input impedance at port 1, $Z_{\text{in}}^{(1)}$, and the characteristic impedance $Z_0 = 50\Omega$. This relationship allows one to directly relate measured scattering parameters S_{11} to the input impedance $Z_{\text{in}}^{(1)}$, which is the impedance between two ports of the equivalent resonant circuit shown in Figure 8.3. With the known value of resonant frequency f and reflection coefficient S_{11}, we can use equation (8.1) and equation (8.1.2) to solve L, R_0 numerically. The results are summarized in the following table.

Table 8.1: Summary on Measurement results at room temperature

Coil	Measurement Result
Coil 1	Resonant frequency: $f = 15.179768$ MHz Reflection coefficient: $20\log_{10}\lvert S_{11}\rvert = -0.92 \pm 0.01$ dB Equivalent resistance: $R_0 = 1.23$ mΩ Inductance: $L = 22.5$ nH
Coil 2	Resonant frequency: $f = 14.999840$ MHz Reflection coefficient: $20\log_{10}\lvert S_{11}\rvert = -0.95 \pm 0.01$ dB Equivalent resistance: $R_0 = 1.16$ mΩ Inductance: $L = 21.9$ nH

8.2 Measurement at Cryogenic Temperature

8.2.1 Overview of the Experiment

The primary objective of this experiment was to measure the temperature dependence of the penetration depth of high-RRR Nb samples by monitoring changes in the resonance frequency of spiral coils. For this purpose, a cryogenic temperature experimental apparatus constructed by Dr. Iwashita et al. at RCNP, Osaka University, was used.

Figure 8.6 shows the experimental assembly. The cylindrical metal structure is a cryostat, a vacuum-insulated container that stores liquid helium to achieve cryogenic temperatures. Inside the chamber, a flat stage holding two spiral coils and two Nb samples was installed (see Figure 8.8). The two superconducting samples are arranged symmetrically, each with a spiral coil on top. Each coil PCB is pressed against the sample by a plate spring. On the surface of each coil, a 20 μm silk bump is placed on top of a 20 μm insulating solder resist layer, resulting in a total separation of 40 μm between the coil and the sample. A heater is located at the center of the stage to control the temperature, and two temperature sensors are positioned near the samples.

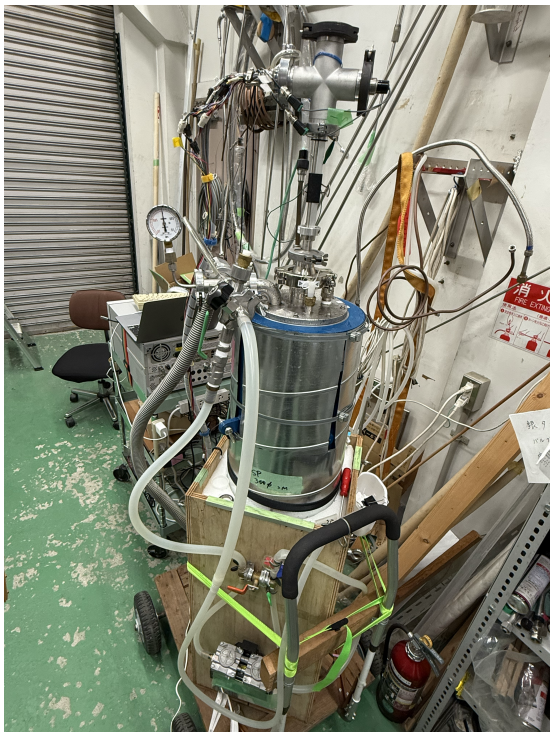

Figure 8.6: Photograph of the assembled experimental apparatus at Osaka University.

To maintain the temperature inside the vacuum chamber at around 9 K, the measurement stage installed in the cryostat was cooled using liquid helium. Before liquid helium is injected into the bottom of the chamber, the air inside the chamber is first evacuated using a vacuum pump. The internal pressure of the chamber can be read from a pressure gauge (gauge pressure) located at the top of the flange. A zero reading on the pressure gauge indicates that the chamber is at atmospheric pressure. A negative reading indicates a pressure lower than the atmospheric pressure, while a positive reading indicates a pressure higher than atmospheric pressure. If the pressure remains at approximately -0.1

Figure 8.7: The whole inner structure including the baffles for thermal insulation.

MPa for an extended period without significant fluctuations, the chamber is considered to be in a vacuum state with no leaks. After the chamber has been evacuated, we disconnect the vacuum pump and fill the chamber with helium gas through the supply line until it reaches atmospheric pressure. This step is performed to ensure that no other gases remain in the chamber, which maximizes the purity of the liquid helium to be recovered. Finally, liquid helium is injected into the chamber. The amount of liquid helium injected can be monitored using a liquid level meter. Liquid helium accumulates at the bottom of the vacuum chamber. If the sample stage becomes submerged in the liquid, its temperature will drop far below the critical temperature of niobium. Therefore, the liquid helium level must be carefully controlled to remain below the sample stage and avoid direct contact.

Baffles are used for insulation (Figure 8.7). The structure is suspended vertically from the upper flange and consists of multiple circular stages. Aluminized Mylar is used for insulation. The sample stage is enclosed in an aluminum cylinder to ensure the uniform temperature environment.

Figure 8.8: The sample stage inside the cryostat.

At the bottom, an additional heater is installed to purge liquid helium after measurement. A metal tab connected to the sample stage extends downward (see Figure 8.9). The lower end of this metal tab is immersed in the liquid helium bath and functions as a heat conductor that transfers heat from the stage to the liquid helium bath.

During the measurement, the resonant circuit with a spiral coil is connected to a network analyzer (Figure 8.10), which records the S_{11} and S_{22} scattering parameters in the vicinity of resonant frequency to determine the resonance frequency shift caused by the superconducting sample. At different temperature, all the data points from each trace at network analyzer were saved, and the temperature can be read from the screen of the temperature monitor (See figure 8.11).

In summary, this system enables stable and precise low-temperature measurements of the electromagnetic response of superconducting samples, which allows for extraction of the London penetration depth through analysis of the resonance frequency shift of the

Figure 8.9: Heater and thermal tab connected to the sample stage.

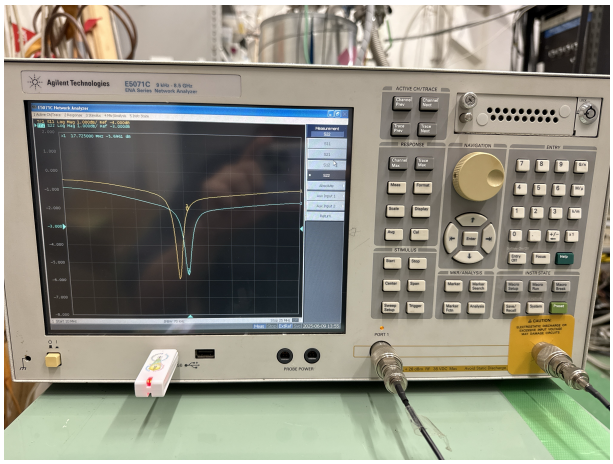

Figure 8.10: Resonance Measurement with Agilent E5071C Network Analyzer at cryogenic Temperature.

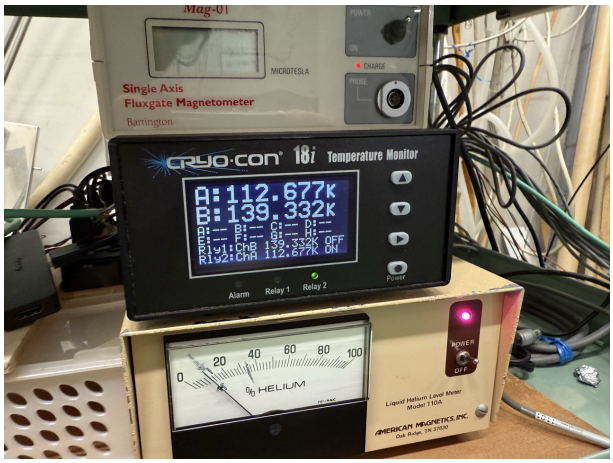

Figure 8.11: Temperature Monitor.

circuit.

8.2.2 Samples Preparation

The superconducting samples used in this study were cut from a high-purity niobium (Nb) plate. Each sample was labeled using a vibration pen for identification. After cutting, the dimensions and weights of the samples were carefully measured(as shown in Figure 8.12), and the result is shown in table 8.2.

Table 8.2: Information of Nb samples

Sample	Thickness (mm)	Length (mm)	Width (mm)	Mass m (g)	Annealing
1	2.85	20.09	20.06	97.269	No
2	2.87	20.04	20.06	97.136	Yes

Surface treatment was carried out using the Buffered Chemical Polishing (BCP) method. Following BCP method, the samples underwent a series of ultra-pure water rinsing steps, including three sequential rinses and an additional ultrasonic rinse for 20 minutes.

Both Sample 1 (I) and Sample 2 (II) were prepared from high Residual Resistivity Ratio (RRR) niobium and underwent Buffered Chemical Polishing (BCP) for 3 minutes. The key difference lies in the additional heat treatment applied to Sample 2.

Sample 2 was subjected to an annealing process at 800°C for 3 hours in a vacuum environment. This annealing step aims to remove internal stresses and hydrogen contamination from the niobium sample, which will improve its superconducting properties. In contrast, Sample 1 did not undergo any annealing. The annealing process was monitored with respect to both temperature and vacuum pressure, as seen in Figure 8.13.

8.2.3 Temperature Control

To control the temperature during the experiment, the following three methods were applied:

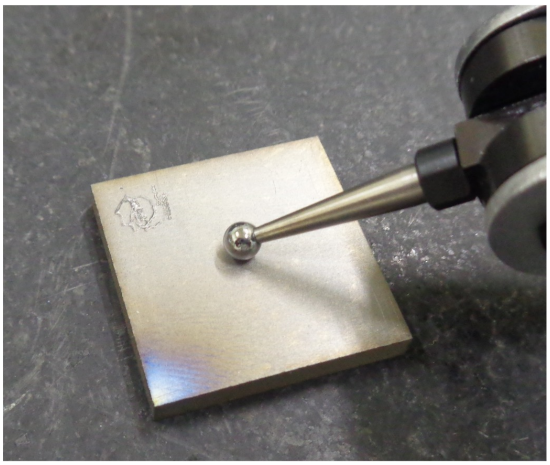

Thickness measurement of Sample 1

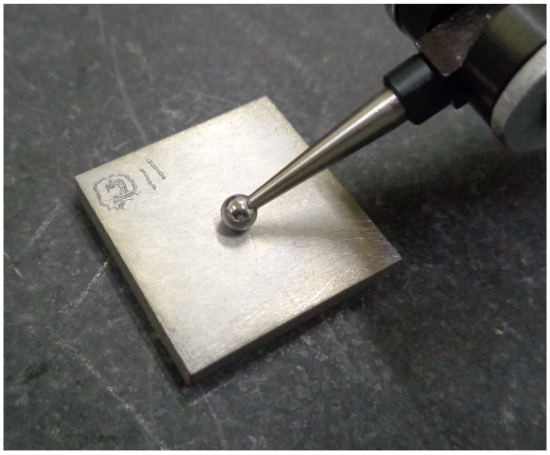

Thickness measurement of Sample 2

Weight measurement of Sample 1

Weight measurement of Sample 2

Figure 8.12: Thickness and weight measurements for Sample 1 and Sample 2. Both samples are cut from high-RRR niobium plane.

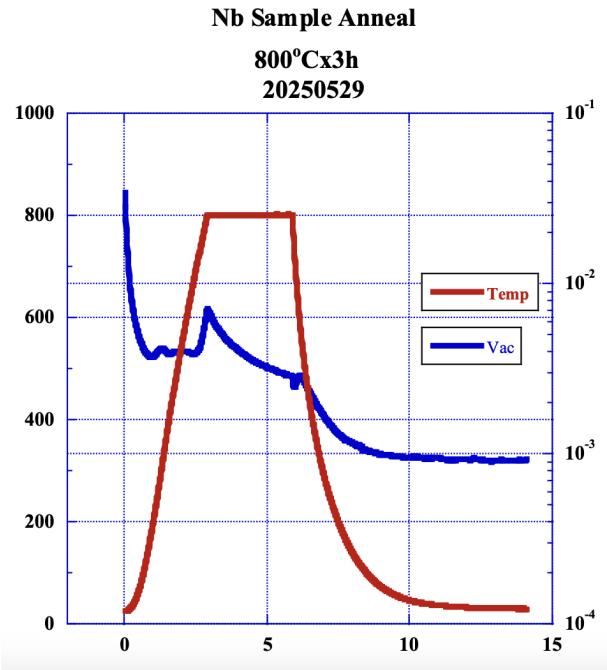

Figure 8.13: Temperature and vacuum pressure profile during the annealing process of the niobium sample at 800°C for 3 hours.

1. Raise the height of the sample stage inside the cryostat;
2. Apply voltage to the heater located at the center of the sample stage to generate localized Joule heat;
3. Activate the purge heater to stir the gas layer with the cold gas generated by the boiling of liquid helium, thereby lowering the temperature around the stage.

As for the first method, an important observation is that: at thermal equilibrium, the temperature distribution inside the cryostat varies with the distance from the liquid helium surface. The closer to the liquid helium surface, the lower the temperature. Therefore, the temperature of the sample stage can be controlled by adjusting the distance between the sample stage and the liquid helium surface. The distance between the sample stage and the liquid helium surface is adjusted by raising the stage axis. The further the axis is pulled out from the cryostat, the further the coil surface moves away from the liquid helium surface.

As the second method, this experiment uses a voltage controller to adjust the voltage applied to a resistor located at the center of the sample stage. This resistor functions as a heater. Increasing the applied voltage raises the temperature at the center of the sample stage. During heating, it is important to note that the temperature at the center may become significantly higher than that at the periphery. Therefore, after heating, it is necessary to wait for a certain amount of time until the entire sample stage reaches thermal equilibrium before reading the temperature data from the temperature monitor.

As for the third method, by activating the heater located at the bottom, the liquid helium is vaporized into cold helium gas. The cold gas then drives the lower-temperature helium gas from the bottom region upward into the warmer region near the top. As a

result, the helium gas surrounding the sample stage is replaced by colder helium gas, thereby lowering the temperature in the vicinity of the sample. One thing needs to be noticed is that the thermal tab connecting to the sample stage is located around the bottom heater. If this tab comes into contact with the heater, it may cause the temperature of the sample stage to rise. Therefore, when adjusting the height of the sample stage in method 1, one must take care to ensure that the bottom end of the tab does not touch the purge heater, in order to prevent the tab from bending and coming into contact with the heater.

8.2.4 Result of Resonant Frequency Shift

The raw data obtained from the NWA is the reflection coefficient as a function of frequency. By fitting the data points near the minimum of the S_{11} curve with a quadratic function, the resonant frequency was determined as the minimum of the fitted function. In this study, a total of five data sets were measured. To examine whether differences between the coils affect the results, one of these data sets was obtained after switching the positions of the samples. The four data sets measured before switching the samples' positions are shown in Figures 8.14 and 8.15, while one data set measured after switching the coil positions is shown in Figure 8.16 and Figure 8.17.

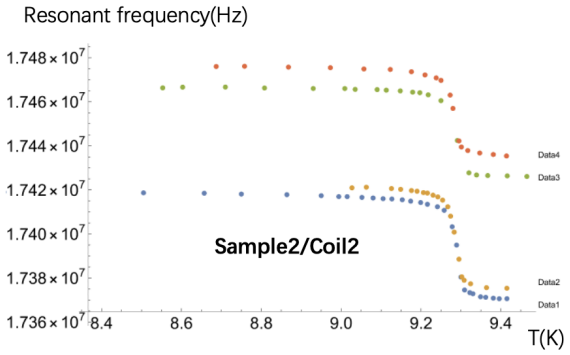

Figure 8.14: 4 sets of data from trace 1 before switching the position.

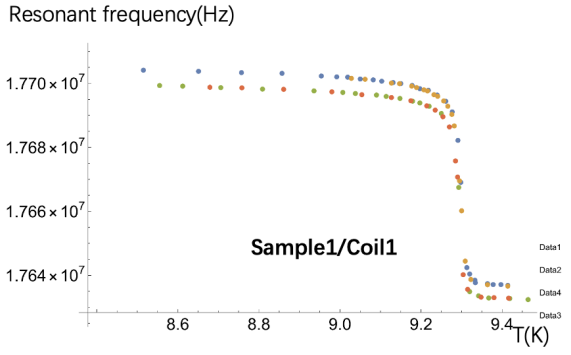

Figure 8.15: 4 sets of data from trace 2 before switching the position.

Data #	Sample # Measured by Coil 1	Sample # Measured by Coil 2
1	1	2
2	1	2
3	1	2
4	1	2
5	2	1

Table 8.3: The information of which sample was measured by which coil for all five data sets.

Table 8.3 summarizes the information of which sample was measured by which coil during all five measurements. The data from Trace 1 was obtained using Coil 1 to measure Sample 2, while the data from Trace 2 was obtained using Coil 2 to measure Sample

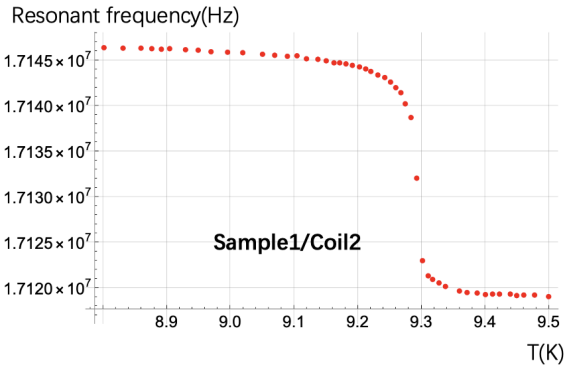

Figure 8.16: 1 set of data from trace 1 after switching the position of the sample.

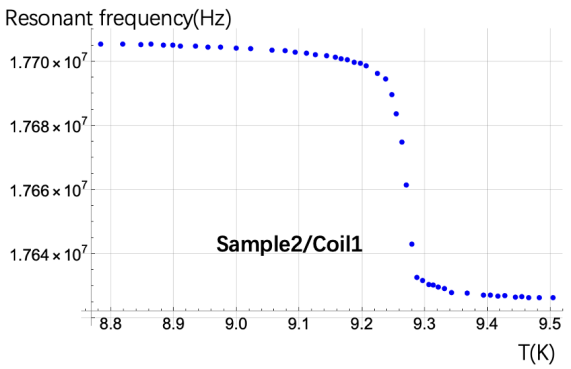

Figure 8.17: 1 set of data from trace 2 after switching the position of the sample.

1. Data points in different colors represent data sets measured at different times. These four data sets were collected at different times, so there are some variations among them. As can be seen, among the four data sets in Figure 8.14, two of them show a significant discrepancy compared to the other two. The cause of this significant discrepancy is potentially caused by the variation of the distance between the sample and the coil board. This large discrepancy results in a significant uncertainty in the absolute value of the London penetration depth. It is possible to calibrate the absolute value of the London penetration depth calculated from the resonance frequency change by measuring superconducting samples with known London penetration depth. However, such samples were not available for this measurement. Instead, we used an assumption to achieve such calibration that the resonant frequency corresponding to a penetration depth of $100nm$ calculated from theoretical formula equals the experimental measured resonant frequency at around $8.9K$. The reason for choosing $8.9K$ is that, according to the empirical formula (8.3), the penetration depth of the Nb sample reaches approximately $100nm$ at this temperature. However, the empirical formula requires an initial assumption of the critical temperature and the London penetration depth at $T = 0$ of the Nb sample. Therefore, this calibration will cause systematic error in the final result. Nonetheless, the main source of the systematic error comes from the variation of the distance between the coil board and the sample, and the error caused by this assumption is relative small compared with the error caused by the variation of distance(see Table 8.5). The critical temperature of the superconducting sample can be identified as the point at which the resonant frequency suddenly drops.

One data set measured after exchanging the positions of the samples is present in this thesis(Figure 8.16 and Figure 8.17). The purpose of measuring the resonant frequency after we exchange the positions of the samples is that we want to evaluate the impact of differences in coils on the result of the measurement. However, during this measurement, the temperature varies rapidly, which leads to a substantial error in the recorded temperature value(Table 8.3).

8.2.5 London Penetration Depth Temperature Dependence

One of the most important outcomes of this study is the trial measurement of the penetration depth $\lambda(T)$ at different temperatures T. This is achieved by transforming the raw frequency data using the inversion formula developed in Chapter 5. In this thesis, we used the effective inductance formula for a planar spiral coil, given by the following equation:

$$L = a \cdot L_0 - c \cdot \pi\mu_0 \int_0^{\infty} \frac{\left\{ e^{-sh} \sum_{m=0}^{M-1} (-1)^m J_1(sr_m) \times r_m \right\}^2}{1 + 2s\lambda \coth\left(\frac{d}{\lambda}\right)} ds \tag{8.2}$$

The relationship between the inductance of the coil and the resonant frequency can be found in equation (8.1.1). The term $a \cdot L_0$ in equation (8.1) will be fitted using COMSOL simulation data and later calibrated with the experimental data in section 8.1. The second term in equation (8.1) represents the change in inductance due to the variation in penetration depth, which will cause the resonant frequency shift. Therefore, we can get the change of resonant frequency as a function of London penetration depth of the sample. From the raw data of resonant frequency shown in previous section, we can read the corresponding temperature and London penetration depth at the same resonant frequency. The result of London penetration depth at different temperatures were presented in Figure 8.18 and Figure 8.19.

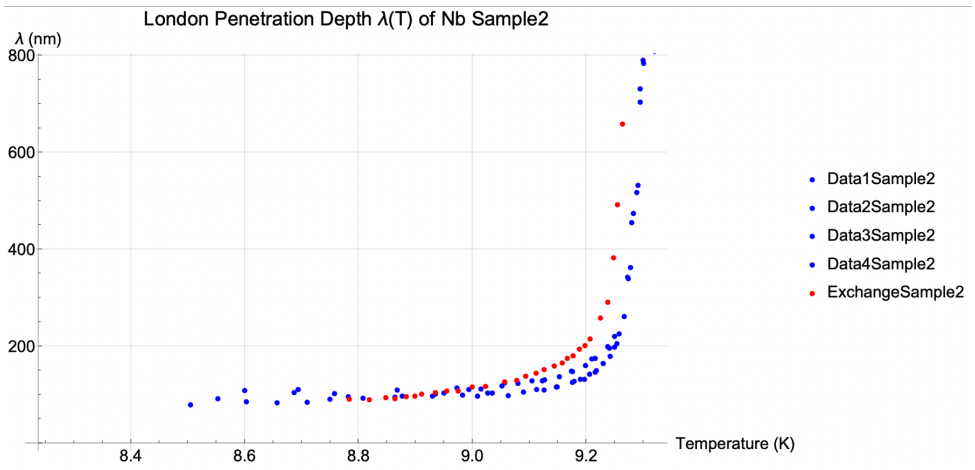

Figure 8.18: London Penetration depth of Sample 2 as functions of temperature.

In Figure 8.18 and Figure 8.19, five data sets measured from sample 2 and sample 1 were plotted respectively. The data points labeled as *ExchangeSample2* represent measurements of the same sample using a different coil, which is denoted by the red color. From these data, we observe that the results for Sample 2 obtained with different coils show a significant deviation near the critical temperature, indicating that the characteristics of the coil may substantially affect the measurement results. A similar conclusion can be drawn from Figure 8.19, where the data points labeled as *ExchangeSample1* also deviate notably from the other four data sets of Sample 1. On the other hand, data points measured using the same coil but from different samples exhibit slightly different behavior as well, which may be due to the different London penetration depth characteristics of each sample.

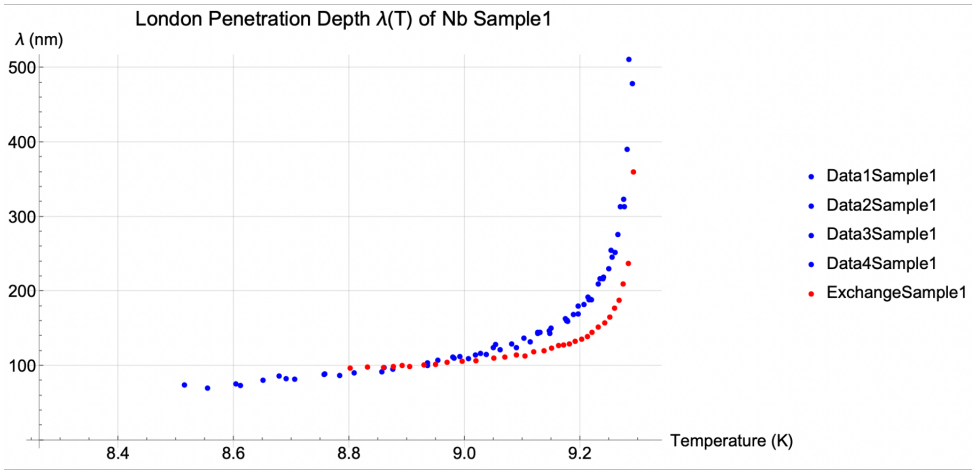

Figure 8.19: London Penetration depth of Sample 1 as functions of temperature.

We can determine the critical temperature and the London penetration depth of the sample at 0 K by fitting the data points with an empirical formula [40]:

$$\lambda(T) = \lambda(0)\left[1 - \left(\frac{T}{T_c}\right)^4\right]^{-1/2} \tag{8.3}$$

where $\lambda(0)$ is the London penetration depth at 0K. Both $\lambda(0)$ and T_c are taken as fitting parameters in this thesis. The fitting results are summarized in the table 8.4. It should be realized that the large error of the absolute value of $\lambda(0)$ for sample 2 is caused by the large variation of the absolute value of the resonant frequency shown in figure 8.14. On the other hand, the measurement result of sample 1 does not have such large variation, so the fitted value of the London penetration depth at $0K$ has relative small error compared with the result of sample 2.

Sample / Data Set	**Measured by**	T_c **(K)**	$\lambda(0)$ **(nm)**	$\lambda_1(0)/\lambda_2(0)$
Sample 1 / 1 to 4	Coil 1	9.303 ± 0.002	37.42 ± 97	–
Sample 2 / 1 to 4	Coil 2	9.3 ± 0.002	32.96 ± 525	1.1353 ± 17.5
Sample 1 / 5	Coil 2	9.310 ± 0.03	30.72	–
Sample 2 / 5	Coil 1	9.271 ± 0.03	37.1	0.8268

Table 8.4: Fitting results of the critical temperature and penetration depth at 0 K for Sample 1 and Sample 2, along with the relative ratio of $\lambda(0)$ between two samples for each data set. The label "1 to 4" represents the data measured before exchanging the positions of the samples(Shown in figure 8.14 and 8.15). The label "5" represents the data measured after exchanging the positions of the samples(Shown in figure 8.16 and 8.17).

Using the parameters presented in Table 8.4, the temperature dependence of the London penetration depth for each sample can be determined based on Equation (8.3). Note that we fitted the empirical formula to different data groups: Data 1 to Data 4 correspond to the four sets of measurements taken before switching the sample's position, while Data 5 represents the data measured after the position of sample was exchanged.

The uncertainty of temperature for Data 5 was rather large due to the rapid temperature increase, which causes the fifth data set exhibits relatively large errors in temperature readings. In contrast, the first to fourth data sets have smaller temperature reading errors, as their temperature rise was more stable. However, compared to the error in the absolute value of the resonant frequency, the temperature introduces a much smaller error in $\lambda(0)$ (as shown in Table 8.5). Based on the values provided in Table 8.5, we neglect the uncertainty in $\lambda(0)$ caused by temperature reading errors when calculating the overall uncertainty of $\lambda(0)$ in Table 8.4.

Another source of error comes from the determination of resonant frequency. The resonant frequency is determined by fitting 60 data points in the vicinity of the minimum value of S_{11}(as shown in figure 8.21).

From Table 8.4, it is evident that the uncertainties in the fitted London penetration depth, $\lambda(0)$, vary significantly between different samples and measurements. For Sample 1 (Data Set 1 to 4), the fitted value is $\lambda(0) = 37.42 \pm 85$ nm, where the uncertainty is more than twice the measured value, indicating very low precision. Similarly, for Sample 2 (Data Set 1 to 4), $\lambda(0) = 32.96 \pm 502$ nm, with an extremely large uncertainty compared to the fitted value of Sample 1, making the result unreliable(as demonstrated in Figure 8.20). In contrast, measurements for Data Set 5 of Sample 1 and Sample 2 yield $\lambda(0) = 30.72$ nm and $\lambda(0) = 37.1$ nm, respectively, but the uncertainties are not provided because there is only one set of data.

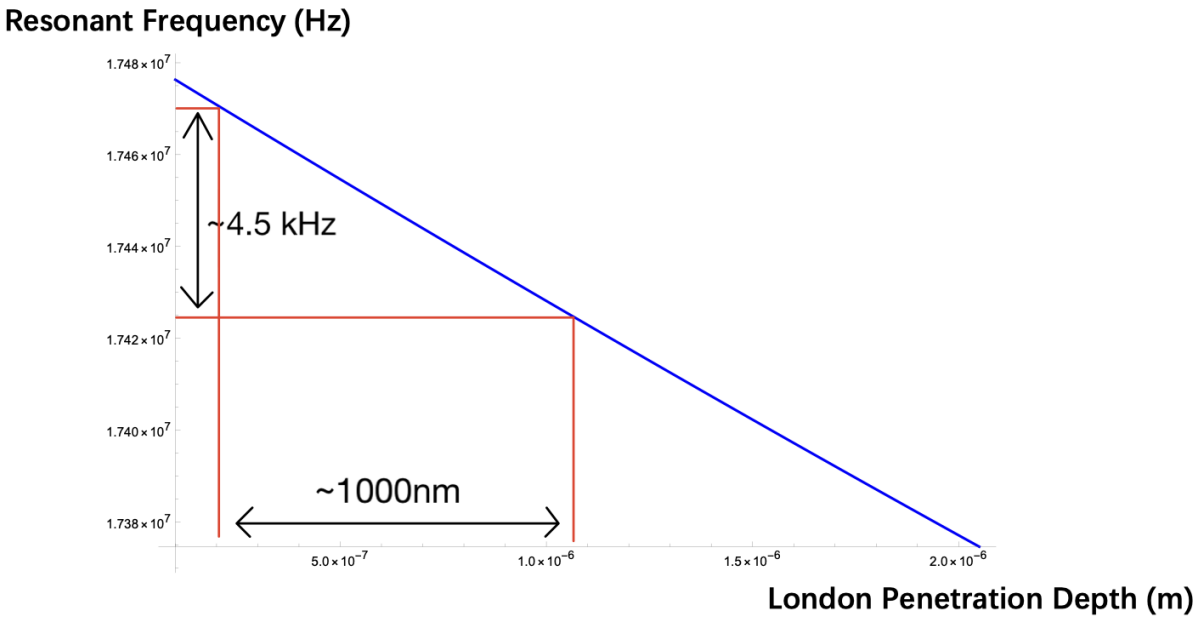

Figure 8.20: Error propagation demonstration in resonant frequency measurement for data sets 1–4 of Sample 2. The blue curve is calculated based on the theoretical formula developed in Chapter 5. As shown in Figure 8.14, the absolute value of the resonant frequency shows a discrepancy of approximately 4–5 kHz, which results in an error of about 1000 nm in the estimation of $\lambda(0)$.

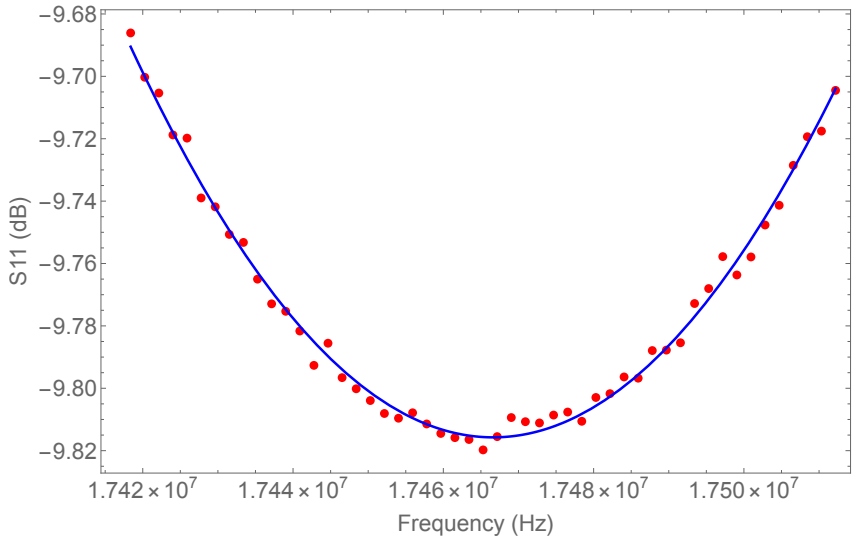

Figure 8.21: The determination of resonant frequency from raw data. We first fit the 60 data points around the minimal value of S_{11} with a quadratic function, and the resonant frequency is identified as the minimal point of that quadratic function. The accuracy of this fitting will have impact on the accuracy of $\lambda(0)$. We use the covariant matrix of the fitted parameters together with the derivative of frequency with respect to each parameters at minimal point of quadratic function to determine how much uncertainty will propagate into the result of resonant frequency. The maximum error caused by this fitting is shown in Table 8.5.

Table 8.5: Sources of error and estimation of their impact on $\lambda(0)$.

Error Source	**Error Magnitude**	**Resulting Error in $\lambda(0)$**
Temperature Reading	0.03 K	$\approx \pm 0.03$ nm
Distance between the Sample and Coil	4.5 kHz	$\approx \pm 500$ nm
Resonance Frequency Fitting	0.25 kHz	$\approx \pm 2.3$ nm
Capacitance	0.5 nF	$\approx \pm 0.64$ nm
Parameter c	0.03	$\approx \pm 0.7$nm
Assumption (λ(100nm)=λ(8.903K))	40 nm	$\approx \pm 20$ nm

Chapter 9

Conclusions

In the London penetration depth measurement, with a planar spiral coil of 2 mm diameter, a resonant frequency shift of about 6 kHz was successfully observed. This resonant frequency shift is caused by the transition of the Nb sample from the superconducting state to the normal state. Compared to previous studies [17], the planar spiral coil features lower fabrication cost and a simpler manufacturing process, which significantly reduces the overall experimental budget.

In the theoretical calculation of the inversion formula, the most significant difference between the spiral coil and those used in previous studies is that its current distribution does not possess axial symmetry in three dimensional space. This makes it extremely difficult to obtain an analytical solution to Maxwell's equations with boundary conditions involving a finite-thickness superconducting bulk. In order to obtain an analytical solution for the spiral coil under those boundary conditions, an approximation model of the spiral coil is proposed [34]. The approximation model is designed to be axis-symmetric in three-dimensional space, which enables the derivation of an analytical solution to Maxwell's equations. In the case of a coil with an axis-symmetric current distribution, the Maxwell's equations can be reduced to ordinary differential equations via the Hankel transformation. The inhomogeneous solution of the ordinary differential equation in the region containing the coil can be obtained either from the two-dimensional Green's function (Equation 5.21) proposed in this thesis or from the inverse Fourier transform of the Hankel-transformed solution in that region (Equation 5.54). To account for the effects of the finite cross-sectional size and spiral geometry of the coil, a parameterized expression for the inductance of the spiral coil was proposed. This parameterized model is based on the important fact that, within a small low-temperature range, the inductance of the spiral coil has a linear relationship with the London penetration depth. This parametrized expression was first fitted to simulation results obtained from COMSOL, and subsequently refined using experimental data to calibrate the absolute value of the resonant frequency. The absolute calibration of the resonant frequency should be performed using a sample with known value of London penetration depths. Since such a sample was not available in this measurement, we assumed that the resonant frequency calculated theoretically for a penetration depth of 100 nm corresponds to the resonant frequency measured experimentally at 8.903 K.

Measurements were performed using two niobium (Nb) superconducting samples under cryogenic conditions, where Sample 2 was subjected to an annealing process at 800°C

for 3 hours in a vacuum environment, whereas Sample 1 was not. From the resonant frequency shift data, the temperature-dependent London penetration depth for both samples was extracted using the inversion formula developed in Chapter 5. The results revealed distinct London penetration depth behavior for each sample, and the values of the critical temperature T_c and the zero-temperature London penetration depth $\lambda(0)$ were obtained through fitting with empirical formula. However, a comparison of measurements on the same sample using different coils shows significant discrepancies, indicating that part of the variation originates from the differences in coils rather than differences in the samples. Among the five extracted data sets, Data 1 to Data 4 were obtained before the sample position was exchanged. These four data sets exhibit relatively small temperature reading errors due to stable temperature variation during the measurement. By fitting these four data sets, the fitted value of $\lambda(0)$ was estimated to be 37.42 ± 97 for Sample 1 and 32.96 ± 525 for Sample 2, while the critical temperatures of both samples were fitted to be around 9.3 K. For the fitted result of $\lambda(0)$, sample 2 exhibits a larger error compared to sample 1 as shown in Table 8.4. This large error originates from discrepancies in the absolute value of the resonant frequency measured at different times(as shown in Figure 8.14). The discrepancies observed in Figure 8.14 arise from variations in the distance between the coil board and the sample during measurement. In this thesis we use a metallic strip to keep the distance between the sample and coil board, and there is no guarantee that the distance between the sample and the coil remains unchanged after exchanging samples' position. Future experiments should use better methods to control and maintain this distance during the measurement.

In addition, this study lacks sufficient data collected after the sample positions were exchanged. Future research should aim to extract adequate data both before and after exchanging samples' positions, in order to evaluate the influence of coil differences on the measurement results. It is important to note that the different amount of liquid helium injection will significantly affect the temperature variation during the measurement. If we inject the liquid helium to the maximum level in the cryostat, the temperature variation will become much stable. Furthermore, it is recommended that future studies use multiple coils to measure the London penetration depth of the samples and determine the final result by averaging the measurements obtained from different coils.

In summary, this thesis presents a methodology for measuring the London penetration depth and critical temperature of bulk superconducting samples at 0 K. These findings make a direct contribution to the advancement of SRF technology for the ILC.

Appendix

Integral Representations and Identities

$$\Gamma(z)\Gamma(1-z) = \frac{\pi}{\sin(\pi z)} \tag{9.1}$$

$$\Gamma(\nu+1) = \frac{2^{\nu}\Gamma\left(\frac{\nu+1}{2}\right)\Gamma\left(\frac{\nu}{2}+1\right)}{\sqrt{\pi}} \tag{9.2}$$

$$\frac{\Gamma(\alpha)\Gamma(\beta)}{\Gamma(\gamma)}F(\alpha,\beta;\gamma;z) = \frac{1}{2\pi i}\int_L \frac{\Gamma(\alpha+s)\Gamma(\beta+s)}{\Gamma(\gamma+s)}\Gamma(-s)(-z)^s\,\mathrm{d}s \tag{9.3}$$

$$(x)_{\underline{n}} = \frac{\Gamma(x+1)}{\Gamma(x-n+1)} \tag{9.4}$$

$$(x)_{\overline{n}} = \frac{\Gamma(x+n)}{\Gamma(x)} \tag{9.5}$$

$$\int_0^1 u^{m-\frac{1}{2}}(1-u)^{\nu-\frac{1}{2}}\,du = \frac{\Gamma\left(m+\frac{1}{2}\right)\Gamma\left(\nu+\frac{1}{2}\right)}{\Gamma(m+\nu+1)} \tag{9.6}$$

$$\begin{aligned}\int_0^1 t^{2k}(1-t^2)^n\,dt &= \frac{1}{2}\int_0^1 \mu^{k-\frac{1}{2}}(1-\mu)^n\,d\mu \\ &= \frac{1}{2}\cdot\frac{\Gamma\left(k+\frac{1}{2}\right)\Gamma(n+1)}{\Gamma\left(n+k+\frac{3}{2}\right)} = \frac{1}{2}\cdot\frac{\Gamma\left(k+\frac{1}{2}\right)\Gamma(n+1)}{(n+\frac{3}{2})_{\overline{k}}\,\Gamma\left(n+\frac{3}{2}\right)}\end{aligned} \tag{9.7}$$

The Hypergeometric Differential Equation

Hypergeometric differential equation is defined as:

$$u''(t) + \frac{(\alpha+\beta+1)t-\gamma}{t(t-1)}u'(t) + \frac{\alpha\beta}{t(t-1)}u(t) = 0 \tag{9.8}$$

where t is a complex number, α and β are parameters of the equation. Also we can see that this equation has three regular singular points at z=0 and z=1, z=∞. The ordinary differential equation with three regular singular point is called the Papperitz equation. A

general strategy of solving Papperitz equation is that we can assume the solution has the following form:

$$u(t) = (t - t_0)^{\lambda} \left(1 + \sum_{n=1}^{\infty} a_n (t - t_0)^n \right) \tag{9.9}$$

After submitting this ansatz to the equation above, each coefficients of $(t - t_0)^m$ must be zero and this will give us the indicial equation:

$$\lambda^2 + (p_0 - 1)\lambda + q_0 = 0 \tag{9.10}$$

Now to investigate the solution around the vicinity of z=0, we rewrite the above equation:

$$u''(t) + \frac{P(t)}{t} u'(t) + \frac{Q(t)}{t^2} u(t) = 0 \tag{9.11}$$

where we assume that Q(t) and P(t) are analytic at the vicinity of the singular point t_0, so we can expand them as series around a singular point:

$$P(t) = \sum_{n=0}^{\infty} p_n (t - t_0)^n = p_0 + p_1 (t - t_0) + p_2 (t - t_0)^2 + \dots \tag{9.12}$$

$$Q(t) = \sum_{n=0}^{\infty} q_n (t - t_0)^n = q_0 + q_1 (t - t_0) + q_2 (t - t_0)^2 + \dots \tag{9.13}$$

On the other hand, from the definition of hypergeometric equation, Q(t) and P(t) are defined as:

$$Q(t) = \frac{(\alpha + \beta + 1)t - \gamma}{(t - 1)} \tag{9.14}$$

$$P(t) = \frac{z\alpha\beta}{(t - 1)} \tag{9.15}$$

From the above equation we can read that Q(0)= γ, P(0)=0. So we have $q_0 = \gamma$ and $p_0 = 0$. Plug this result into the indicial equation and solving it we have

$$\lambda_1 = 0, \quad \lambda_2 = 1 - \gamma \tag{9.16}$$

Therefore the regular singular solutions at z=0 are

$$u(t) = 1 + \sum_{n=1}^{\infty} a_n t^n, \quad v(z) = t^{1-\gamma} \left(1 + \sum_{n=1}^{\infty} b_n t^n \right) \tag{9.17}$$

where u(z) is called the hypergeometric series. Note that the solution v(z) has an exponent $\gamma - 1$ at z=0, and this will lead to a branch point at the origin. Similarly, we can investigate the solution at singular point $z = 1$ and $z = \infty$ by the same approach. One can found that at $z = 1$, the two exponents are 0 and $\gamma - \alpha - \beta$. At $z = \infty$, the two exponents are α and β. We can denoted the set of all solutions by a symbol called Riemann's P symbol

$$u(t) \in P \left\{ \begin{array}{cccc} t_1 & t_2 & t_3 & \\ \alpha_1 & \alpha_2 & \alpha_3 & t \\ \beta_1 & \beta_2 & \beta_3 & \end{array} \right\}, \tag{9.18}$$

where a_1, a_2, a_3 represent the three regular singular points, and α, β corresponds to the root of indicial equation at that point. The three columns can be interchanged arbitrarily without affecting the solution set. Also, the order of the two roots of indicial equation in each column doesn't matter.

After we calculated the roots of indicial equation, we still need to determine the coefficient a_n, b_n of the series respectively. In our case, we are interested in determining the coefficient of $u(t)$ because it is analytic around the regular singular point $t = 0$. To determine the coefficient a_n, we plug the solution of $u(t)$ into the original differential equation. The coefficient of t with the same order must vanish, and this will give us a recurrence relation of the series

$$\frac{a_{n+1}}{a_n} = \frac{(n+\alpha)(n+\beta)}{(n+1)(n+\gamma)}, \quad n \in \mathbb{N} \tag{9.19}$$

Since the hypergeometric differential equation is a linear homogeneous differential equation, we can always set $a_0 = 1$ in the series. Then we can obtain the solution of a_n by multiplying all the recurrence relations from $\frac{a_1}{a_0}$ to $\frac{a_n}{a_{n-1}}$. The result is:

$$a_n = \prod_{\nu=0}^{n-1} \frac{(\nu+\alpha)(\nu+\beta)}{(\nu+1)(\nu+\gamma)} = \frac{(\alpha)_{\bar{n}}(\beta)_{\bar{n}}}{(\gamma)_{\bar{n}}} \tag{9.20}$$

$$\mu(t) = \sum_{n=0}^{\infty} \frac{(\alpha)_{\bar{n}}(\beta)_{\bar{n}}}{(\gamma)_{\bar{n}}} \cdot \frac{t^n}{n!} \tag{9.21}$$

where the Pochhammer symbols are defined as follows:

$$x_{\overline{n}} = x(x+1)(x+2)\cdots(x+n-1) \tag{9.22}$$

$$x_{\underline{n}} = x(x-1)(x-2)\cdots(x-n+1) \tag{9.23}$$

An alternative definition of Pochhammer symbol can be found in (9.4), (9.5) in the Appendix. For obvious reason, this solution converges at the region $|t| < 1$. Therefore, it represents an analytic function at that region in the complex plane, and it is called the hypergeometric function defined as:

$$F(\alpha, \beta; \gamma; t) = \sum_{n=0}^{\infty} \frac{(\alpha)_{\bar{n}}(\beta)_{\bar{n}}}{(\gamma)_{\bar{n}}} \cdot \frac{t^n}{n!}, \quad |t| < 1 \tag{9.24}$$

The hypergeometric function is analytic everywhere except the possible singularity at $t = \pm 1$. It has three free parameters α, β, and γ, with the convention that α and β are orderless. Once we knew those three parameters, the hypergeometric function can be determined uniquely.

Among the many theorems satisfied by the hypergeometric differential equation, the one we need to focus on here is the Displacement Theorem and the Substitution Theorem. Displacement Theorem states that if we write the solution of the original equation $u(t)$ by a new function $v(t)$ multiplied by a multiplication of powers with the following form

$$u(t) = v(t) \prod_{i=1}^{n} (t - a_i)^{\lambda_i} \tag{9.25}$$

It will result in shifting or displacing the roots of indicial equation, but the location and the classification of the singular points remains the same. The amount of the shift can be related with the exponent of the multiplicative factor by the following formula:

$$\begin{cases} \bar{\alpha}_i = \alpha_i - \lambda_i \\ \bar{\beta}_i = \beta_i - \lambda_i \end{cases} \quad i = 1, 2, 3, \ldots, n \qquad \begin{cases} \bar{\alpha} = \alpha + \sum_{i=1}^{n} \lambda_i \\ \bar{\beta} = \beta + \sum_{i=1}^{n} \lambda_i \end{cases} \tag{9.26}$$

The non-trivial point of this result is that the λ_i is the same with the exponent of the series in equation (9.25). In the most general case, the displacement will change the original form of equation. If we reverse the statement of this theorem, it tells us that if we displace the roots of the indicial equation, the solution of the original equation should be multiplied by a corresponding factor. The multiplicative factors are determined by the singularity a_i and the exponents λ_i in equation (9.25). To prove the Displacement Theorem, we begin by substituting equation (9.25) into the original differential equation. This substitution yields a new differential equation, which remains of Fuchsian type. We then compute the roots of the indicial equation corresponding to the transformed equation. The result is a new set of roots, each shifted by a displacement λ_i at the respective singularity.

On the other hand, Substitution Theorem states that a change of variable $z = \frac{at+b}{ct+d}, ad - bc \neq 0$ to all the three singular points 0,-1,∞ and the variable t itself will preserve the form of the original differential equation. In other words, it preserves the roots of the indicial equation. Such transformation is unique, and it is called Möbius transformation. Möbius transformation is a very fundamental transformation in complex analysis because it maps the complex plane onto itself in a conformal way. Unlike the Displacement Theorem, the Substitution Theorem only holds in the case that the equation has three distinct regular singular points. But this is enough for solving the Hypergeometric differential equation, because by definition Hypergeometric differential equation always has three distinct regular singular points located at $t = 0, t = 1, t = \infty$. Symbolically, we can represent the Substitution Theorem using the Riemann symbol in the following way.

$$P \left\{ \begin{array}{cccc} t_1 & t_2 & t_3 & \\ \alpha_1 & \alpha_2 & \alpha_3 & t \\ \beta_1 & \beta_2 & \beta_3 & \end{array} \right\} = P \left\{ \begin{array}{cccc} z(t_1) & z(t_2) & z(t_3) & \\ \alpha_1 & \alpha_2 & \alpha_3 & z(t) \\ \beta_1 & \beta_2 & \beta_3 & \end{array} \right\} \tag{9.27}$$

where we have used Möbius transformation $z(t)$ on three singular point $t1, t2, t3$, and the independent variable t. In this research, we apply the Displacement Theorem to the Hypergeometric differential equation. In the previous section, we have already computed the roots of the indicial equation at the singular point $t = 0$, and stated that the roots at $t = 1$ and $t = \infty$ are $(0, \gamma - \alpha - \beta)$ and (α, β), respectively. Using Riemann symbol, it follows that:

$$P \left\{ \begin{array}{ccccc} 0 & & 1 & & \infty & \\ 0 & & 0 & & \alpha & t \\ 1-\gamma & & \gamma-\alpha-\beta & & \beta & \end{array} \right\} \tag{9.28}$$

By applying Möbius transformations to these roots in the Riemann symbol, we observe

that, for some specific choices of the coefficients a, b, c, d, the transformation will permute the singular points 0, 1, and ∞. In particular, if the Möbius transformation is taken as $t \mapsto 1 - t$, then the singular point 0 is mapped to 1, 1 is mapped to 0, and ∞ remains unchanged. Symbolically we can write this as:

$$(0, 1, \infty) \to (1, 0, \infty)$$

Substitution Theorem states that this transformation will not change the form of the equation. In other words, the two Riemann Symbols should be equivalent to each other:

$$P\left\{\begin{array}{cccc} 0 & 1 & \infty & \\ 0 & 0 & \alpha & t \\ 1-\gamma & \gamma-\alpha-\beta & \beta & \end{array}\right\} = P\left\{\begin{array}{cccc} 0 & 1 & \infty & \\ 0 & 0 & \alpha & 1-t \\ \gamma-\alpha-\beta & 1-\gamma & \beta & \end{array}\right\} \tag{9.29}$$

When we do this transformation, it corresponds to interchanging the elements in the second and third rows of the first and second columns in Riemann Symbol. This means that we displaced the roots of indicial equations of singular point 0 and 1. From the Displacement Theorem we knew that if we write the solution of the original equation in a form that has multiplicative factors, it will result in a displacement of the roots. This theorem is also true if we reverse the statement: if we displace the roots of indicial equation of the original equation, we should multiply the solution with the corresponding multiplicative factors to give the new solution of the displaced equation. The multiplicative factors are determined by equation (9.26). Note that equation (9.29) has a constraint that the displacement of the first root $\alpha_i$and the second root β_i must be equal, and this constraint will give us a relation between the three coefficients α, β, and γ. In order to preserve the form of the differential equation, α, β, and γ must obey those relations. Here one can check that the following Hypergeometric function is also a solution to the original equation,

$$F(\gamma - \alpha, \gamma - \beta; 1 + \gamma - \alpha - \beta; 1 - t) \tag{9.30}$$

Thus, we successfully construct another linear independent solution of the hypergeometric differential equation. Ultimately, our goal is to use this approach to obtain the integral representation of the Bessel function of the second kind. To achieve that, we do the following displacement of the roots:

$$P\left\{\begin{array}{cccc} 0 & 1 & \infty & \\ 0 & 0 & \alpha & 1-t \\ \gamma-\alpha-\beta & 1-\gamma & \beta & \end{array}\right\} = P\left\{\begin{array}{cccc} 0 & 1 & \infty & \\ \gamma-\alpha-\beta & 0 & \alpha & 1-t \\ 0 & 1-\gamma & \beta & \end{array}\right\} \tag{9.31}$$

Here if we let $v(z)$ be the solution of the differential equation represented by the left-hand side Riemann Symbol. Then the right-hand side should represent the original equation, which means the roots inside the right-hand side Riemann Symbol should serve as α_i and β_i in equation (9.26). In this case only two singular points 0 and 1 are not at infinity, so i runs from 1 to 2. In this case, two displacements can be calculated as $\rho_1 = \gamma - \beta - \alpha, \rho_2 = 0$ respectively. The result of Displacement Theorem states that an

addition factor $(1-z)^{\gamma-\alpha-\beta}$ should be multiplied with the solution of the transformed hypergeometric differential equation $v(z)$ to give the final solution of the original equation:

$$u(t) = (1-t)^{\gamma-\alpha-\beta} F(\gamma-\alpha, \gamma-\beta; 1+\gamma-\alpha-\beta; 1-t) \tag{9.32}$$

where we used the fact that $v(t)$ is just the solution of the right hand side Riemann Symbol. Therefore, we have found two linear independent solution of the hypergeometric differential equation:

$$F(\alpha, \beta; \gamma; t) \tag{9.33}$$

$$(1-t)^{\gamma-\alpha-\beta} F(\gamma-\alpha, \gamma-\beta; 1+\gamma-\alpha-\beta; 1-t) \tag{9.34}$$

Actually, this is not the unique way to construct another linear independent solution of the Hypergeometric equation. We have all six different permutations of the order of singular points, and together with four distinct ways to displace the roots of indical equation. So we have $4*6 = 24$ different ways in total to construct another solution of Hypergeometric equation.

Note that only two of the solutions among those 24 solutions are linear independent, which means that any three of them should be linear dependent on each other. And this linear dependent relation has an analytical expression which can be derived by using Barnes' integral representation of Hypergeometric function (9.3). In this research, we will use equation (9.33), (9.34) to construct the Legendre function of the first kind and the second kind below. To do that, first we take a special case of hypergeometric differential equation when $\alpha = -n$, $\beta = n+1$, $\gamma = 1$, $z = \frac{1-t}{2}$ and in this case the hypergeometric differential equation turns into:

$$u''(t) + \frac{2t}{t(t-1)} u'(t) - \frac{n(n+1)}{t(t-1)} u(t) = 0 \tag{9.35}$$

The polynomial solutions of this hypergeometric differential equation, as we will mention below, is called Legendre functions. So we found that we can define the Legendre function by using hypergeometric function:

$$P_n(z) = F\left(-n, n+1; 1; \frac{1-t}{2}\right) \tag{9.36}$$

Now if we make a change of variable $t = 4z(1-z)$ to the original hypergeometric differential equation and substitute $\alpha = 2a$, $\beta = 2a$, $\gamma = a+b+\frac{1}{2}$, we can derive a relation:

$$F\left(2a, 2b; a+b+\frac{1}{2}; t\right) = F\left(a, b; a+b+\frac{1}{2}; 4t(1-t)\right) \tag{9.37}$$

Next we introduce the Euler transformation of hypergeometric function:

$$F(\alpha, \beta; \gamma; z) = (1-z)^{-\alpha} F\left(\alpha, \gamma-\beta; \gamma; \frac{z}{z-1}\right) \tag{9.38}$$

Euler transformation shows the linear dependence between some of the solutions in the total 24 solutions we mentioned above. But fortunately, Euler transformation will not

take equation (9.36) to a form which is proportional to equation (9.34). After applying the Euler transformation to equation (9.36), we derived the following useful formula:

$$F\left(a,b;\frac{a+b+1}{2};\frac{1-t}{2}\right)=z^{-a}F\left(\frac{a}{2},\frac{a+1}{2};\frac{a+b+1}{2};1-\frac{1}{t^2}\right) \tag{9.39}$$

Therefore, another linear independent solution of hypergeometric differential equation can be expressed as:

$$Q_n(t)=\frac{\sqrt{\pi}}{(2t)^{n+1}}\frac{\Gamma(n+1)}{\Gamma(n+3/2)}F\left(1+\frac{n}{2},\frac{1+n}{2};n+\frac{3}{2};\frac{1}{t^2}\right) \tag{9.40}$$

Schlaefli Integral

Cauchy's integral formula is defined as:

$$\frac{1}{2\pi i}\oint_C\frac{f(z)}{z-x}\,dz=f(x) \tag{9.41}$$

Now if we differentiate equation(9.41) by n times we get:

$$f^{(n)}(x)=\frac{n!}{2\pi i}\oint\frac{f(z)\,dz}{(z-x)^{n+1}} \tag{9.42}$$

The solution of the second-order Sturm-Liouville ODE with general form can be written by Rodrigues formula:

$$p(x)y''+q(x)y'+\lambda y=0 \tag{9.43}$$

$$y_n(x)=\frac{1}{w(x)}\left(\frac{d}{dx}\right)^n[w(x)p(x)^n] \tag{9.44}$$

Using equation (9.42), Rodrigues formula can be rewritten as:

$$y_n(x)=\frac{1}{w(x)}\frac{n!}{2\pi i}\oint_C\frac{w(z)[p(z)]^n}{(z-x)^{n+1}}\,dz \tag{9.45}$$

where the contour C should enclose the point x, and $w(z)[p(z)]^n$ is analytic everywhere inside contour C. This formula is called Schlaefli integral for $y_n(x)$.

Similarly, if we want to find integral representation of Legendre function of first kind, we can apply Cauchy's formula to equation(9.39). Then we obtain:

$$P_v(x)=\frac{2^{-v}}{2\pi i}\oint_C\frac{(t^2-1)^v}{(t-x)^{v+1}}\,dt \tag{9.46}$$

The contour of this integral representation can be verified by using the following steps: Considering the contour shown in Figure 4.1, and if we can successfully revisit the expression for $P_v(x)$ in equation (9.36) again, then we can confirm the contour of this integral representation.

Next, to derive the integral representation for Bessel function of the second kind, we start by using the integral representation of hypergeometric function [27]:

$$F(\alpha,\beta;\gamma;t)=\frac{\Gamma(\gamma)}{\Gamma(\gamma-\beta)\Gamma(\beta)}\int_0^1 u^{\beta-1}(1-u)^{\gamma-\beta-1}(1-ut)^{-\alpha}\,\mathrm{d}u \tag{9.47}$$

Using equation(9.40) together with equation (9.45) to express $Q_n(t)$ as:

$$Q_n(z) = \frac{\sqrt{\pi}\,\Gamma(n+1)}{(2t)^{n+1}\,\Gamma\left(n+\frac{3}{2}\right)} \sum_{k=0}^{\infty} \frac{(\alpha)_{\bar{k}}\,(\beta)_{\bar{k}}}{(\gamma)_{\bar{k}}} \cdot \frac{(\frac{1}{z^2})^k}{k!} \tag{9.48}$$

Here, we rewrite the variable t as z to distinguish it from the integration variable t in the following formula. We can use formula (9.7) in the Appendix to find an integral representation for $Q_n(t)$. Replacing the two Pochhammer symbols in the numerator of equation (9.48) with formula (9.5), and we can immediately identify that we can apply (9.7) in the denominator. This will give us some extract the Gamma function factors in the expression of $Q_n(t)$. After some simplifications, we can expression $Q_n(t)$ in the following form:

$$Q_n(z) = \frac{1}{(2z)^{n+1}} \sum_{k=0}^{\infty} \int_{-1}^{1} (1-t^2)^n \cdot \frac{(2k+n)!}{n!\,(2k+n-n)!} \left(\frac{t}{z}\right)^{2k} dt \tag{9.49}$$

where we have used (9.2) during the simplification. And Note that the factorial term in the above expression corresponds to the definition of a binomial coefficient, and thus it can be rewritten using binomial notation: $\binom{2k+n}{2k}$. Here, if we wish to express the binomial coefficient together with $\left(\frac{t}{z}\right)^{2k}$ as a single term, such as $\left(1-\frac{t}{z}\right)^{2k+n}$, we should apply the following identity that holds for binomial coefficients:

$$\binom{2k}{2k+n} = \frac{\Gamma(2k+n+1)}{\Gamma(n+1)\,\Gamma(2k+1)} = \frac{\Gamma(-n)}{\Gamma(-2k-n)\,\Gamma(2k+1)} = \binom{2k}{-n} \tag{9.50}$$

The above formula can be derived using (9.1) in Appendix. The resulting binomial expression indicates that we are now computing the coefficient of the $2k$-th term, $\left(\frac{t}{z}\right)^{2k}$, in the expansion of $\left(1-\frac{t}{z}\right)^{-n-1}$. The index 2k tells us that it should be an even number when k is an integer. We can use a mathematical trick to extend the index from even numbers to all integer values. Since the integration interval is symmetric, from -1 to 1, it is valid to add any odd function to the integrand, as its contribution will vanish upon integration. We could chose to add some odd function terms in the integrand such that it allows us to write the total expression as an binomial expansion of $\left(1-\frac{t}{z}\right)^{-n-1}$. The procedure are demonstrated as follows:

$$Q_n(z) = \frac{1}{(2z)^{n+1}} \sum_{k=0}^{\infty} \int_{-1}^{1} (1-t^2)^n (-1)^k \binom{-n-1}{k} \left(\frac{t}{z}\right)^k dt \tag{9.51}$$

$$= \frac{1}{(2z)^{n+1}} \int_{-1}^{1} (1-t^2)^n \left(1-\frac{t}{z}\right)^{-n-1} dt \tag{9.52}$$

Therefore we successfully obtained the following integral representation of Bessel function of the second kind:

$$Q_n(z) = \frac{1}{2^{n+1}} \int_{-1}^{1} \frac{(1-t^2)^n}{(z-t)^{\nu+1}}\,dt \tag{9.53}$$

Poisson Integral Representation

To find Poisson integral representation of Bessel function, we assume that the solution of Bessel function has the following general expression:

$$z^{\nu}\int_{a}^{b}e^{izt}T(t)\,dt \tag{9.54}$$

where T is only the function of t, not z. a and b are arbitrary complex numbers, independent of z. To prove this, one can plug this result into the Bessel differential equations. In order to satisfy the equation, the following relation must hold:

$$\frac{d}{dt}\left\{T(t^2-1)\right\}=(2\nu+1)Tt,\quad e^{izt}T(t^2-1)|_a^b=0 \tag{9.55}$$

The first equation shows that T is a constant multiple of $(t^2-1)^{\nu-\frac{1}{2}}$, and the latter shows that we should impose the boundary condition such that either $e^{izt}(t^2-1)^{\nu+\frac{1}{2}}$ has the same value in both limit a and b, or $e^{izt}(t^2-1)^{\nu+\frac{1}{2}}$ vanishes at each limit. We will adopt the first boundary condition in the following content, because under this boundary condition we could construct the same eight shape contour in complex plane with the integral representation of Legendre function of the second kind(see Figure 4.1). In this way, this integral can be related to the Legendre function of the second kind. By integrating the

$$J_{\nu}(z)=\frac{\Gamma\left(\frac{1}{2}-\nu\right)\left(\frac{z}{2}\right)^{\nu}}{2\pi i\,\Gamma\left(\frac{1}{2}\right)}\int_{C}e^{izt}(t^2-1)^{\nu-\frac{1}{2}}\,dt. \tag{9.56}$$

where C is a similar Contour shown in Figure 4.1. Another important integral representation is called the Poisson integral representation of Bessel function of the first kind. For the case of order zero, it is expressed as:

$$J_0(\omega)=\frac{1}{2\pi}\int_{-\pi}^{\pi}e^{i\omega\cos\theta}\,d\theta \tag{9.57}$$

This integral representation is commonly known as the Poisson integral representation, where ω is a real variable and θ is the angular integration variable. ω is defined as:

$$\omega=\sqrt{z^2+z'^2-2zz'\cos\phi}. \tag{9.58}$$

where z, z' and ϕ are all complex variables.

Lipschitz–Hankel Integral

We begin by evaluating the following integral:

$$I\;=\;\int_{0}^{\infty}e^{-at}\;J_{\nu}(bt)\;J_{\nu}(ct)\;t^{\,\mu-1}\,dt\;, \tag{9.59}$$

where following the Poisson integral representation of Bessel function J_{ν} will be used:

$$J_{\nu}(z)\;=\;\frac{\Gamma\!\left(\frac{1}{2}-\nu\right)\left(\frac{z}{2}\right)^{\nu}}{2\pi i\;\Gamma\!\left(\frac{1}{2}\right)}\;\int_{C}e^{\,iz\,t}\left(t^2-1\right)^{\,\nu-\frac{1}{2}}\,dt\;, \tag{9.60}$$

where the contour C encloses the branch cut of $(t^2-1)^{\nu-\frac{1}{2}}$ on the real axis of t from -1 to 1. At this stage we evaluate the contour integral in t. The integral has the contour around the branch cut $[-1,1]$ on the real axis. We can make the same simplification as demonstrated in chapter 4.2, where we reduce the contour into a real integral from -1 to 1. Using this technique, we can make the following transformation:

$$t = \cos\phi, \qquad dt = -\sin\phi\, d\phi, \qquad \phi \in [0,\pi].$$

Using $(1-\cos^2\phi) = \sin^2\phi$ we obtain:

$$J_\nu(z) = \frac{\Gamma\!\left(\frac{1}{2}-\nu\right)\left(\frac{z}{2}\right)^\nu}{2\pi i\,\Gamma\!\left(\frac{1}{2}\right)} \int_0^\pi e^{\,i\pi(\nu-\frac{1}{2})} e^{\,iz\cos\phi}\,\sin^{2\nu}\phi\, d\phi \tag{9.61}$$

From reflection formula: $\Gamma(\frac{1}{2}-\nu)\,\Gamma(\frac{1}{2}+\nu) = \frac{\pi}{\sin(\pi\nu)}$, it follows that $\frac{\Gamma(\frac{1}{2}-\nu)\,\sin\pi\nu}{\Gamma(\frac{1}{2})} = \frac{1}{\Gamma(\frac{1}{2}+\nu)}$. Substituting this result together with equation (9.52) into (9.50) we obtain:

$$I(a,b,c;\mu,\nu) = \left(\tfrac{1}{2}bc\right)^\nu \frac{1}{\Gamma\left(\nu+\frac{1}{2}\right)\Gamma\left(\frac{1}{2}\right)} \int_0^\infty \int_0^\pi e^{-at}\,\frac{J_\nu(\omega t)}{\omega^\nu}\, t^{\mu+\nu-1}\,\sin^{2\nu}\phi\, d\phi\, dt \tag{9.62}$$

where we define:

$$\omega \;=\; \sqrt{b^2+c^2-2bc\cos\phi}\,.$$

From equation (9.53), one can identify the following integral representation for hypergeometric function:

$$\int_0^\infty e^{-at}\, t^{\mu+\nu-1} J_\nu(\omega t)\, dt = \frac{(\omega/2)^\nu\,\Gamma(\mu+2\nu)}{a^{\mu+\nu}\,\Gamma(2\nu+1)}\,{}_2F_1\left(\frac{\mu+2\nu}{2}, \frac{\mu+2\nu+1}{2}; \nu+1; -\frac{\omega^2}{a^2}\right) \tag{9.63}$$

One can verify the above integral representation by plugging it into a hypergeometric differential equation. Then we can rewrite equation (9.54) as:

$$I(a,b,c;\mu,\nu) = \frac{(bc)^\nu\,\Gamma(\mu+2\nu)}{\pi a^{\mu+2\nu}\,\Gamma(2\nu+1)} \int_0^\pi {}_2F_1\left(\frac{\mu+2\nu}{2}, \frac{\mu+2\nu+1}{2}; \nu+1; -\frac{\omega^2}{a^2}\right) \sin^{2\nu}\phi\, d\phi. \tag{9.64}$$

If we let $\mu = 1$, equation (9.55) will reduce to Bessel function of the second kind according to equation (9.40):

$$\int_0^\infty e^{-at} J_\nu(bt) J_\nu(ct)\, dt = \frac{1}{\pi\sqrt{bc}}\, Q_{\nu-\frac{1}{2}}\left(\frac{a^2+b^2+c^2}{2bc}\right), \tag{9.65}$$

Bibliography

[1] Michael Tinkham. *Introduction to Superconductivity*. 2nd edition, McGraw-Hill, New York, 1996.

[2] S. Keckert, T. Junginger, T. Buck, D. Hall, P. Kolb, O. Kugeler, R. Laxdal, M. Liepe, S. Posen, T. Prokscha, *Critical fields of Nb_3Sn prepared for superconducting cavities*, Supercond. Sci. Technol. **32**, 075004 (2019).

[3] ILC Collaboration, *The International Linear Collider, Technical Design Report, Volume 3.1: Accelerator R&D*, June 2013. ISBN: 978-3-935702-76-8.

[4] R. Katayama, Y. Iwashita, H. Tongu, H. Oikawa, T. Kubo, T. Saeki, H. Hayano, H. Ito, T. Nagata, and R. Ito, *Evaluation of superconducting characteristics on the multilayer thin-film structure using the third harmonic voltage method*, Proc. 15th Annual Meeting of Particle Accelerator Society of Japan, WEOL04, Nagaoka, Japan (2018).

[5] R. Katayama *et al.*, "Evaluation of the superconducting characteristics of multi-layer thin-film structures of NbN and SiO2 on pure Nb substrate," SRF2019 Proceedings, Dresden, Germany.

[6] H. Padamsee, *RF Superconductivity: Science, Technology, and Applications*, Wiley-VCH, Weinheim, 2009.

[7] T. Kubo, *Effects of Nonmagnetic Impurities and Subgap States on the Kinetic Inductance, Complex Conductivity, Quality Factor, and Depairing Current Density*, Phys. Rev. Applied **17**, 014018 (2022). DOI: 10.1103/PhysRevApplied.17.014018.

[8] T. Kubo, *Multilayer coating for higher accelerating fields in superconducting radio-frequency cavities: a review of theoretical aspects*, Supercond. Sci. Technol. **30**, 023001 (2017).

[9] T. Kubo, *Superheating fields of semi-infinite superconductors and layered superconductors in the diffusive limit: structural optimization based on the microscopic theory*, Supercond. Sci. Technol. **34**, 045006 (2021).

[10] T. Kubo, Y. Iwashita, and T. Saeki, *Radio-frequency electromagnetic field and vortex penetration in multilayered superconductors*, Appl. Phys. Lett. **104**, 032603 (2014).

[11] T. Kubo, *Multilayer coating for higher accelerating fields in superconducting radio-frequency cavities: a review of theoretical aspects*, Supercond. Sci. Technol. **30**, 023001 (2017).

[12] T. Kubo, *Superheating fields of semi-infinite superconductors and layered superconductors in the diffusive limit: structural optimization based on the microscopic theory*, Supercond. Sci. Technol. **34**, 045006 (2021).

[13] R. Katayama, H. Hayano, T. Kubo, T. Saeki, C. Z. Antoine, H. Ito, R. Ito, Y. Iwashita, H. Tongu, and T. Nagata, *Evaluation of the Superconducting Characteristics of Multi-Layer Thin-Film Structures of NbN and SiO_2 on Pure Nb Substrate*, Proc. SRF2019.

[14] H. Ito, C. Z. Antoine, H. Hayano, R. Katayama, T. Kubo, T. Saeki, R. Ito, T. Nagata, Y. Iwashita, and H. Tongu, *Lower Critical Field Measurement of NbN Multilayer Thin Film Superconductor at KEK*, Proc. SRF2019 (2019).

[15] C. Z. Antoine, M. Aburas, A. Four, F. Weiss, Y. Iwashita, H. Hayano, S. Kato, T. Kubo, and T. Saeki, *Optimization of tailored multilayer superconductors for RF application and protection against premature vortex penetration*, Supercond. Sci. Technol. **32**, 085005 (2019).

[16] K. Fujii, C. Grojean, M. E. Peskin, T. Barklow, Y. Gao, S. Kanemura, H. Kim, J. List, M. Nojiri, M. Perelstein, R. Pöschl, J. Reuter, F. Simon, T. Tanabe, J. D. Wells, J. Yu, H. Baer, M. Berggren, S. Heinemeyer, S.-L. Lehtinen, J. Tian, G. Wilson, J. Yan, H. Murayama, and J. Brau, *The Potential of the ILC for Discovering New Particles*, arXiv:1702.05333 [hep-ph], DESY 17-012, KEK Preprint 2016-60, SLAC–PUB–16916, 2017.

[17] A. Gauzzi, J. Le Cochec, G. Lamura, B. J. Jönsson, V. A. Gasparov, F. R. Ladan, B. Plaçais, P. A. Probst, D. Pavuna, and J. Bok, *Very high resolution measurement of the penetration depth of superconductors by a novel single-coil inductance technique*, Rev. Sci. Instrum. **71**, 2147–2153 (2000).

[18] P. Bambade *et al.*, *The International Linear Collider: A Global Project*, arXiv:1903.01629 [hep-ex] (2019).

[19] G.B. Arfken, H.J. Weber, and F.E. Harris, *Mathematical Methods for Physicists*, 7th ed., Academic Press, 2012.

[20] S. Michizono, *The International Linear Collider*, Nat. Rev. Phys. **1**, 244–245 (2019).

[21] M. D. Schwartz, *Quantum Field Theory and the Standard Model*, Cambridge University Press, 2014.

[22] M. E. Peskin and D. V. Schroeder, *An Introduction to Quantum Field Theory*, Addison-Wesley, 1995.

[23] C. Timm, *Superconductivity*, 2nd ed., Academic Press, 2007.

[24] Bardeen J., Cooper L. N., and Schrieffer J. R., 1957, "Theory of Superconductivity," *Physical Review* **108**, 1175–1204.

[25] B. S. Chandrasekhar and D. Einzel, "The superconducting penetration depth from the semiclassical model," *Annalen der Physik*, vol. 505, no. 6, pp. 535–546, 1993.

[26] D. J. Griffiths, *Introduction to Electrodynamics*, 4th ed. (Pearson, Boston, 2013).

[27] G. Kristensson, *Second Order Differential Equations: Special Functions and Their Classification*, Springer, 2010.

[28] G. N. Watson, *A Treatise on the Theory of Bessel Functions*, 2nd ed., Cambridge University Press, 1944.

[29] A. Prosperetti, *Advanced Mathematics for Applications*, Cambridge University Press, 2011.

[30] H. V. Alizadeh and B. Boulet, "Analytical Calculation of the Magnetic Vector Potential of an Axisymmetric Solenoid in the Presence of Iron Parts," *IEEE Transactions on Magnetics*, vol. 52, no. 3, pp. 1–4, 2016. doi:10.1109/TMAG.2015.2477083

[31] D.J. Griffiths and D.F. Schroeter, *Introduction to Quantum Mechanics*, 3rd ed., Cambridge University Press, 2018.

[32] T. Kubo, *Magnetic Fields in Bulk, Film, and Multilayer Superconductors in Front of a Multi-Turn Coil*, Proceedings of IPAC2016, Busan, Korea, WEPMB019 (2016).

[33] T. Kubo, *Magnetic Fields in Bulk, Film, and Multilayer Superconductors in Front of a Multi-turn Coil*, Proc. SRF2019.

[34] T. Kubo, "Change of Coil Inductance due to a Superconducting Sample," internal research note (unpublished), 2021.

[35] COMSOL Multiphysics® v6.2, COMSOL AB, Stockholm, Sweden.

[36] Wolfram Research, Inc., *Mathematica*, Version 13.3, Champaign, IL (2023).

[37] D. C. Meeker, *Finite Element Method Magnetics*, Version 4.2 (15 Jan 2022), `http://www.femm.info`.

[38] M. Yamaguchi *et al.*, "TISPISGIMR: A Novel Experimental Technique for Penetration Depth Measurement," *Japanese Journal of Applied Physics*, vol. 60, 2021.

[39] S. Dzhumanov, U.M. Turmanova, and U.T. Kurbanov, *Two distinctive temperature dependences of the London penetration depth in high-Tc cuprate superconductors as support for the theory of Bose-liquid superconductivity*, Physics Letters A **452**, 128447 (2022).

[40] R. Prozorov and R. W. Giannetta, "Magnetic Penetration Depth in Unconventional Superconductors," *Superconductor Science and Technology*, 19 April 2006.

[41] V.A. Gasparov and A.P. Oganesyan, *Temperature dependence of the penetration depth in epitaxial $Y_1Ba_2Cu_3O_{7-x}$ thin films*, Physica C **178**, 445–448 (1991).